The X-ray Spectrum of Cygnus X-3

by

Shunji Kitamoto

DISSERTATION IN PHYSICS

THE OSAKA UNIVERSITY

GRADUATE SCHOOL OF SCIENCE

TOYONAKA, OSAKA

ABSTRACT

The X-ray binary Cygnus X-3 was observed in September 1983 and in September 1984 by the SPC (scintillation proportional counters) aboard Tenma.

The X-ray spectral shape as well as the flux reveals 4.8-hour modulation. The modulation can not result from the variations of absorption column density either of the neutral gas or of the He-like partially ionized gas. One of the possible cause is Comptonization by a hot plasma.

Iron feature from Cygnus X-3 was detected at an energy of about 6.7 keV. Its flux was 0.01 ~ 0.03 counts/sec/cm^2 and appeared to have no 4.8-hour modulation. The flux of the feature correlated well with the average flux in the energy range 9 to 10 keV during the 4.8-hour period. In addition, the spectra showed a shallow dip around 9~10 keV, which might be an absorption edge of FeXXV. These facts suggest that the emission mechanism of iron lines is a fluorescence of plasma (~10^6K) exposed to X-rays, and that this plasma is not influenced by the cause of 4.8-hour modulation.

From our observations and previous observations, we propose the following model for Cygnus X-3. Cygnus X-3 is a binary system containing a neutron star with 4.8-hour orbital period. X-rays and γ-rays are emitted around the neutron star. The system is enshrouded with matter, whose center is shifted toward the companion star. The electron scattering depth of the matter from the surface of the companion star to infinity is several. In the inner region, on the binary orbital scale (~10^{11} cm), the

ionization is complete and the temperature is about several tens keV. The iron lines come from the outer region of the plasma. which is cooler than the inner region.

It will be shown that this model can explain almost all the characteristic of Cygnus X-3. from radio to X-rays.

CONTENTS

CHAPTER Ⅰ. Introduction. ..... 1.

CHAPTER Ⅱ. Review. ..... 5.

Ⅱ-1. Radio. ..... 5.

Ⅱ-2. Infrared and Optical. ..... 6.

Ⅱ-3. X-rays. ..... 7.

Ⅱ-4. γ-rays. ..... 11.

Ⅱ-5. Models. ..... 12.

CHAPTER Ⅲ. Tenma. ..... 17.

Ⅲ-1. The Tenma Satellite. ..... 17.

Ⅲ-2. The SPC system. ..... 19.

Ⅲ-3. Data acquisition. ..... 21.

CHAPTER Ⅳ. Observations. ..... 23.

CHAPTER Ⅴ. Data analysis and Results. ..... 26.

Ⅴ-1. Light curve and Ephemeris. ..... 26.

Ⅴ-2. Spectra and Spectral variations. ..... 31.

Ⅴ-3. Model fitting of the observed spectra.. 34.

Ⅴ-4. Iron lines. ..... 36.

Ⅴ-5. Absorption Edge. ..... 39.

CHAPTER Ⅵ. Discussions. ..... 41.

Ⅵ-1. Period change. ..... 41.

Ⅵ-2. Emission region of iron lines. ..... 44.

Ⅵ-3. Previous proposed models. ..... 49.

Ⅵ-4. Hot gas model. ..... 52.

Ⅵ-5. Concluding remarks. ..... 63.

APPENDIX A. ..... 65.

APPENDIX B. ..... 67.

CHAPTER I. INTRODUCTION

Since the first discovery of an extrasolar X-ray source in 1962 (Giacconi et al. 1962), X-ray astronomy has developed rapidly. Now it is one of the important wave bands for the study of heavenly bodies together with radio, infrared, and visible bands etc.

X-rays have been observed from clusters of galaxies, quasars, active galaxies, supernova remnants, and most types of stars. Apart from the Crab Nebula, the most luminous galactic X-ray sources are close binary systems which contain a neutron star (or black hole), and a normal stellar companion. These sources can be roughly divided into two groups. One is the X-ray pulsars, which exhibit a regular periodic variation of X-ray intensity. The optical counterparts of many of these have been identified with normal massive stars. The pulsars are generally thought to consist of a strongly magnetized neutron star ($\sim 10^{12}$ gauss at the surface) and a normal star, usually a young giant star of Population I. The normal star supplies matter for the neutron star either by Roche-Lobe overflow or from the stellar wind. The matter accretes onto the neutron star, where the gravitational energy is released as X-radiation. A strong magnetic field, which is thought to be mis-aligned with the rotation axis of the neutron star, funnels the accreting matter and produces anisotropic radiation. This results in X-ray pulsation as seen by distant observers. For a comprehensive accounts, see the recent review article by Rappaport and Joss (1981).

Another group is the so-called "galactic bulge" sources. Some of them occasionally exhibit X-ray bursts. The blackbody radius of the X-ray burst is about 10 km (van Paradijs, 1978, Ohashi et al. 1982), consistent with the theoretical radius of a neutron star (Arnett and Bowers 1977). The bursts are very likely due to a thermonuclear flash which occurs in a blanket of accreted matter on a neutron star (Joss 1978). The optical counterparts of several of these sources have been identified with faint late-type stars. Therefore, many authors assume that they also contain a neutron star (or black hole) and an optical companion (usually unseen) which approximately fills its critical Roche-lobe and supplies gas for the compact object via an accretion disk. Mitsuda et al. (1984), Hayakawa et al. (1984) and Hirano et al. (1984) proposed a model in which the X-rays are emitted from the surface of a weakly magnetized neutron star and from an optically thick accretion disk.

Cygnus X-3 was first discovered as an X-ray source by Giacconi et al.(1967) during a survey of the Cygnus region made with an X-ray instrument on an Aerobee rocket launched in 1966. Usually Cygnus X-3 is classified into the latter group, i.e. the so-called "galactic bulge" sources. However, Cygnus X-3 exhibits many types of behavior different from other X-ray sources. Cygnus X-3 is not only an X-ray source but also a radio, infrared, γ-ray and probably cosmic-ray source. Sometimes giant radio outbursts of Cygnus X-3 occur, and at these times it becomes one of the strongest compact radio sources in the sky. As an X-ray source, Cygnus X-3 is rather bright source and exhibits a particularly intense iron line emission. Pravdo

(1979) stated that "The iron line of Cygnus X-3 is the "Sco X-1" of iron lines." (Sco X-1 is the brightest X-ray source in the sky.) The X-ray and infrared flux from Cygnus X-3 show a smooth, nearly sinusoidal variation having a period of 4.8 hours. The 4.8-hour period is an order of magnitude longer than X-ray pulsar periods (69 ms - 835 sec). Such periods are known to occur in U Gem systems and novae, but the luminosity of these sources is about two orders of magnitude lower than that of Cygnus X-3. It is difficult to imagine that Cygnus X-3 belongs in the same category. Two X-ray sources, 4U1822-37 and 4U2129+47, have similar periodic modulation of their X-ray intensity, whose periods are about 5.7 hours and 5.2 hours, respectively. They display an unusual partial X-ray eclipse. White and Holt(1982) thought that Cygnus X-3 belongs in the same category with these sources.

The detection of fluxes of γ-rays with energy $E>10^{8}$eV and $E>10^{12}$eV from the direction of Cygnus X-3 have been reported. Recently, Samorski and Stamm (1983) reported the detection of high energy quanta, presumably γ-rays, with energy $E>2\times10^{15}$eV from Cygnus X-3; The detection of γ-rays in this energy range have been reported from only two sources; Cygnus X-3 and Vela X-1 (Protherore and Gerhardy, 1984).

Hjellming (1973) referred to " An Astronomical Puzzle called Cygnus X-3".

The second Japanese X-ray astronomy satellite, "Tenma", observed Cygnus X-3. Tenma is equipped with gas scintillation counters with twice the energy resolution of conventional proportional counters, giving superior spectral data. In this

work, we show the results of data analysis for Cygnus X-3, and present a new model for Cygnus X-3 based upon the new results and previous observations. In Chapter Ⅱ, we review these previous observations and the proposed models. In Chapter Ⅲ, the Tenma satellite is described. In Chapter Ⅳ, we describe the observations of Cygnus X-3 and the data analysis procedures. Detailed analysis and results are given in Chapter Ⅴ. In Chapter Ⅵ, we describe the interpretations of the results and our speculations, and critically examine previously-proposed models. Finally, we propose a new model, the "hot gas model".

CHAPTER II. Review.

Since the discovery of Cygnus X-3, many observations of radio, infrared, X-rays and γ-rays have been carried out. A composite spectrum of Cygnus X-3 from radio to γ-rays is shown in figure-1. Many models to explain the complex behavior of Cygnus X-3 have been proposed on the basis of these various observations. However, none of these models can explain fully all of the behavior of Cygnus X-3. In this chapter, the observed results in each wave band are reviewed and some of the previously proposed models are described.

II-1. Radio.

The flux of radio from Cygnus X-3 is usually several hundreds mJy (1 Jy=10^{-26} W/m^2/Hz). Although no evidence for the 4.8-hour period seen at infrared and X-rays has been found, irregular flux variations have been reported (Hjellming et al. 1974). A number of strong radio flares (10-20 Jy) from Cygnus X-3 have been observed. Woodsworth (1983) searched for periodicities in the large amplitude radio flaring, but with no positive result. The radio outbursts in September 1972 were extensively observed by many groups (Hjellming 1973, and references therein). From the results of many different wave bands, it was shown that the spectral variation during a flare could be explained by synchrotron radiation from an expanding cloud of relativistic electrons (Gregory et al. 1972). Such an outburst provides an opportunity to obtain a distance estimate by observing absorption by galactic neutral hydrogen at 21 cm, and the resulting lower limit for the distance to Cygnus X-3 is 11.6

kpc (Dickey 1983, Chu and Bieging, 1973, Lauque et al. 1972). The column density of neutral hydrogen along the line of sight is at least 1.7×10^{20} T_S cm^{-2}, where T_S is line spin temperature in degree K, which is about 100° K (Chu and Bieging, 1973). Geldzahler et al. (1979) observed Cygnus X-3, with very long-baseline interferometer (VLBI), and reported the angular size to be 0.0013 ± 0.0002 arcsec. If the distance to Cygnus X-3 is 12 kpc from the sun, then the corresponding linear diameter is about 2×10^{14} cm. Geldzahler et al. (1983) reported that they observed jetlike emission expanding with the speed of $\geqq 0.35c$ after outburst occurred in 1982 September.

II-2. Infrared and optical.

Infrared radiation from Cygnus X-3 was discovered by Becklin et al. (1972). The flux density of the infrared, which at 2.2 μm is about 10-20mJy, shows a 4.8-hour modulation synchronized with the X-ray flux (Becklin et al. 1973). If the source is taken to be at a distance of 12 kpc, its 2.2 μm absolute magnitude is brighter than -3.6. This makes it at least as bright as an early O star. From joint X-ray, infrared and radio observations (Becklin et al. 1973, Becklin et al. 1974, Mason et al. 1976), it was shown that there is no simple radio-infrared correlation. Several types of behavior in the infrared flux variations were reported : (a) short time variations with time scales on the order of 2 minutes, (b) longer time scale outbursts with time scales on the order of 1 to 2 hours, (c) an apparent absence of regular periodic structure, and (d) long-term variability.

Westphal et al.(1972) searched for a visible counterpart at

the radio position. but no visible object was detected. The upper limit of the flux is about $2\sim6\times10^{-6}$ Jy ($V \geqq 23.9$ mag.). The extinction in the direction of Cygnus X-3 is about 1.5 mag. at 2.2 μm on the basis of the observation of infrared flux (Becklin et al. 1973). corresponding to 10-20 mag at visual wavelengths. which means that the column density of neutral hydrogen is about $2\sim5\times10^{22}$ atoms/cm^2. If we assume the distance to Cygnus X-3 is 12 kpc. the absolute magnitude is fainter than -1.5 ~ -11.5 mag. in visual wavelengths.

II-3. X-rays.

Since the discovery of X-rays from Cygnus X-3 (Giacconi et al.1967). many observations have been carried out with rockets. balloons and satellites.

Parsignault et al. (1972) and Sanford et al.(1972) found the intensity variation to be periodic with a period of 4.8 hours. The period is extremely stable and its derivative is about 10^{-9} sec/sec (Elsner et al. 1980. van der Klis and Bonnet-Bidaud. 1981). This suggests that the periodic variation results from orbital motion in a binary system. However. the X-ray behaviour of Cygnus X-3 does not resemble that of most other X-ray binaries. The X-ray light curve is unique in that it does not show the typical eclipse shape with a zero level. flat minimum. Rather. it reveals a nearly sinusoidal curve. and the ratio of I_{max} to I_{min} is about 2 or 3 (Parsignault et al. 1972) in the several-keV range. In the several tens of keV range. the amplitude of the modulation is smaller or non-existent (Ulmer et al. 1974. Baity et al. 1973). The detailed properties of this

nearly sinusoidal light curve are compiled here from several authors:

(1). The average 4.8-hour X-ray light curve is asymmetric with a sharp fall to X-ray minimum followed by a gradual rise (Mason et al. 1976) and this shape is stable over several years (Elsner et al. 1980).

(2). The shape of the light curve is variable from one cycle to the next (van der Klis and Bonnet-Bidaud. 1982).

(3). Variations occur mainly around the maximum of the light curve (van der Klis and Bonnet-Bidaud. 1982).

(4). The amplitude of the 4.8-hour modulation is correlated with the average source level and varies more than proportionally (Bonnet Bidaud and van der Klis. 1981).

(5). There are quasi-periodic variations in the X-ray flux (van der Klis and Jansen 1984).

Cygnus X-3 exhibits longer term variations. Leach et al.(1975) reported that there are two distinct flux levels in the 2-6 keV range. The "high state" is about an factor 3 brighter than the "low state". which has a harder spectrum. A period of 34.1 days in the X-ray intensity was reported by Holt et al.(1979) and Molteni et al.(1980). However. this period is not confirmed. Bonnet-Bidaud and van der Klis reported that a variation was found in the phase of arrival of the minimum of the light curve. suggestive of a $\sim$20 day periodicity. Parsignault et al.(1977) searched for periodicity shorter than 4.8 hours. but no periodicity in the range 2 sec - 30 min. was found.

Many authors reported the spectrum of Cygnus X-3. but their results are quite variable. Especially. there is a great

difference between the spectra of the high and low states.

The continuum spectrum in the range 2-10 keV. in the high state. is roughly a blackbody spectrum with kT $\sim$ 1.2 to 1.4 keV (Serlemitsos et al. 1975. Sanford et al. 1975. White and Holt. 1982). The column density is (2 $\sim$ 5)x10^{22} H atoms/cm^2 and this value agrees reasonably with the radio measurements (Chu and Bieging. 1973). At energies greater than 10 keV. the observed spectrum exhibits an excess from an extrapolation of the black body spectrum fitted in the low energy region. White and Holt. (1982) assumed that this component is a power law spectrum with a photon index of about 1.6$\sim$1.9. The spectrum in the low intensity phase of the 4.8-hour modulation tends to become flatter than in the high intensity phase. However. no variation in absorption across the modulation is observed (Blissett et al. 1981. White and Holt. 1982). The upper limit to any phase-related change in absorption is $<$ 1.5x10^{22} H atoms/cm^2 (White and Holt. 1982). If the distance to Cygnus X-3 is 12 kpc. the luminosity of X-rays is several times $\sim 10^{38}$ erg/sec.

In the low state. the continuum spectrum is harder than in the high state and it is roughly represented by a power law spectrum with a photon index of 1$\sim$1.5 (Becker et al. 1978. White and Holt. 1982) with a break at $\sim$18 keV. above which energy the spectrum falls with e-folding energy of $\sim$16 keV. The photoelectric absorption is $\sim$7x10^{22} H atoms/cm^2. The spectrum in the low intensity phase of the 4.8-hour modulation is also harder than in the high intensity phase. Becker et al. (1978) reported that there exists a less-modulated low energy component: if this is a thermal bremsstrahlung spectrum. the temperature is

about 3 keV. White and Holt. (1982) also reported that there is a soft thermal component modulated differently than the higher energy component. but its energy is about 0.3 keV and they pointed out that this soft component may be not intrinsic to Cygnus X-3. but rather may come from confusion with Cygnus OB 2 (Harnden et al. 1979). Assuming the 12 kpc distance. the luminosity of X-rays is about 5×10^{37} erg/sec.

The spectrum in the range 10 - 100 keV is roughly a power low spectrum with a photon index of 4～2 (Meegan et al. 1979. Reppin et al. 1979). The spectral variation between the high state and the low state is not clear.

The iron feature of Cygnus X-3 is extremely strong. Since the report of Sanford et al.(1975) and Serlemitsos et al.(1975). many observations have been carried out. The intensity of the iron feature is about 0.01～0.05 photons/cm^2/sec. and the central energy is 6.5～6.8 keV. The equivalent width is 300～700 eV in the high state and 1000～1500 eV in the low state. Many authors concluded that the equivalent width appears to be phase-independent. Becker et al.(1978) reported that the centroid of the iron feature shifts ～0.2 keV in phase with 4.8-hour cycle. with its center at 6.7 and 6.5 keV at phase 0.0 and 0.5. respectively (we use the convention that the phase 0 corresponds to the X-ray minimum when the light curve is fitted to a sinusoidal curve). Blissett et al. (1981) also observed the same behaviour. White and Holt. (1982). Serlemitsos et al. (1975) and Blissett et al. (1981) reported that the line width (FWHM) is about 1 keV. but Sanford et al. (1975) concluded that its width is less than 1 keV. Kestenbaum et al. (1977.1978) observed the

iron feature of Cygnus X-3 with a crystal spectrometer. Their results are that the energy is 6.52 ± 0.08 keV and 6.84 ± 0.17 keV. the intensity is 0.0097 ± 0.0043 and 0.020 ± 0.008 photons/cm^2/sec. the width is $\leqq 200$ eV and $\leqq 600$ eV. in the low state and the high state. respectively.

Elsewhere in the X-ray spectrum. White and Holt. (1982) detected Si and S lines by the Einstein (HEAO 2).

Ⅱ-4. γ-rays.

Lamb et al. (1977) reported the detection of γ-rays from Cygnus X-3 at energies above 35 MeV with a 4.8-hour periodicity. At these energies. the modulation is significantly larger than that seen in the X-ray and infrared light curves. The data are consistent with zero flux near phase 0. However. Bennett et al. (1977) could not detect a significant flux in this energy range. Hermsen (1984) reported that the upper limit of the γ-ray flux for 70 MeV < E < 5000 MeV was 1.0×10^{-6} photons/cm^2/sec.

Neshpor et al. (1979) observed γ-rays from Cygnus X-3 at energies above 10^{12}eV. Danaher et al. (1981). Lamb et al. (1982). Weekes (1983) and Dowthwaite et al. (1983) also reported the detection of γ-rays in this energy range. The flux of γ-rays in this energy range has a 4.8-hour periodicity and is composed of two narrow pulses around phases 0.2 and 0.8.

Recently. Samorski and Stamm (1983) have reported and Lloyd-Evans et al.(1983) have confirmed the detection of high-energy quanta. presumably γ-rays. with energy $E > 2 \times 10^{15}$ eV from Cygnus X-3.

II-5. Models.

The 4.8-hour period of Cygnus X-3 is very stable. with a period derivative of about 10^{-9}sec/sec. This variation presumably results from orbital motion in a binary system. If this period was instead the rotational period of an X-ray star. it would not be so stable period because of the momentum carried by the matter transferred from the companion star. Assuming the orbital period to be 4.8 hours. we can estimate the separation as

$$0.8 \times 10^{11} (M_X/M_\odot + M_C/M_\odot)^{1/3} \text{ cm}$$

where. M_X is the mass of the X-ray star. M_C is the mass of the companion star and $M_\odot$ is the solar mass. If both the masses are about 1 $M_\odot$. the separation is about 10^{11}cm.

Many models have been proposed to explain the complex behavior of Cygnus X-3.

Gregory et al. (1972) proposed the following model for the radio outburst. Cosmic-ray particles are ejected from a very small region. These relativistic particles begin an expansion which carries along magnetic fields that originally surrounded the system. The radio outburst is the synchrotron radiation from an expanding bubble of relativistic particles and magnetic fields. Peterson (1973) calculated on the basis of this model that a maximum mass of $0.76 \times 10^{-8} M_\odot$ was injected over a period of 1.2 day for the outburst in September 1972.

The quiescent radio emission from Cygnus X-3 was explained by the following model (Seaquist and Gregory. 1977. Vestrand. 1983). The compact star emits γ-rays with energies more than 10^8 eV. These γ-rays interact with the enshrouding matter which extends to radii $R > 10^{14}$ cm. and electrons and positrons are

generated. The synchrotron radiation of these electrons and positrons is the observed radio emission.

Vestrand and Eichler.(1982) explained that the γ-rays with $E > 10^{12}$ eV result from the companion's atmosphere acting as target material for particles accelerated near the X-ray star. This model can reproduce the observed light curve composed of two narrow pulses at X-ray phase about 0.2 and 0.8.

Many models have been proposed to explain the behavior at X-ray and infrared wavelength. In all models. Cygnus X-3 is a close binary system containing a neutron star and a normal stellar companion. having 4.8-hour orbital period.

① Reflection model.

This model. proposed by Basko et al. (1974). is that the neutron star emits hard X-rays. We do not observe the X-rays directly. but instead observe the reflection at the surface of the companion star. Since the reflection occurs only the hemisphere exposed to the X-rays. the observed region reflecting X-rays changes as the system revolves. The expected light curve corresponding to inclination $\sim 15^{\circ}$ resembles the X-ray light curve of Cygnus X-3. If the distance to Cygnus X-3 is 12 kpc. to explain the observed X-ray luminosity of about 10^{38} erg/sec. the X-ray luminosity of the primary source should be more than 10^{39} erg/sec. This value strongly exceeds the Eddington limit.

$$L_E \sim 10^{38} (M_X/M_{\odot}) \text{ erg/sec} .$$

which is likely to be an upper limit for the X-ray luminosity of the accreting neutron star. Thus. the assumption of an accreting neutron star as the X-ray source in Cygnus X-3 meets

severe difficulties. Basko et al.(1974) assumed that the X-ray star in Cygnus X-3 is a non-accreting young pulsar (similar to that in the Crab Nebula). with a very short period .P≦0.01 sec.

② Stellar wind model.

Pringle (1974) proposed a model in which the mass loss from the companion surrounds the system with a dense wind. A similar model was proposed by Davidsen and Ostriker (1974). If the cloud is not both perfectly spherical and centered on the X-ray source. the X-ray flux will nonisotropic. because photons will escape most readily in the direction of minimum scattering depth. For a fixed observer. the scattering depth to the X-ray star changes with the orbital motion. This change of the scattering depth leads to the change of the X-ray intensity. Therefore. we observed the 4.8-hour modulation. This model was elaborated in Monte Carlo simulations by Hertz et al. (1978). Ghosh et al. (1981) assumed that the asymmetry in the 4.8-hour X-ray light curve results from an elliptical binary orbit and determined the orbital parameters in this model.

③ Cocoon model.

Milgrom (1976) and Milgrom and Pines. (1978) proposed a model which consists of an ordinary X-ray binary system at the center of a spherical shell of gas. the radius of which is sufficiently larger than the separation. Except for a cap which is shaded by the companion. the shell is exposed to the X-ray flux from the compact member. This flux is scattered by free

electrons in the shell or is absorbed and reemitted. With the orbital motion. the shade scans the equator of the shell. For a fixed observer. an X-ray minimum will be seen when the shade faces the observer. Hertz et al. (1978) examined this model with Monte Carlo simulations. In their results. the absorption in the shade resembles the light curve of Cygnus X-3. if the radius of companion is less than 0.6 times the separation. Ghosh et al. (1981) determined the orbital elements in this model. Their results implies that the companion's size exceeds that of its critical lobe. and they suggest that the dense stellar wind can form a "dress" around the "bare" companion. mimicking a star bigger than its critical lobe.

④ Accretion disk corona (A.D.C.) model.

White and Holt (1982) proposed the following model. They thought that there was an accretion disk around the neutron star. and at the edge of the accretion disk there was a bulge which was caused by the inflowing material. The central X-ray source in this system is diffused by a large Compton-thick accretion disk corona (A.D.C.). The quasi-sinusoidal modulation can be reconciled with the partial occultation of the A.D.C. by the bulge . In the low state. the optical depth to the central X-ray object is about 5 and the high state can be reconciled with an increase in optical depth to $\geqq 10$ that may be associated with an increase in the central source luminosity.

⑤ An elliptical orbit model.

Elsner et al. (1980) and Ghosh et al. (1981) discuss the

possibility that the X-ray source is in an elliptical orbit and some. or all. of the observed period derivative may be due to apsidal motion. They thought that the nearly sinusoidal light curve is explained by the stellar wind model or the cocoon model. Further. the elliptical orbit hypothesis explains the observed asymmetry in the average X-ray light curve and leads to the conclusion that the most likely companion to the X-ray source is a helium star (van den Heuvel and de Loore. 1973). possibly with a light hydrogen envelope.

CHAPTER Ⅲ. TENMA.

Ⅲ-1. The Tenma Satellite.

Tenma. the eighth Japanese scientific satellite. was successfully launched on February 20. 1983. by the Institute of Space and Astronautical Science (ISAS). It was placed into a near circular orbit with an apogee of 501 km. a perigee of 497 km and an inclination of 31.5° . The orbital period is about 94.5 minutes.

Figure 2 schematically shows the structure of Tenma. The spacecraft body is an approximate cube of 89.5 cm height and 110.4 cm width. weighing about 218 kg. Four solar paddles provide electric power of 150 W at maximum. The direction of the z-axis (normal to the upper panel) with respect to the sun must be between 120° and 160° to obtain enough power and to protect the battery from over charging. which restricts the observable X-ray sources in a given part of year.

Tenma is a spin-stabilized satellite. However. its major angular momentum can be carried by a bias momentum wheel with the spacecraft body rotating slowly. In the freely spinning mode with the momentum wheel inactive. the rate is kept between 1.5 rpm and 2 rpm. The total angular momentum of the spacecraft is adjusted by torquing against the earth's magnetic field. using of magnetic unloading coils. Nutation of the satellite is suppressed by means of a pair of nutation dampers (dissipation in a viscous fluid).

The satellite attitude is measured with sun. geomagnetic. horizon. and star sensors. Fine attitude with an accuracy of a few arc minutes is obtained by the star sensor. The position of

the X-ray sources referred to satellite coordinates can be measured with some of the X-ray detectors. The spin axis is maneuvered to the desired direction of the sky by means of the magnetic torquing coil. which generates a magnetic moment aligned with the spin axis of 10 ATm^2 at maximum. The optimum magnitude and polarity of the magnetic moment are selected every 2 minutes by delayed commands from an on-board programmable timer. The optimum sequence of delayed commands is calculated with the ground-based computer simulation.

An on-board data processor accumulates all the data (X-ray data. housekeeping data. attitude data etc.) and edits them into a telemetry format. The telemetry format consists of major and minor frames. A major frame comprises 64 minor frames. The data processor sends the data to a telemetry and to a data recorder. In the high bit rate (8 kbps) mode. major and minor frames correspond to 8 sec and 125 msec. respectively. and in the low bit rate (2 kbps) mode. 32 sec and 500 msec. respectively.

The on-board data recorder can store the data for 160 minutes in the low bit-rate mode and for 40 minutes in the high bit-rate mode. The data recorder is controlled by an on-board programmable timer and changes of the reading mode every 2 minutes are possible. The stored data are dumped during ground contact at 32 kbps for about 10 minutes duration. Ground contacts are available in five successive orbits out of 15 orbits a day.

Four high energy astrophysical experiments are conducted on Tenma. Their characteristics are summarized in table 1 and figure 3 shows the field of view of each experiment. The major

experiment is the spectral and temporal study of cosmic X-ray sources in the range 2-60 keV with gas scintillation proportional counters (the SPC system). which has twice the energy resolution of conventional proportional counters. The study of very soft X-ray sources in the range 0.1-2 keV is performed with XFC (X-ray Focusing Collector). TSM (transient Source Monitor) consists of one-dimensional Hadamard masks (Hadamard X-ray Telescope : HXT) and fan beam scanning counters (ZY Telescope : ZYT). and which monitor a wide-field sky. RBM/GBD (Radiation Belt Monitor/γ-ray Burst Detector). two small scintillation counters. are equipped as a monitor of non X-ray background. and the detection of γ-ray bursts. A detailed description of Tenma is given by Tanaka et al. (1984).

Ⅲ-2. The SPC system.

The X-ray spectra and their temporal variations are measured by the SPC (gas scintillation proportional counter) system developed at ISAS.

The SPC system consists of the ten identical units of gas scintillation proportional counters. Figure 4 illustrates the the SPC for Tenma schematically. It consists of a ceramic gas volume filled with one atm of Xe and 0.2 atm He. and a phototube. and have a 100 μm dome-shaped Be entrance window with 13 cm diameter. The gas volume is divided into 3 regions by two spherical electric grids normally supplied with about 800V and 7000V. respectively. An X-ray photon produces an electron cloud above the first grid (drift region). The electron cloud drifts to the first grid and produces a number of UV photons through gas

scintillation between the first and the second grids (scintillation region). The UV photons are converted into visible light by a terphenyl wavelength shifter. then into an electric signal by the phototube. Figure 5 shows the effective area including the collimator transmission and energy resolution as a function of X-ray energy. Theoretical pulse height distributions for several monochromatic incident radiations are shown on figure 6. Additional details on the SPC are found in Inoue et al. (1982).

The SPC system consists of three groups: SPC A. B and C. The SPC A and B comprise four counters each and are equipped with honeycomb collimators with fields of view of 3.1° and 2.5° (FWHM). respectively. The two counters of SPC-C are equipped with bigrid rotating modulation collimators (RMC) of 34' and 43' with the grid lines of the two perpendicular to each other. The fields of view are defined with honeycomb collimators of 3.8 ° (FWHM). The collimator response functions are shown in figure 7.

The background counts are reduced by rise-time discriminators. About 70% of the non X-ray events are rejected. while 98% of the X-rays are accepted. On board calibration of the energy scale is performed employing Cd^{109} radioisotope (22.1 keV) installed in the window assembly of each counter. which yields a continuous flux of a few counts per second. Various energy ranges can be covered by changing either the high voltage of the counters or the phototubes. as well as by changing the coarse gains of the amplifiers. Adjusting the fine gains of the amplifiers. we can make the energy scales of the counters coincide with each other within an accuracy of 1%.

The X-ray signal is pulse-height analyzed into 256 channels with a pseudo-logarithmic scale (the channel width is constant for channels 0-127. twice as wide for 128-191 and four times as wide for 192-256). The pulse-height spectrum of an SPC is transmitted either in PH (pulse-height) or in MPC (multi-channel pulse-counting) mode. In the PH mode. each detected X-ray event is tagged with 8 bits of pulse-height information and occupies one data word. The 8 bit pulse-height data are sampled 6 times per counter in every minor frame. Since each data word is occupied by only one event. this mode is subject to significant dead time. The maximum read-out rate per counter is 48 and 12 counts/sec for high and low bit rate. respectively. The total counting rate is also transmitted twice in each minor frame for dead time correction. The MPC mode has four different sub-modes. the 128ch. C128ch. 32ch and C32ch modes. The number of energy channels are reduced to 128 or 32. and counts of all channels are read out successively. In the C128ch and C32ch mode (these two sub-modes are for SPC A and B only). the data of four counters in the same group are combined together. In table 2 the time resolutions of each mode are summarized. The performance and its verification of SPC system were described by Koyama et al. (1984).

Ⅲ-3. Data acquisition.

Tracking operations are carried out at Kagoshima Space Center (KSC). Institute of Space and Astronautical Science (ISAS). in Uchinoura. Kagoshima prefecture (131.° 08 E. 31.° 25 N). Ground contacts are available in five consecutive orbits out

of 15 orbits a day. Commands are sent through a 137 MHz up-link. whereas the real-time and stored data are transmitted through 400 MHz U-band and 2280 MHz S-band down-links. Most of the command operations. for example for the performance of the data recorder. for the attitude control. for the bit rate and for other instruments are decided previously at ISAS. in Tokyo. by duty scientists.

At KSC. all the data received from the satellite are recorded on magnetic disks. and mini-computers display on CRT the housekeeping data. attitude data such as direction of the sun. X-ray counting rate and the pulse height spectrum. in real time. The operating status of the various instruments. housekeeping data and X-ray data are dumped out and all the data are saved on magnetic tapes. after the ground contact.

All the data are directly transferred to ISAS through a digital data transmission (DDX) line. and are stored in a computer data base system. Duty scientists at ISAS take care of the satellite. determining the attitude. plotting the time histories of all the data from each instrument as well as preparing the command list.

CHAPTER IV. OBSERVATIONS.

Cygnus X-3 was in the field of view of the SPC system in 1983 September 13-18. and in 1984 September 11-14.

The spectra in 1983 were about a factor of 1.5 brighter in the range 2-6 keV and softer than that in 1984. Therefore. we think that during the observation in 1983 and in 1984. Cygnus X-3 was in its high state and its low state respectively.

In 1983. the data were obtained by the SPC A. B and C. with the C128ch mode. having the energy range of 2-60 keV. The time resolution was 0.5 sec and 2 sec for the high and the low bit rate. respectively. In 1984. the data were obtained by the SPC A and C. with the 128ch mode and roughly in the same energy range. The time resolution was 2 sec and 8 sec for the high and the low bit rate. respectively. The attitude of the satellite was determined by the SPC-C (RMC) and the star sensor for the data in 1983. and by the SPC-C. the sun sensor and the distance from Cygnus X-2 using the ZYT for the data in 1984. The accuracy of the attitude is about 0.1° for 1983 and 0.3° for 1984. Figure 8 and figure 9 show the time history of the locus of the spin axis in the sky during the observation in 1983 and 1984. respectively.

The data obtained in the sky region near Cygnus X-3. where there are no known bright X-ray source. were used for the background data. Figure 10 and figure 11 show the spin axis history during the background observations. Sometimes. some known week X-ray source were in the field of view during the observation of Cygnus X-3 and the background. The X-ray flux of these sources are summarized in table 3. The observed background

flux was about 0.1 counts/sec/cm^2 (2 - 25 keV). and the flux of Cygnus X-3 in the range 2-6 keV. during the observation in 1983 and 1984. was about 0.75 and 0.5 counts/sec/cm^2. respectively. Comparing these results with the value of table 3. the flux of each sources for the contamination is estimated to be less than 10% of the flux of the background and about 2% of the flux of Cygnus X-3. above 2 keV. Therefore. the influence of these sources is ignored.

From the raw data transferred from KSC. applicable data were first selected. The background counts due to cosmic rays are found to be reproducible from the cutoff rigidity if it is greater than 10 GeV/c. At smaller cutoff rigidity. less than 10. the data are removed. because the background count rate can not be reproduced successfully (Koyama et al. 1984). The electron background. which is not predictable. is checked by the RBM/GBD. The data with larger counting rate of RBM/GBD than usual (about 25 counts/sec) are removed. The data during the earth occultations and for Cygnus X-3 near the horizon (angle between the field of view and the direction of the earth's center less than 80°) are removed. The observed times of the selected data are shown in figure 12. which also gives the phase of the 4.8-hour period. which will be determined in Chapter V-1. To determine the energy scale. the spectrum over a small energy range (19-28 keV) is fitted by two Gaussian functions (for the Kα and Kβ lines of the calibration source Cd^{109}) together with an exponential function (for the continuum). After the determination of the energy scale. the counting rates attributable to the calibration source were subtracted.

The spectral data and the background data are arranged according to the cutoff rigidity. and integrated in each rigidity bin of 1 GeV/c. The energy scale of the background data are adjusted to coincide with those of the data of the observation of the Cygnus X-3. From the data in each rigidity bin. the background corresponding to that bin were subtracted. After the correction of the transmission of the collimators. they are added.

CHAPTER V. Data Analysis and Results.

V-1. Light curve and the Ephemeris.

Figure 13 shows the light curve after the background subtraction and the correction for the satellite attitude in the ranges 1-3 keV, 3-6 keV, 6-9 keV and 9-21 keV. The data in 1983 show the 4.8-hour modulation as well as a decrease in the mean level and in the amplitude of the modulation. In this section, we determine the time scales of the decrease of the mean level and the amplitude, and the time of X-ray minimum (T_{min}), using the data in 1983. Finally, we determine the ephemeris of 4.8-hour modulation.

Our data sequences are too short to observe a full cycle of the 4.8-hour modulation. Furthermore, variability of the shape of the light curve from one cycle to the next one has been reported (Leach et al. 1975, Mason et al. 1976, Parsignault et al. 1977, van der Klis and Bonnet-Bidaud, 1982). Therefore, the determination of the period from our data alone is difficult. We used two fixed values for the period at 0h 0m 13 Sept. 1983 (UT): 0.1996885 ± 0.0000011 day (17253.086 ± 0.095 sec) from the ephemeris of van der Klis and Bonnet-Bidaud (1981), and 0.1996900 ± 0.0000026 day (17253.22 ± 0.22 sec) from Elsner et al. (1980). The validity to use these periods is found as follows. The period at 0h 0m 13, Sept. 1983 (UT) derived from our final ephemeris is 0.1996882 ± 0.0000002 day (17253.051 ± 0.017 sec), which is shown later. The difference between this and the assumed period is 0.0000018 day. Since the entire data interval is about 30 cycles, the influence of the difference between these periods

upon the value of T_{min} is about 2.3 seconds ($\sim$0.0001 cycles) which is smaller than the error(0.008 cycles). Other parameters, such as the time scales of the decrease of the mean level and the amplitude, are also insensitive to the exact value of period in this case.

Using the two assumed periods, a least squares fit of the data in the range 1-9 keV was performed to a function of the form:

$$I(t) = A_0 \exp(-(t-t_0)/\tau_1) + A_1 \exp(-(t-t_0)/\tau_2) \sin(2\pi((t-t_0)/P-\Delta)) .$$

where t_0 is a time origin fixed at 0h 0m 13, Sept. 1983 (UT). t is the time from t_0, Δ is the phase at $t=t_0$ and P is the period of the modulation fixed at 0.1996885 day and 0.1996900 day. The first term is the mean level decreasing with the time constant of τ_1 and the second term is the sinusoidal curve with the amplitude decreasing with the time constant of τ_2. The free parameters are A_0, τ_1, A_1, τ_1, and Δ.

The χ^2 statistics was used to establish the best fit (Lampton et al. 1976), which is given as

$$\chi^2 = \sum_i (x_{io}-x_{it})^2/\sigma_i^2$$

where x_{io} is the ith observed data point, x_{it} is the corresponding value of the fitting function and σ_i is the uncertainty of x_{io}. The fit were performed with the data binned in intervals of 80 sec. With the σ_i^2 set equal to the variance due to counting statistics, an extremely poor fit was obtained, χ^2 per degree of freedom being of the order of 800. This is not surprising since Cygnus X-3 is known to be variable on a wide variety of time scales and to show apparent fluctuations in the

shape of the light curve from cycle to cycle. The poor fit to the data was therefore taken to imply that our choice for σ_i grossly underestimate the fluctuations.

We then adopted the following procedure to take account of the observed variability. First we fitted the data with σ_i^2 set equal to the variance due to counting statistics. Next we calculated the root mean square deviation, σ_{rms}, of the data about the best fit curve, obtaining $\sigma_{rms} \sim 51.437$ counts/80sec and 51.431 counts/80sec for the period of 17253.216 sec and 17253.086 sec. respectively. Finally we refitted the data, replacing σ_i with σ_{rms}. This chose for σ_{rms} slightly overestimates the fluctuations because the shape of the light curve intrinsically differs from sinusoidal. Then the errors of derived parameters are slightly overestimated.

In table 4, we list the best fit parameters in the energy range 1-9 keV. The values of the parameter Δ for both the periods are the same. The other parameters are also the same within the errors. The best fit curve for the period of 17253.216 sec is shown in figure 14. The curve for the period of 17253.086 is quite similar to figure 14. The corrected T_{min} referred to the barycenter of the solar system is

$$T_{min}(\text{Tenma}) = \text{JD } 2445590.3923 \pm 0.0016 ,$$

where the error is 1σ level ($\chi^2_{min}+5.9$) according to Lampton et al. (1976). (In this section, all errors are 1σ level according to Lampton et al.(1976).) The decay time scale of the mean level (τ_1) and that of the amplitude (τ_2) are about 11 days and 6 days, respectively. This fact means that the amplitude of the 4.8-hour modulation varies more rapidly than a simple

proportional to the average source level, which was already pointed out by Bonnet-Bidaud and van der Klis (1981).

To make an ephemeris for Cygnus X-3, we compiled the data gathered by Elsner et al. (1980) from several satellite experiments (Leach et al. 1975, Parsignault et al. 1976, Manzo et al. 1978, Lamb et al. 1979), the Copernicus results published by Mason and Sanford (1979) and the Cos-B result by van der Klis and Bonnet-Bidaud (1981). These data are summarized in table 5. These measurements all refer to, or were corrected by the authors to refer to (column 5 in table 5), the T_{min} of the best fit sine wave to the full light curve.

Adding the present T_{min} measurement, we performed a least squares fit to all the data with a constant period hypothesis:

$$\phi = (t-T_0)/P \ .$$

where ϕ is the phase at time t from a time origin T_0, which is defined as the nearest X-ray minimum time to the first time of X-ray minimum reported by Leach et al. (1979), and P is the period. The results are

$$T_0 = \text{JD } 2440949.8868 \pm 0.0004$$
$$P = 0.19968561 \pm 0.00000004 \text{ day}$$
$$\chi^2/\text{D.O.F.} = 215.9/59 \ .$$

The results of a parabolic fit of the form :

$$\phi = (t-T_0)/P - ((t-T_0)/P)^2\dot{P}/2 \ ,$$

are

$$T_0 = \text{JD } 2440949.8979 \pm 0.0005$$
$$P = 0.19968314 \pm 0.00000005 \text{ day}$$
$$\dot{P} = (1.08 \pm 0.03) \times 10^{-9} \text{ sec/sec}$$
$$\chi^2/\text{D.O.F.} = 80.3/58 \ .$$

The value of χ^2 is large even if we use the parabolic formula. Mason and Sanford (1979) determined the minimum intensity time using about 2 cycles. Since variability in the shape of the light curve has been reported, it is possible that their data have larger errors than those cited by them. Therefore, excepting their data, we recalculated the fitting. The results of the constant period hypothesis are

$$T_0 = \text{JD } 2440949.8890 \pm 0.0007$$
$$P = 0.19968559 \pm 0.00000005 \text{ day}$$
$$\chi^2/\text{D.O.F.} = 115.8/19 \quad .$$

This hypothesis is rejected with 99.5 % confidence level. Using the parabolic formula, the results are

$$T_0 = \text{JD } 2440949.9038 \pm 0.0009$$
$$P = 0.19968260 \pm 0.00000006 \text{ day}$$
$$\dot{P} = (1.20 \pm 0.03) \times 10^{-9} \text{ sec/sec}$$
$$\chi^2/\text{D.O.F.} = 13.97/18 \quad .$$

Figure 15 and figure 16 show the residuals from the best-fit curves for the constant period and the parabolic formula, respectively, except for the Copernicus data (Mason and Sanford, 1979).

Through this work, the phase of the 4.8-hour period is derived from this ephemeris and phase 0 means the minimum intensity phase.

Figure 17 shows the folded light curves in the range 3-6 keV and 6-9 keV and the hardness ratio (intensity in the range 6-9 keV / intensity in the range 3-6 keV), with this period. From this figure, we found that:

① Around the phase 0, the spectra are harder than the

other phase.

② In 1984, the spectra are harder than that in 1983.

③ The light curve is asymmetric with a sharp fall to X-ray minimum followed by a gradual rise as pointed out by previous authors.

④ The intensity around phase 0.5 shows a large scattering. This is due to the decreases of the mean level and the amplitude of the modulation.

V-2. Spectra and Spectral variations.

In order to analyze the spectral variation depending on the 4.8-hour modulation, the data were integrated for the phase intervals, 0.875-0.125, 0.125-0.375, 0.375-0.625 and 0.625-0.875 over three parts of the data, the first half (before Sept. 16 0h 0m UT), the latter half (after Sept. 16 0h 0m UT) in 1983 and in 1984, respectively. Figure 18 shows the observed spectra after background subtraction and aspect correction, which were convolved with the detector response. The following facts may be drawn from figure 18 :

① There is a strong excess around 6-7 keV.

② There appears to be a shallow dip around 9 keV.

A sensitive model-independent indicator of the spectral variability is the ratio of the count rate in each energy channel of one spectrum to that of another one (PHA ratio). Figure 19 shows the PHA ratios of the spectra in the phase 0.875-0.125, 0.125-0.375 and 0.625-0.875 to that in the phase 0.375-0.625, which is the approximate phase of the X-ray maximum intensity in the 4.8-hour cycle, in the first half in 1983. Figure 20 and

figure 21 show the same PHA ratios of the spectra in the latter half of 1983 and in 1984. From these, we can find the following facts :

③ There is a relative excess around 6-7 keV in the phase 0.875-0.125.

④ The amplitude of the modulation is maximum around the energy 3 keV.

⑤ There is a large difference between the spectral shapes of the phase 0.875-0.125 and that of the phase 0.375-0.625.

⑥ The spectral shape above 15 keV varies, and its variation appears to be independent of the phase.

The fact ③ indicates that the equivalent width of this feature is larger in the phase 0.875-0.125 than the other phases.

Figure 22 and figure 23 show the PHA ratios between the data in the first half and that in the latter half of 1983 , and between the spectra in 1984 and the averaged spectra of the first and the latter half of 1983, for each phase interval, respectively. From figure 22 and 23, we found that:

⑦ The difference between the spectral shape of the first half and that of the latter half in 1983 is mainly the decrease of the intensity below 6 keV, excepting the irregular change above 15 keV.

⑧ The spectra in 1984 are harder than that in 1983.

⑨ The PHA ratios of the data in 1983 to those in 1984 show an excess around 6～7 keV comparing the neighbouring region. This means the equivalent width of the feature around 6～7 keV in 1984 is larger than that in 1983.

To compare these spectral variation with some physical

phenomena, figure 24 shows simulated PHA ratios, derived from the variation of the absorption column density both of (a) the neutral gas (Brown and Gould 1970 and Fe I), and of (b) the partially ionized gas of He-like Mg, Si, S, A, Ca, Cr, and Fe with cosmic abundance (Allen 1973) and Comptonization by the electrons of the temperature of 10 keV. In this simulation, the incident spectrum was assumed to be a blackbody spectrum of the temperature of 1 keV which roughly represents the spectral shape in 1983. Although the partially ionized gas assumed above is not self consistent ionization state, this will roughly resemble the expected PHA ratios resulting from the variation of the absorption column density of the actual ionized gas in the short energy ranges for 2-5 kev (mainly due to Si and S) and above 7 keV (mainly due to Fe), separately. From the comparison between the data and the simulation, the following results are found:

⑩ The observed PHA ratios of the phase 0.875-0.125 to the phase 0.375-0.625 show the gradual increase in the range from 3 keV to 15 keV against the steep increase in the range from 3 keV to 9 keV of the simulated PHA ratios derived from the variations of the absorption column density of the neutral gas and the partially ionized gas. Therefore the spectral variation corresponding to the 4.8-hour modulation can not result from the variations of absorption column density in either the neutral gas or the He-like partially ionized gas. One possible cause of this change above 3 keV is Comptonization by a hot plasma. The increase of the PHA ratio below 3 keV suggests the existence of a low-energy component which undergoes less modulation (Becker et al.

1978, White and Holt 1982).

⑪ The difference between the spectra of the first half and the latter half in 1983 resembles the difference resulting from the variation of the absorption column density of neutral gas.

⑫ The difference between the spectral shape of the data in 1983 and in 1984 can not be due to the change of the absorption column density in either the neutral gas or the He-like partially ionized gas. One possible cause of the variation except for the data above 15 keV is Comptonization by a hot plasma.

V-3. Model fitting of the observed spectra.

The model fitting was carried out according to the method described by Koyama et al. (1984).

The spectrum of Cygnus X-3 shows an excess around 6-7 keV and a tendency toward a shallow dip near 9 keV, as shown in V-2. Therefore, in order to determine the continuum spectrum, the model spectra of combinations of the simplest models : blackbody, power law and thermal bremsstrahlung spectra attenuated by photoelectric absorption (Brown and Gould, 1970 and Fe I assuming cosmic abundance (Allen, 1973)), were fitted to the spectral data , excepting the data of the energy range of 6-7 kev and 9-12 keV,

A black body spectrum is given as,

$$I(E) = (S/4\pi D^2)0.988\times10^{32}4\pi r^2(E^2/(\exp(E/kT)-1))$$

photons/sec/keV,

where S is the area of the detector, D is the distance to Cygnus

X-3, kT is the temperature of the emission region, which is assumed to be a sphere of the radius r, and E is the energy of a photon in keV.

A power law spectrum is given as,

$I(E) = (S/4\pi D^2)\ A\ E^{-\alpha}$ photons/sec/keV.

Thermal bremsstrahlung spectrum is given by Matteson (1971) as,

$$I(E) = (S/4\pi D^2)V\ 3.03\times10^{-15} n_e n_z (Z^2/(kT)^{1/2}) g$$
$$\exp(-E/kT)(1/E) \text{ photons/sec/keV},$$
$$g = 1.04(kT/100)^{0.125}(E/kT)^{-0.31(kt/100)^{-0.19}}$$

where V is the volume of the emission region, n_e and n_z are the density of electrons and ions, Z is the mean ion charge. Tucker and Gould (1966) showed $n_e n_z Z^2 = 1.3 n_e^2$ for an object with cosmic abundance. The formula using this fitting includes slight correction of the electron-electron thermal bremsstrahlung in the non-relativistic limit (Maxon and Corman, 1967).

Table 6 shows the trial models and χ^2 values. To investigate the general variation of the X-ray spectrum, the fitting with a complex model is not useful, because the increase of the number of the parameters of the model obscures the general trend of the variation. Among the one-component models, the black body spectrum gives the smallest χ^2 values to the data in 1983. If we exclude the data above 9 keV, the black body spectrum can also roughly represent the data in 1984. Therefore we fitted the blackbody spectra to all the data below 9 keV, excepting the data of energy range 6-7 keV.

Figure 25 shows the best fit parameters and in table 8 we

summarize those as well as χ^2 values. We can find that:

① The radius of the black body is modulated by a factor of about 2. The radius in 1984 is less than that in 1983.

② The temperature shows 4.8-hour modulation and is highest around phase 0. The temperature in 1984 is higher than that in 1983.

③ The phase related change in absorption column density is about 2×10^{22} H atoms/cm^2 and the column density is small around phase 0. The column density in the latter half in 1983 is larger than that in the first half in 1983. and that in 1984 is the smallest among the three parts.

The modulation of the absorption column density changes the spectral shape (figure 24.). However, the smaller absorption column density at phase 0 should give a softer spectral shape at the phase 0 than that at the other phases. This is contrary to the observed spectral variation.

V-4 Iron lines

It is natural to assume that the excess around 6-7 keV is due to iron emission lines, because iron has its large cosmic abundance among the chemical elements which emit X-ray lines around 6～7 keV. In this section, the intensity, the central energy and the width of this iron feature will be determined. Since the parameters are sensitive to the assumed continuum spectrum, we must use as a good model spectrum for the continuum one as possible.

As shown in table 6, one-component or two-component spectra cannot sufficiently simulate the spectrum of Cygnus X-3. In the

three component model (black body + power law + thermal bremsstrahlung), the reduced χ^2 values range from about 1 to 5. Therefore, we use the three component model for the continuum spectrum. The best fit parameters of the three component model are summarized in table 7. The best fit three-component model spectra and the observed data as well as the residuals from the model spectra are shown in figure 26. We can easily find the excess around 6.7 keV and the shallow dip near 9-10 kev.

To get the intensity, the central energy and the width of the iron feature, the three component models plus a Gaussian distribution for the iron feature were fitted to the spectral data excepting the data of energy range 9-12 keV, because of the tendency toward a shallow dip. In this fitting, the temperatures of the black body and the thermal bremsstrahlung and the power law index are fixed to the values shown in table 6. Figure 27 shows the data and the best fit model spectra. The best fit parameters for the iron feature and the continuum counts rate at 6.7 keV are shown in figure 28. The best fit parameters are also summarized in table 9. We can summarize the properties of the iron feature as follows :

① The intensity appears to be phase independent, especially in 1983.

② The equivalent width is clearly modulated with the 4.8-hour cycle.

③ The central energy is 6.7 ± 0.1 keV.

④ The width is about 0.4～0.8 keV (FWHM), and shows a tendency to increase at phase 0.25.

⑤ The intensity observed in 1984 is about twice that

observed in 1983.

Although the intensity of the feature appears to be phase independent, it is not constant. Then, we reanalyze the iron feature properties. First, the data in 1983 observation are divided into five parts, (a), (b), (c), (d) and (e), as shown in figure 13, and then integrated over each part. The intensity, central energy and width are determined in like manner. The results are shown in figure 29. From this figure we can find that:

⑥ The intensity is variable on a time scale of less than one day, though the central energy and the width are almost constant.

Second, in order to investigate more short time variability, the data of individual orbits of the satellite, lasting about 5 to 20 minutes, are also analyzed in the same way. Figure 30 shows the history of the iron properties. The folded data with the 4.8-hour period are shown in figure 31. Following facts may be inferred from figure 30 and figure 31:

⑦ The intensity is variable on a time scale of several hours.

⑧ The centroid of the iron feature has a tendency to shift toward 6.65 keV at phase 0.0 and toward 6.75 keV at phase 0.5.

The centroid of the iron feature at 6.7 keV implies that the ionization state of the iron ion is mainly He-like. The emission could either be a thermal or via a fluorescence mechanism. The fact that the line intensity does not show the 4.8-hour modulation indicates that the main origin of the iron lines is

different from that of the continuum X-rays. This favors the fluorescence emission of the lines. If the emission mechanism is fluorescence, we can expect that the line intensity should correlate with the continuum intensity above 8.8 keV. Figure 32 shows the relation between the iron feature intensity and the flux in the range 9-10 keV of the data divided into 4 phase intervals and three parts of the observation. They reveal a rough correlation. Further, we can expect the intensity of iron feature to correlate to the mean intensity averaged over 4.8-hour modulation above 8.8 keV, because there is no modulation of the iron feature intensity. The data divided into 5 parts, (a) to (e) in 1983 observation and an integrated data through the 1984 observation were used. The mean intensity was determined by a least squares fit of the light curve in the range 9-10 keV to a sine curve. Figure 33 shows the relation between the iron feature intensity and the mean intensity in the range 9-10 keV, and we can find good correlation. This correlation strongly suggests that the emission mechanism of the iron lines is the fluorescence, and that the plasma emitting iron lines is not influenced by the 4.8-hour modulation except for the slight change of the centroid and the width.

V-5. Absorption Edge.

It is reasonable that the emission mechanism of the iron line is the fluorescence, as shown in the previous section. The centroid of the iron feature is about 6.7 keV. Then, we think that the shallow dip around 9 keV is due to the absorption edge of He-like iron ions. The cross section of the He-like iron is

given by Bethe et al. (1957):

$$\sigma(E) = 2 \times (6.3 \times 10^{-18})/25.7^2 \times (E_{th}/E)^{2.84} \ cm^2 ,$$

where E_{th} is the threshold energy of K edge. Using this cross section and the three-component model, we perform a model fitting to the spectrum in the range 8-15 keV. The results are shown in figure 34. We can summarize the property of the absorption edges as follows:

① The column density assuming the cosmic abundance is about $10^{23.4 \pm 0.2}$ H atoms/cm^2 and $10^{23.4 \pm 0.5}$ H atoms/cm^2 for 1983 and 1984, respectively.

② The edge energy is about 9.1 ± 0.2 keV and 9.2 ± 0.5 keV for 1983 and 1984, respectively.

③ There are no clear phase dependence of the absorption column density and the edge energy.

The relation of the absorption edge and the iron feature will be discussed in the next chapter.

CHAPTER VI. Discussion

VI-1. Period change.

The period derivative, $\dot{P}$, of the 4.8-hour modulation is $\sim 10^{-9}$ sec/sec, which is consistent with the values derived by van der Klis and Bonnet-Bidaud (1981) and by Elsner et al.(1980). The period, P, is $\sim$17253 sec, then $\dot{P}/P$ is $\sim 7 \times 10^{-14}$ sec^{-1}. In the X-ray binaries, the stable periodicity is due to either the orbital revolution or the rotation of an X-ray star. X-ray pulsars are generally believed that their pulses are due to the rotation of the X-ray star. They have been investigated in detail. The period and $\dot{P}/P$ of X-ray pulsars range from 0.03 sec to 835 sec (Bradt and McClintock, 1983) and from 10^{-12} to 10^{-11} (Nagase et al. 1984), respectively. In comparison with X-ray pulsars, the period of Cygnus X-3 is an order of magnitude longer and $\dot{P}/P$ is an order of magnitude shorter. From these facts, many authors believe that this period is due to the orbital motion.

If we assume that the 4.8-hour period is due to the orbital motion, we can roughly estimate the radius of the orbit. The separation, a, is given by,

$$a^3 = (1/(2\pi))^2 \; P^2 \; (M_X + M_C) \times G \; , \qquad (1)$$

where M_X and M_C are the mass of an X-ray star and a companion star, respectively, and G is the gravitational constant. If the companion star is a main sequence star of $M_C \leqq 1.0 M_\odot$, which approximately fills its critical Roche lobe, and $M_C/M_X < 0.8$, the radius of a companion star is (Robinson, 1976)

$$R_C \sim 0.93 \; (M_C/M_\odot) \; R_\odot \; , \qquad (2)$$

where $M_\odot$ is the solar mass and $R_\odot$ is the solar radius, respectively. The radius of the critical Roche lobe is (Paczynski 1971),

$$R_c/a = 0.46\ (M_c/(M_x + M_c))^{1/3}. \qquad (3)$$

Then, we find that

$$M_c \sim 3.5\times10^{-5}\ P\ M_\odot$$
$$\sim 0.6\ M_\odot \quad . \qquad (4)$$

Assuming the X-ray star is a neutron star, i.e. $M_x \sim 1.4\ M_\odot$, the separation and the radius of the companion star are obtained as,

$$a \sim 1.2 \times 10^{11}\ \text{cm}\ , \qquad (5)$$

$$R_c \sim 2.8\times10^{10}\ \text{cm}\ . \qquad (6)$$

These results are uncertain because the assumptions, $M_c \leqq 1.0 M_\odot$, $M_c/M_x < 0.8$ and a companion star of a main sequence star, have not been demonstrated explicitly by observations.

If the period of 4.8-hour modulation is due to the orbital motion, what causes the period derivative, $\dot{P}/P \sim 7\times10^{-14}$ sec^{-1}? The change of orbital period due to mass transfer between members of a binary system is given by (e.g. Pringle, 1975)

$$\dot{P}/P = \left(3(M_c-M_x)/(M_cM_x) \right) \dot{M}_c\ . \qquad (7)$$

If the X-ray emission from Cygnus X-3 results from the accretion onto a neutron star, the mass accretion rate required to produce the observed luminosity ($L_x \sim 10^{38}$ erg/sec) is

$$\dot{M}_c \sim -5 \times 10^{17}\ \text{gram/sec}\ . \qquad (8)$$

Thus, the period change is , using M_c and M_x of 0.6 $M_\odot$ and 1.4 $M_\odot$,

$$\dot{P}/P \sim 7 \times 10^{-16}\ \text{sec}^{-1}\ , \qquad (9)$$

and this value is too small.

When the system reveals the mass loss, the orbital period is changed. If we make the plausible assumption that the mass which is lost by the system carries away the angular momentum it had when it was part of the companion star, the period change is given by (Davidsen and Ostriker, 1974),

$$\dot{P}/P = -2 \times \dot{M}_C/(M_X+M_C) \ . \qquad (10)$$

The mass loss rate required to explain the period derivative is

$$\dot{M}_C \sim -10^{-5\sim-6} \ M_\odot/\text{year}. \qquad (11)$$

This value is too large for a main sequence star. Such a value is only revealed by some peculiar stars; Of stars and Wolf-Rayet stars etc. However, Davidsen and Ostriker (1974) argued that once the wind got started, electron scattering trapped photons, some of which found their way to the companion star and thus fed the wind even if the companion star was a red dwarf. In the very thick wind, the companion star was illuminated by X-rays on all sides and was literally being boiled away. And they introduced the mass loss rate of $\sim 10^{-6} \ M_\odot$/year.

Another possibility of the period derivative of $\sim 10^{-9}$ sec/sec is the apparent change by the apsidal motion of an elliptical orbit. If the system is observed over a span of time shorter than the period of apsidal motion, P_{aps}, then the periodic nature of these changes may not become apparent. Indeed, for a sufficiently short span of observations during certain parts of the apsidal cycle, these changes would appear as monotonic increases or decreases of period. This phenomenon was discussed by Elsner et al.(1980) and Ghosh et al. (1981). They argued that the elliptic orbit hypothesis explained the observed asymmetry in the average X-ray light curve.

Our data show that the period appears as monotonic increase over about 10 years (figure-16.). The average X-ray light curve of our data also shows the similar asymmetry with previous observations, i.e., a sharp fall to X-ray minimum followed by a gradual rise (figure-17.). Therefore, if the period derivative is mainly due to the apsidal motion, the period of the apsidal motion, P_{aps}, is larger than 40 years. As shown by Elsner et al. (1980) and Ghosh et al.(1981), this period rules out all main sequence companion stars and the most plausible companion star is a pure helium star.

VI-2. Emission region of iron lines.

The strong iron feature of Cygnus X-3 has been pointed out by many authors. Our results about iron lines from Cygnus X-3 are summarized as follows:

① The intensity appears to have no modulation of 4.8-hour period, especially in 1983.

② The intensity correlates strongly with the mean intensity during the 4.8-hour period in the range 9-10 keV.

③ The centroid of the energy is about 6.7 keV, and it has a tendency to shift toward 6.65 keV at phase 0.0 and toward 6.75 keV at phase 0.5.

④ The width is about 0.4～0.8 keV and shows a tendency to increase at phase 0.25.

⑤ The intensity is about 0.015 counts/sec/cm^2 in 1983 and about 0.025 counts/sec/cm^2 in 1984.

⑥ The intensity varies in the time scale of several hours. The spectra reveal the shallow dip around 9 keV. Assuming that it

was due to the absorption edge of He-like iron ions, following facts were derived in the previous chapter:

⑦ The edge energy is about 9 keV. The energy is consistent with the energy of the K-edge of He-like iron ions.

⑧ The column density of absorption edge of He-like iron ions corresponds to about $\sim 10^{23.4}$ H atoms/cm^2 with the cosmic abundance of iron.

The facts, ② ,⑦ and ⑧, suggest that the emission mechanism of the iron feature is fluorescence of the plasma irradiated by X-rays. The iron feature intensity, by fluorescence of an open uniform gaseous shell located at a radius r from the neutron star and subtending a solid angle Ω, is estimated according to Basko (1980), in appendix A. The results show that the intensity of the iron feature emitted by the plasma has the upper limited value* given by

$$I_{Line} \sim 30 \int_{Eth}^{\infty} I(\varepsilon)/\varepsilon^{2.84}\, d\varepsilon \;\; \tau_T \Omega Y_{Fe} \quad \text{(photons/sec)}, \qquad \text{(A-12)}$$

where $I(\varepsilon)$ is the spectral shape, τ_T is Thomson scattering depth of the shell and Y_{Fe} is the ratio of the iron abundance of the plasma to the iron cosmic abundance.

We think that the spectrum in the phase 0.125-0.375 reveals the mean spectrum of Cygnus X-3. The spectrum in the range 8-15 keV resembles by

$$I(\varepsilon) = 1.1 \times 10^3 \times \varepsilon^{-4.9} \times 4\pi D^2 \text{ photon/sec/keV}, \qquad (12)$$

for the data in 1983, and

---

* The value is the upper limit by two reasons: (1) all iron atoms are assumed to be in He-like ions, (2) it is assumed that all the line photons finally escape as K-α photons.

$$I(\varepsilon) = 3.69 \times \varepsilon^{-2.28} \times 4\pi D^2 \text{ photons/sec/keV}, \quad (13)$$

for the data in 1984, where D is the distance to Cygnus X-3.

The column density of the absorption edge due to the He-like iron ions corresponds to about $10^{23.4}$ H atoms/cm^2 assuming that the abundance of the He-like iron ions is the cosmic abundance. This value is derived neglecting the Lyman continuum emission. This emission makes the depth of the absorption edge smaller. Taking account of this effect, we simulate the relation of the observed column density and the edge energy to a true column density. If we assume the spectral shape (12) and (13) and the true absorption column density of He-like iron ions, we can simulate the expected spectra using the photoelectric cross section given by equation (A-9) and the Lyman continuum intensity given by equation (A-13). The absorption column density and the edge energy expected to be observed are estimated by the least square fit of the simulated data assuming that the shallow dip is due to only the absorption edge. In figure 35, the results, in case of $\Omega = 4\pi$, $Y_{Fe} = 1$, are shown. From the figure 35, we can find that the true column density is about $10^{23.5}$ H atoms/cm^2. This figure also explains the edge energy observed about 9 keV.

These absorption column density was derived from the absorption edge around 9 keV assuming the cosmic abundance. When we take account to Y_{Fe}, we should write $N_H/Y_{Fe} \sim 10^{23.5}$. Using the equation (A-12), the spectral shapes (12) and (13) and the column density $N_H/Y_{Fe} \sim 10^{23.5}$, the expected iron feature intensities of the plasma with $\Omega = 4\pi$ are

$$I_{Line}/(4\pi D^2) \sim 0.007 \text{ counts/sec/cm}^2$$

$$I_{Line}/(4\pi D^2) \sim 0.011 \text{ counts/sec/cm}^2,$$

for 1983 and 1984, respectively. This value is about half of the observed intensity. In this discussion, we assume that the emission and the plasma are both spherical symmetric. However, since there is a companion star, the plasma may not be spherical symmetric. The density may be denser near the companion star, so that the plasma near the companion star can emit the iron lines more efficiently. If we assume that the typical Thomson scattering depth, τ_T, is about 2 and the solid angle from the compact star is about $0.1 \times 4\pi$, the observed intensity of the iron feature can be explained.

In the following, we examine the structure of the plasma emitting the iron lines. The column density is about $10^{23.5}$ H atoms/cm^2. This means that

$$nR \sim 10^{23.5}, \qquad (14)$$

where n is the number density and R is the thickness of the plasma. The centroid of the feature with about 6.7 keV and the energy of the absorption edge of about 9keV imply that the ionization state of the iron ions is mainly He-like. The ionization state for an optically thin gas irradiated by a point source of X-rays is approximately specified by a single parameter (Tarter et al. 1969),

$$\xi = L_X/(nR'^2), \qquad (15)$$

where L_X is the luminosity of the X-ray source, R' is the distance from the X-ray source. In the region where the iron ions are mainly Fe XXV, the value of ξ is about $10^{2.5\sim3.5}$ (Kallman and McCray 1982). Assuming $L_X \sim 10^{38}$ erg/sec, we obtain

$$nR'^2 \sim 10^{34.5\sim35.5}. \qquad (16)$$

In case of $R \sim R'$, we can get the density and radius as

$$R \sim R' \sim 10^{11 \sim 12} \text{ cm} \quad (17)$$

$$n \sim 10^{12.5 \sim 11.5} \text{ cm}^{-3} . \quad (18)$$

Since the separation is about 10^{11}cm, the radius $10^{11 \sim 12}$ cm is consistent with the no modulation of the intensity of the iron feature if we assume that the cause of the 4.8 hour-modulation is the orbital motion. If a fraction of the iron feature is emitted from the matter near the companion star, it may also show little modulation in the model described in VI-4, because the enshrouding matter is nearly spherical symmetric from the center of the companion star. The modulation of the centroid of the iron feature will be discussed in VI-4.

VI-3. Spectral variation and previous proposed models.

The spectral variation according to the 4.8-hour period is shown in figures 19, 20 and 21. This variation is not due to the change of the absorption column density, but is rather due to the change of the temperature when we fit the spectrum with a black body spectrum. Before this work, the observation of the spectral variation according to the 4.8-hour period was poor, and the previous proposed models have not yet been examined sufficiently, on this point of view. In this section, we examine the several proposed models comparing with our results.

① Reflection model

This model was proposed and investigated by Basko et al. (1974). The expected spectrum reveals a large iron absorption edge around 7.2 keV and K-α emission feature around 6.6 keV. In our data, the iron absorption edge around 7.2 keV is not clear. They consider two components of the spectrum, the reflection on the surface of the companion star and the scattering at the hot extended layer which is the evaporating gas produced by the interaction of X-rays with the atmosphere on the companion star. Their calculation shows that the scattered component is softer than the reflected components below 20 keV. Since the fraction of the scattered component may be larger near the phase 0, the expected spectrum near the phase 0 must be softer than the other phase. This is inconsistent with our results; the spectrum around phase 0 is harder than that at other phase.

② Stellar wind model.

Pringle (1974) and Davidsen and Ostriker (1974) proposed this model. Both of them predicted that the absorption column density must be variable, i.e. the absorption column density is maximum at the phase 0. The present observation shows that the absorption column density is rather minimum at phase 0. when we fit the spectrum with a black body spectrum.

Hertz et al. (1978) performed the Monte Carlo simulation for this model of the five case of the cloud with different density distribution and ionization state. They showed that for the cloud with O I and Fe I the expected spectrum reveals a large 7.1 keV absorption edge and the light curve in the range 1-3 keV shows a narrower maximum than that in the higher energy range. Our data do not reveal these features.

For the cloud including Fe XXVI. with a scattering depth of about unity, which is measured from the surface of the companion star to the point of 4 times larger than the separation, the expected light curve resembles the observed one, and the expected spectrum shows an iron feature around 6.9 keV and an absorption edge around 9.2 keV. Although the equivalent width of the iron feature reveals to be slightly enhanced in the phase around 0, the variation is smaller than that of our observation, which shows the modulation by a factor of about 2.

For the cloud including only Compton scattering, the light curve of Cygnus X-3 can be explained when the scattering length of the cloud is greater than about unity.

If the cloud is fully ionized and has a high temperature (about several tens keV) in the inner region on the orbital

scale, it is expected that the iron lines emitted in more outer layer and its intensity is not modulated. The spectral variation, harder spectrum around phase 0, also can explain by Comptonization of the hot cloud. This model will be discussed in the next section.

③ Cocoon model.

Milgrom (1976) and Milgrom and Pines (1978) proposed this model, and Hertz et al. (1978) examine this model with a Monte Carlo simulation. Hertz et al.(1978) showed that a comparable shape of the modulation of the Cygnus X-3 light curve was obtained, when the scattering length was greater than 2, the companion radius was 0.6 times the separation and the photoelectric absorption occurred within part or all of the shell.

If there is the photoelectric absorption within all of the shell, and the scattering length is greater than 2, the absorption column density is greater than 10^{24} H atoms/cm^2. This is inconsistent with our results.

On the other hand, when the absorption occurs within a part of the shell, i.e. a shade of the shell, it is expected that the absorption column density at the phase 0 is larger than that at the other phases. This is also inconsistent with our results.

④ Accretion Disk Corona (A.D.C.) model.

White and Holt (1982) proposed this model. They said that the broad iron feature ($\sim$ 1 keV) was one of the consequence of the presence of the optical thick A.D.C.. If the iron lines are

emitted from the A.D.C., the flux of the iron feature must be modulated as the continuum flux. In other words, the equivalent width of the iron feature is expected to show no 4.8-hour modulation. This is inconsistent with our results. Therefore, most of the iron lines should not be emitted from the A.D.C. but from a more extended region than the A.D.C., for example, in order to have less modulation by the eclipse by the bulge of the disk.

The spectral shape variation of the 4.8-hour modulation was not considered by them. If we take account of only the eclipse by the disk bulge, the spectral shape can not be modulated. To explain the spectral variation of the 4.8-hour modulation, we must introduce another mechanism. For example, the A.D.C. is asymmetric by some reason, and has a higher temperature than the X-ray emitting region of the neutron star. Comptonization in the A.D.C. makes the spectrum become harder when the X-rays escape from the A.D.C. The spectral variation of the 4.8-hour modulation is due to the change of the scattering depth of the asymmetric A.D.C.

As shown above, without some modification, none of these models can explain the observed behavior of Cygnus X-3. The stellar wind model and the A.D.C. model are most plausible among these models. In the next section, we will propose and discuss the hot gas model which improves the previous stellar wind model (Pringle, 1974 ; Davidsen and Ostriker, 1974).

VI-4. Hot gas model.

One model for the sinusoidal light curve of Cygnus X-3 is

that the binary source Cygnus X-3 is enshrouded with matter which have the scattering depth of order of unity. The constant iron feature intensity in the 4.8-hour period suggests that the cloud emitting the iron lines is not influenced by the cause of the 4.8-hour modulation which may be the orbital motion. The harder spectrum around the phase 0, which can not be resembled by the change of the absorption column density with either a neutral gas or a partially ionized gas, implies the presence of high temperature cloud which is modulated in the 4.8-hour period.

Therefore, we present the following model. Cygnus X-3 is a close binary system containing a neutron star and a normal companion star which has the separation of about 10^{11}cm. The system is enshrouded with the matter, whose scattering depth from the surface of the companion star to infinity is several. The X-rays and γ-rays are emitted around the neutron star. The matter in the inner region on the orbital scale is fully ionized and has a high temperature (several tens keV) by the energy supply of mainly γ-rays. The iron lines are emitted from the outer region of the orbital size and from the matter near the companion star. The scattering by the enshrouding matter makes the light curve of the X-rays sinusoidal. Around the phase 0, we see mainly the scattered component by the hot gas and the spectrum is harder than the other phase.

In the following, we discuss this model in more detail.

① Enshrouding matter.

Davidsen and Ostriker (1974) assumed that the density distribution of the gas cloud is spherically symmetric with

respect to the companion star and decreases as r_*^{-2}, where r_* is the distance from the center of the companion star. Furthermore, we assume the scattering depth from the point of $r_* \sim 10^{11}$ cm to infinity is about 2, in order that the X-ray light curve is modulated as we observed (Hertz et al. 1978). Therefore, we can write the density distribution as

$$n(r) \sim 3 \times 10^{13} / r_{*11}^{2} \ \mathrm{cm}^{-3}. \qquad (19)$$

where $10^{11} r_{*11} = r_*$.

One of the possible origin of the enshrouding thick matter is a large mass loss rate, $\dot{M} \sim 10^{-5 \sim -6} M_\odot$/year, of the companion star, which can explain the period derivative of $\sim 10^{-9}$ sec/sec, by some mechanisms for example evaporation by the X-ray illumination (Basko et al. 1977).

Second possible origin of the enshrouding matter is the hydrogen rich envelope of a He-star companion (van den Heuvel and de Loore, 1974). This assumption can also explain the period derivative by the apsidal motion, as shown by Elsner et al.(1980) and Ghosh et al.(1981).

Third possible mechanism is the Roche lobe overflow, whose rate is too large to accrete the neutron star. The matter lost by the primary is expected to suspend around the system and to enshroud the entire system.

Although we can not decide the origin of the enshrouding matter, we assume the density distribution of equation (19) in this discussion.

② X-ray heating.

This matter is always irradiated by X-rays and γ-rays

emitted from around the neutron star.

For an optically thin gas irradiated by a point source of X-rays, the ionization state and the temperature of any local region is roughly determined by a single parameter (Tarter et al. 1969)

$$\xi = L_X/(nr^2) \quad , \tag{20}$$

where L_X is the luminosity of the X-ray source, n is the local atomic number density of the gas and r is the distance from the X-ray source. Assuming the density distribution of equation (19), the atomic number density is given by

$$n(r) = n_X D^2/r_*^2 \quad , \tag{21}$$

$$n_X \sim 3\times10^{13}(D/10^{11})^{-2} \ cm^{-3} \quad , \tag{22}$$

where n_X is the ion number density at the orbit of the X-ray source, D is the separation, and r_* is the distance from the center of the companion star. According to the definition of Hatchett and McCray (1977),

$$\xi = L_X/(n_X D^2)\ q \quad , \tag{23}$$

$$q = (r_*/r)^2 \quad . \tag{24}$$

Therefore, the value ξ is determined by the variable q. The lines of a constant q in the orbital plane are illustrated in figure 36. Assuming $L_X \sim 2\times10^{38}$erg/sec, we obtain

$$\xi \sim 0.6 \times 10^3 \ q \quad . \tag{25}$$

At $q\sim$ 0.5 - 5, the value of ξ is about $10^{2.5\sim3.5}$ and the ionization state of iron ions is there mainly He-like and lower Z elements are almost fully ionized (Kallman and McCray 1982). The temperature is about 10^6K. In the nearer region to the X-ray source ($q > 5$), the iron ions are almost fully ionized.

The modulation of the centroid of the iron feature, which

has a tendency to shift toward 6.65 keV at phase 0.0 and toward 6.75 keV at phase 0.5,(figure 31) can be qualitatively recognized by figure 36. The hemisphere containing the companion star has smaller value of q, and in that the iron ions are less ionized. Around phase 0, we observe Cygnus X-3 from the hemisphere containing the companion star, so that the iron lines from the hemisphere containing the companion star are mainly observed, because the iron lines emitted from the farther hemisphere will escape most readily in the opposite direction to the observer by the scattering, and then the centroid of the iron feature is lower than that in other phase.

In above discussion, the effects of Compton scattering and pair production by γ-rays are neglected. As shown in the next subsection, when we take account of these effects, the plasma near the neutron star becomes hotter and the fully ionized region becomes larger. However, in the more outer region, the effects of Compton scattering and pair production by γ-rays are smaller than that of the free-free, bound-free, free-bound and bound-bound transition, so that the ionization state of the plasma can be determined by the variable q. After all, the energy shift of the iron feature is still expected.

③ γ-ray heating.

In this subsection, the effect of Compton scattering and pair production by γ-rays are examined, including the effect of the thermal bremsstrahlung.

The observed γ-ray spectrum was given as (Samorski and Stamm ,1983)

$$N(>E)=(6.4\pm3.6)\times10^{-7}(E/10^{9})^{-1.108\pm0.021}$$

photons/cm^2/sec. (26)

Assuming that the distance to Cygnus X-3 is 12 kpc, we obtain

$$I(E)\sim 4.0\times10^{41}(E/10keV)^{-2.1}\ photons/sec/eV\ . \quad (27)$$

However, Hermsen(1984) reported that the upper limit of the γ-ray flux at 70 MeV < E < 5000 MeV was 1.0×10^{-6} photons/cm^2/sec. This value is one order of magnitude smaller than the value derived from the equation (26). Further, the X-ray spectrum in the range of 10keV ~ 1 MeV shows the variable power law index from one observation to the others, but the flux at about 10 keV is relatively stable (Reppin et al. 1979). Then, we assume that the power law index of equation (27) is variable and the spectrum is written as

$$I(E)\sim 4.0\times10^{41}(E/10keV)^{-\alpha}\ photons/sec/eV\ . \quad (28)$$

The plasma near the Cygnus X-3 is heated by the higher energy photons than the temperature of the plasma and is cooled by the lower energy photons. The plasma is also cooled by the thermal bremsstrahlung of the plasma itself. In Appendix B, the energy exchange rate in this plasma is discussed, and the results are used in the following.

If we fix the density of the plasma of about 3×10^{13} cm^{-3} from equation (19), the energy supply rate by pair production (equation (B-10)) and Compton scattering (equation (B-12), within a certain radius of r from the neutron star, is determined by the γ-ray spectrum of equation (28), i.e. by its index, α. When α is small, the energy supply rate is large. On the other hand, the cooling rate (equation (B-15)) by Compton scattering is determined both by the luminosity, L, of the X-rays with energy

lower than the temperature of the plasma and by the temperature of the plasma, kT. The cooling rate by the thermal bremsstrahlung (equation (B-16)) is determined by the temperature of the plasma.

First, we choose the parameters, α and L, so that the heating is relatively small and cooling is large; i.e. α=2.5 and L=2x10^{38} erg/sec. In this case at r<10$^{10\sim11}$cm, Compton cooling and Compton heating are dominant on the energy exchange and they balance each other at the plasma temperature of about 9 keV, as shown in figure 37 (a). Next, we choose the parameters α and L, so as to be an opposite condition; α=2.1 and L=0.5x10^{38} erg/sec. In this case, Compton cooling and heating balance each other at r<10$^{11\sim12}$cm, at the temperature of the plasma of about 100 keV. In this hot region, the plasma is almost fully ionized, so that the effect of bound-free, free-bound and bound-bound transitions is negligible. Therefore, in this hot region, the discussion about the X-ray heating in the previous subsection should be corrected and the temperature is determined as shown above.

After all, in the case of n$\sim$3x10^{13}cm^{-3}, we can expect that the exchange of energy, at r<10$^{10\sim11}$cm, is mainly due to Compton cooling and heating and they balance at the temperature of about several tens keV.

The flux of X-rays and γ-rays decrease in proportion to the square of the distance from the X-ray star, so that the energy exchange rate by Compton scattering decrease as the same. On the other hand, the cooling rate by the thermal bremsstrahlung is proportional to the square of the density of the plasma. In the

region of $r<10^{10\sim11}$ cm, we can roughly assume that the density is constant, so that the cooling rate of the thermal bremsstrahlung is independent of the distance from the X-ray star. Thus, at the more distant region ($r>10^{10\sim11}$cm), the temperature is determined by the energy balance among Compton heating, Compton cooling and the cooling by the thermal bremsstrahlung. Hence, the temperature of the plasma at $r>10^{10\sim11}$cm becomes lower than that of the inner region. When the temperature decreases to several keV, bound-free, free-bound and bound-bound transitions play an important role. Therefore, ionization state is estimated by the parameter ξ, whose value can be obtained from the variable q shown in figure 36. Therefore the discussion for the iron lines emission region in VI-2 is still valid in this region.

④ The observations and the explanations

If we assume that the existence of γ-rays and the enshrouding matter of the density distribution given by equation (19), the hot gas region is naturally derived. In the following, we show that this model can explain almost all the behavior of Cygnus X-3.

The quiescent radio emission is explained by Vestrand (1983) with the model having the same matter distribution and γ-rays as ours. The relativistic electrons and positrons are produced by pair productions of γ-rays with thermal ions, or Compton collisions of γ-rays with thermal electrons. They emit the synchrotron radiations, which are observed as the quiescent radio emission.

The free-free optical depth of infrared ($\nu \sim 10^{14}$ H_z) is given by

$$\tau = \int_r^\infty f_{ff}\, n(r)^2\, dr \sim 5.1\times10^{-4} g Z^2 T_6^{-3/2} \nu_{14}^{-2} r_{11}^{-3} \qquad (29)$$

where f_{ff} is the opacity of the free free transition. $10^6 T_6 = T$, $10^{14}\nu_{14} = \nu$, and g is the mean Gaunt factor, which is of the order of unity. Then, the free-free optical depth is less than unity from the surface of the companion star to infinity. The black body radiation from the surface of the companion star, assuming its temperature of 10^4K and its radius of 3×10^{10} cm, is given as.

$$I_b \sim 1.6\times10^{17} (\exp(h\nu/kT)-1)^{-1} \nu_{14}^3 \text{ erg/sec/Hz} . \qquad (30)$$

The free-free radiation from the optically thin region is,

$$I_f \sim 2.2\times10^{20} g(kT)^{-1/2} \exp(-E/kT)\, r_{11}^{-1} \text{ erg/sec/Hz} . \qquad (31)$$

If we assume the temperature is 10^6K, $\nu \sim 10^{14}$ Hz and the distance

to Cygnus X-3 is 12 kpc, the value derived from equation (31) is comparable with the observed infrared flux. Further, if the enshrouding matter is due to the stellar wind, it is possible that the evaporation of the matter from the surface of the companion star facing the X-rays star is greater than that of the opposite surface, because of the X-ray irradiation. Therefore, the cloud in the hemisphere containing the X-ray star may be denser than that in the another hemisphere. so that the infrared flux reveals a small modulation.

If we assume the radius of the companion star is 3×10^{10} cm and the density distribution given by equation (19), the scattering depth from the surface of the companion star to infinity is about 7. In this scattering depth, we can expect, as shown by Hertz et al.(1978), that the light curve of X-ray reveals nearly sinusoidal. Furthermore, around the phase 0, since we mainly observe the scattered components by the hot gas, the spectrum is expected to be harder than the other phase. In other words, the temperature around phase 0 is higher than that at the other phase, when we fit the spectrum with a black body spectrum.

Figure 38 shows a schematic illustration of our model. We performed a Monte Carlo simulation assuming the density profile of $3\times10^{13}r_{11}^{-2}$, separation of 10^{11} cm, and the hot plasma, whose center is at the X-ray star, having the temperature of 10 keV and radius of 10^{11}cm. The incident X-ray spectrum from the neutron star is a black body spectrum with the temperature of 1 keV. The energy transfer per Compton scattering is roughly given by $E(4kT-E)/mc^2$, where E is the photon energy, kT is the temperature of

electrons and m is the electron rest mass. Thus, in the hot region, the energy transfer per Compton scattering is larger than that in the outer region. Therefore, we neglect the energy transfer of the scattering in the outer region. Figure 39 and 40 show the light curve of the energy of several keV and the PHA ratios, respectively. They resemble the observed results.

The difference between the spectral shape in 1983 and that in 1984 can be explained by the change of the scattering length in the hot plasma as pointed out in V-2. The spectrum in 1984 is similar to that of the low state. Therefore, the spectral variation between the high state and the low state may be considered to be due to the change of the scattering length of the hot region.

The asymmetry in the 4.8-hour X-ray light curve may result from an elliptical binary orbit as suggested by Elsner et al. (1980) and Ghosh et al.(1981).

The EXOSAT data shows that the flux of the iron feature is modulated (van der Klis, 1985). In their data, the flux of the iron feature is stronger than our data by the factor of 2 or 3. This fact is explained as follows. When the enshrouding matter becomes denser, the radius of the hot region becomes smaller, because Compton cooling and heating rate are proportional to the density and the cooling rate by the thermal bremsstrahlung is proportional to the square of it. Then the region emitting iron lines approaches to the X-ray star, so that the flux of the iron lines are modulated. At the same time, the denser matter can emit more intense iron lines.

Our model does not explain the radio outbursts and the

origin of the γ-rays. Gregory et al.(1974) and Petersen et al. (1973) explained the radio giant outburst by the ejection of relativistic particles. Vestrand and Eichler (1982) proposed the model for the γ-rays with $E>10^{12}$ eV, and the implications of the γ-rays with $E>10^{15}$ eV were discussed by Eichler and Vestrand (1983), Hillas (1984) and Porter(1984). They argue that the neutron star, which may be a young pulsar whose period is an order of msec, accelerates relativistic particles by some mechanism. However, these phenomena remain to be highly puzzling. (In our model, even if there is a young pulsar, we can not detect its pulsation because the large scattering length would smear out the pulsations.)

VI-5. Concluding remarks.

We observed the detailed spectra of Cygnus X-3 with the SPC aboard Tenma. The spectra show the strong iron feature around 6.7 keV and the shallow dip, presumably the absorption edge of He-like iron ions, around 9 keV. We found that the iron feature intensity strongly correlates with the mean intensity during the 4.8-hour modulation in the range 9-10 keV. This fact suggests that the emission mechanism of the iron lines is the fluorescence. The iron feature intensity appears to have no modulation at the 4.8-hour period.

The nearly sinusoidal light curve suggests that Cygnus X-3 is enshrouded with the matter with the scattering depth of several. The variation of the spectrum according to the 4.8-hour modulation, which shows the harder spectrum at the phase 0 than the other phases, can not be resembled by the changes of the

absorption column density either of the neutral or of partially ionized gas. This suggests that the enshrouding matter is highly ionized and is a high-temperature gas which is modulated in the 4.8-hour period.

From these facts, we propose a new model for Cygnus X-3 as follows. Cygnus X-3 is a close binary system containing a neutron star and a normal companion star, and the system is enshrouded with matter. The neutron star emits X-rays and γ-rays. The enshrouding matter in the inner region on the orbital size has a high temperature (several tens keV) by the energy supply of mainly the γ-rays.

This model can explain almost all the phenomena of Cygnus X-3, from radio to X-rays wavelength. To recognize the radio outburst and the origin of the γ-rays, we must await further observations of them and theoretical developments.

APPENDIX A. The estimation of the intensity of the iron lines emitted by the fluorescence.

We examine the intensity of the iron lines emitted by the fluorescence, according to Basko (1980). We consider an open uniform gaseous shell located at a radius r and subtending a solid angle Ω as seen from an X-ray source. Under the assumption that all the resonance photons created in the shell ultimately escape, the expression for the intensity, I_{Line}, can be written as

$$I_{Line} = \beta\ n_e n_{Fe} \Omega r^2 \delta \quad \text{(photons/sec)}, \qquad \text{(A-1)}$$

where β is the excitation coefficient, n_e and n_{Fe} are the number density of electron and iron ion, δ is the geometrical thickness of the shell. The iron number density n_{Fe} is represented as

$$n_{Fe} = 4\times10^{-5}\ n_H Y_{Fe} \quad (cm^{-3}), \qquad \text{(A-2)}$$

where Y_{Fe} is the ratio between the iron abundance and the iron cosmic abundance (Allen, 1973). The geometrical thickness of the shell is represented as

$$\delta = \tau_T/(\sigma_T n_e), \qquad \text{(A-3)}$$

where τ_T is Thomson scattering length and σ_T is Thomson cross section. Then we can rewrite equation (A-1) as

$$I_{Line} = 7.2 \times 10^{19}\ \tau_T \Omega Y_{Fe} \beta n_e r^2 \quad \text{(Photons/sec)}. \qquad \text{(A-4)}$$

If the iron is predominantly in the form of He like,

$$\beta \sim \beta^{24} = \alpha_{tot}^{24} \chi^{25} (1- \alpha_1^{24}/\alpha_{tot}^{24}) \quad (sec^{-1}), \qquad \text{(A-5)}$$

$$\alpha_1^{24}/\alpha_{tot}^{24} \sim 18\% \text{ , (Basko,1980)} \qquad \text{(A-6)}$$

where α_1^{24} (α_{tot}^{24}) is the radiative recombination coefficient to the ground state (summed over all states) of Fe XXV, χ^{25} is

the fraction of Fe XXVI, and β^{24} is the excitation coefficient of Fe XXV. In the steady state,

$$\gamma^{24}\chi^{24} = \alpha_{tot}^{24} n_e \chi^{25}, \qquad \text{(A-7)}$$

where γ^{24} is the photoionization rate for Fe XXV which given by

$$\gamma^{24} = (1/(4\pi r^2)) \int_{Eth}^{\infty} \sigma^{24}(\varepsilon) I(\varepsilon)\, d\varepsilon \quad (sec^{-1}). \qquad \text{(A-8)}$$

where $I(\varepsilon)$ is the spectrum of the X-rays, Eth is the threshold energy of K edge and $\sigma^{24}(\varepsilon)$ is the photoelectric cross section of Fe XXV which is given by

$$\sigma^{24}(\varepsilon) = 2 \times 6.3\times10^{-18}/25.7^2 \times (Eth/\varepsilon)^{2.84} \quad (cm^2), \qquad \text{(A-9)}$$

Thus,

$$\gamma^{24} = 0.73\times10^{-18}/r^2 \int_{Eth}^{\infty} I(\varepsilon)/\varepsilon^{2.84}\, d\varepsilon \quad (sec^{-1}). \qquad \text{(A-10)}$$

In the case $\chi^{24} \sim 1$, from the equations (A-5),(A-6),(A-7) and (A-10),

$$\beta \sim \beta^{24} = 0.60\times10^{-18}/(r^2 n_e) \int_{Eth}^{\infty} I(\varepsilon)/\varepsilon^{2.84}\, d\varepsilon \quad (sec^{-1}). \qquad \text{(A-11)}$$

Then, we arrive at a conclusion that the intensity of the iron feature emitted by the plasma limited by the value

$$I_{Line} \sim 30 \int_{Eth}^{\infty} I(\varepsilon)/\varepsilon^{2.84}\, d\varepsilon\ \tau_T \Omega Y_{Fe} \text{ (photons/sec)}. \qquad \text{(A-12)}$$

In the same time, we can estimate the Lyman continuum intensity, changing $(1-\alpha_1^{24}/\alpha_{tot}^{24})$ in the equation (A-5) into $\alpha_1^{24}/\alpha_{tot}^{24}$, and it is

$$I_{Lyman} \sim 6.6 \int_{Eth}^{\infty} I(\varepsilon)/\varepsilon^{2.84}\, d\varepsilon\ \tau_T \Omega Y_{Fe}$$

(photons/sec). (A-13)

APPENDIX B. The energy exchange rate of the matter near the γ-ray emitting neutron star.

As shown in the text, we assume the γ-ray spectrum as

$$I(E) \sim 4.0 \times 10^{41} (E/10keV)^{-\alpha} \text{ photons/sec/eV.} \qquad (B\text{-}1)$$

These γ-rays supply the plasma with energy. The γ-rays with energies $E > 1$ MeV generate pairs of an electron and a positron. The total cross section of a γ-ray for pair production in the energy range ($E >> 2\,mc^2$), is given as (Heitler ,1954),

$$\sigma_p = (1/137)\, r_e^2((28/9)\ln(2E/(mc^2)-(218/27)), \qquad (B\text{-}2)$$

where r_e is the classical electron radius, m is the electron mass and c is the light velocity. The pair production rate in the material of the constant density n, within the radius r from the neutron star, is given by ,

$$\int_{1MeV}^{\infty} 4.0 \times 10^{41} (E/10keV)^{-\alpha}\, nr\, \sigma_p\, dE \quad . \qquad (B\text{-}3)$$

Interaction of the electrons, with the thermal material and magnetic field, causes the ionization, the bremsstrahlung and the synchrotron emission losses.

The synchrotron emission loss, $\dot{E}_s$, of an electron of the energy of E is given by

$$\dot{E}_s = 2.48 \times 10^{-2} (B^2/8\pi)(E/mc^2)^2 \text{ eV/sec} , \qquad (B\text{-}4)$$

where B is the magnetic field strength.

The bremsstrahlung loss, $\dot{E}_b$, for an electron of the energy E in the plasma of density n is

$$\dot{E}_b = 1.4 \times 10^{-16} E\,(\ln(E)+14.38)\, n \text{ eV/sec} . \qquad (B\text{-}5)$$

The ionization loss rate is given as (Gold ,1972),

$$\frac{dEi}{dx} = (4\pi ne^4/(mv^2))\,\Gamma , \qquad (B\text{-}6)$$

$$\Gamma = \ln((\gamma-1)^{1/2}\beta mc^2(2\delta)^{1/2}/\hbar\omega_p) + (1/2)(1+(2\gamma-1)/\gamma^2)\ln(1-\delta) + (1/2)(\delta/(1-\delta)) + (1/4)((\gamma-1)/\gamma)^2\delta ,$$

where $\delta = (\Delta E_{lab})_{max}/((1/2)mv^2)$, $(\Delta E_{lab})_{max}$ is the maximum energy exchange in the lab frame, v is the electron velocity, ω_p is the plasma frequency, e is the electron charge, $\hbar$ is the Planck's constant, $\beta = v/c$ and $\gamma = (1-\beta^2)^{-1/2}$.

If we assume that the mean energy of the electron and the positron is several MeV, plasma density is about 3×10^{13} cm^{-3} from equation (19) and the magnetic field strength is $\sim 10^3$ gauss, which was the value used to explain the quiescent radio from Cygnus X-3 by Vestrand (1983), we obtain

$$\dot{E}_s \sim 4 \times 10^3 \text{ eV/sec} , \qquad \text{(B-7)}$$

$$\dot{E}_b \sim 10^4 \text{ eV/sec} , \qquad \text{(B-8)}$$

$$\frac{dEi}{dx} \sim 7 \times 10^{-5} \text{ eV/cm (i.e. } \dot{E}i \sim 10^6 \text{ eV/sec)} . \qquad \text{(B-9)}$$

For a positron similar calculation can be performed. Therefore, almost all of the energy of the electron and positron is given to the plasma. Each electron and positron produced by a photon of energy E, roughly supplies the plasma in the radius r with the energy whose value is smaller one between E/2 and $(4\pi ne^4/(mv^2))\Gamma r$. Thus the energy supplied by pair production in the radius r from the neutron star is given by

$$\int_{1MeV}^{\infty} 2x4.0x10^{41}(E/10keV)^{-\alpha} nr\sigma_p \; Min((4\pi n_e e^4/(mv^2))\Gamma r, E/2)dE. \qquad \text{(B-10)}$$

Compton scattering by the γ-rays supplies the plasma with energy. The exchanged energy of one collision is $\sim E^2/(mc^2+E)$, and the cross section is given by

$$\sigma_c \sim \sigma_T \qquad (E<10keV) ,$$

$$\sim \sigma_T (1-(5/8)(E-10keV)/(mc^2)) \qquad (10keV<E<mc^2),$$

$$\sim \sigma_T (3/8)(mc^2/E)(\ln(2E/(mc^2))+(1/2)) \quad (mc^2<E). \quad (B-11)$$

The electron scattered by a γ-ray also mainly loses the energy by ionization process. The energy supplied by Compton scattering in the radius r from the neutron star is given by

$$\int_{E_{min}}^{\infty} 4.0\times10^{41}(E/10keV)^{-\alpha} \mathrm{Min}((E^2/(mc^2+E)),((4\pi n_e e^4)/(mv^2))\Gamma r)\sigma_c n r dE \ . \quad (B-12)$$

where, we will set E_{min} equal to the plasma temperature.

Next, we examine the energy loss of the plasma. The plasma is irradiated by the X-rays with lower energies than the plasma temperature. The energy exchange at one collision with the X-ray photons with average energy <E> is

$$(4kT_e/mc^2)\ \langle E\rangle \ , \qquad (B-13)$$

where kT_e is the temperature of the plasma. The rate of collision is given by

$$(L/\langle E\rangle)\ n r \sigma_T \ , \qquad (B-14)$$

where L is the luminosity of the X-rays with $E<kT_e$ in erg. Then the loss rate by Compton scattering is given by

$$Lnr\sigma_T(4kT_e/(mc^2)) \text{ erg/sec} \ ,$$

$$= 6.2 \times 10^{11} Lnr\sigma_T(4kT_e/(mc^2)) \text{ eV/sec} \ . \qquad (B-15)$$

The energy loss rate by the thermal bremsstrahlung is given by

$$(4\pi r^3/3)n^2 g\ 3\times10^{-12}(kT_e)^{1/2} \text{ eV/sec} \ . \qquad (B-16)$$

where g is the mean Gaunt factor, which is of order of unity.

Acknowledgment

I am grateful to Professor S. Miyamoto for his valuable discussion and comments on this work as well as for his continuous encouragement through six years of my career in this field. I thank Professor K. Yamashita and Dr. H. Tsunemi for their useful and stimulating discussions and for critically reading the manuscript. I am thankful to Professor S. Hayakawa in Nagoya university for his valuable coments. I wish to thank Mr. Y. Matsui. He also analyzed the data of Cygnus X-3 and completed his Master dissertation. which was very useful for a guide article of this work.

I thank Professors Y. Tanaka. M. Oda. F. Makino. R. Hoshi. M. Matsuoka. and Y. Ogawara. and Drs. K. Koyama. H. Inoue. T. Murakami. and K. Makishima for their useful discussion at ISAS. All the members of X-ray astronomy group at ISAS developed the important part of the data reduction system for the Tenma satellite. I acknowledge their endeavors.

Finally. I thank Dr. H. S. Hudson and Professor J. E. Grindlay for their careful review of the manuscript and valuable comments.

References

Allen, C. W. 1973, in Astrophysical Quantities, 3d ed, Athlone Press, London.

Arnett, W.D., and Bowers,R.L. 1977, Ap. J. Suppl. 33,254.

Baity, W. A., Ulmer, M. P., Wheaton, W. A., and Peterson, L. E. 1973. Nature, 245, 90.

Basko, M. M., Hatchett, S., McCray, R., and Sunyaev, R.A. 1977, Ap. J. 215, 276.

Basko, M. M., Sunyaev, R. A., and Titarchuk, L. G. 1974, Astron. Astrophys. 31, 249.

Basko, M. M. 1980, Astron. Astrophys. 87, 330.

Becker, R. H., Robinson-Saba, J. L., Boldt, E. A., Holt, S. S., Pravdo, S. H., Serlemitsos, P. T., and Swank, J. H. 1978, Ap. J. Lett. 224, L113.

Becklin, E. E., Kristioan, J., Neugebauer, G., and Wynn-Williams, C. G. 1972, Nature.239, 130.

Becklin, E. E., Neugebauer, G., Hawkins, F. J., Mason, K. O., Sanford, P. W., Matthews, K., and Wynn-Williams, C. G. 1973, Nature 245, 302.

Becklin, E. E., Hawkins, F.J., Mason, K.O., Mathews, K., Neugebauer, G., Packman, D., Sanford, P. W., Schupler, B., Stark, A., and Wynn-Williams, C. G. 1974, Ap. J. Lett. 192, L119.

Bennett, K., Bignami, G., Hermsen, W., Mayer-Hasselwander, H. A., Paul, J. A., and Scarsi, L. 1977, Astron. Astrophys. 59, 273.

Bethe, H. A., Salpeter, E. E. 1957, Quantum Mechanics of One and two-Electron Systems, Academic Press, New York.

Blissett, R. H., Mason, K. O., and Culhane, J. L. 1981, MNRAS, 194, 77.

Bonnet-Bidaud, J. M., and van der Klis, M. 1981, Astron. Astrophys. 101, 299.

Bradt, H. V. D., and McClintock, J. E. 1983, Ann Rev. Astron. Astrophys. 21, 13.

Brown, B. L., and Gould, R. J. 1970, Phys. Review. D. 1, 2252.

Chu, K. W., and Bieging, J. H. 1973, Ap. J. Lett. 179, L21.

Danaher, S., Fegan, D. J., Porter, N. A., and Weeles, T. C. 1981, Nature, 289, 568.

Davidsen, A., and Ostriker, J. P. 1974, Ap. J. 189, 331.

Dickey, J. M. 1983, Ap. J. Lett. 273, L71.

Dowthwaite, J. C., Gibson, A. I., Harrison, A. B., Kirkman, I, W., Lotts, A. P., Macrare, J. H., Orford, K. J., Turver, K. E., and Walmsley, M. 1983, Astron. Astrophys. 126, 1.

Eichler, D., and Vestrand, W. T. 1984, Nature 307, 613.

Elsner, R. F., Ghosh, P., Darbro, W., Weisskopf, M. C., Sutherland, P. G., and Grindlay, J. E. 1980, Ap. J. 239, 335.

Forman, W., Jones, C., Cominsky, L., Julian, P., Murray, S., Peters, G., Tananbaum, H., and Giacconi, R. 1978, Ap. J. Supple. 38, 357.

Geldzahler, B. J., Kellermann, K. T., and Shaffer, D. B. 1979, Astron. J. 84, 186.

Geldzahler, B. J., Johnston, K.J., Spencer, J. H., Klepczynski, W. J., Josties, F. J., Angerhofer, P. E., Florkowski, D. R., McCarthy, D. D., Matsakis, D. N., and Hjellming, R. M. 1983,

Ap. J. Lett. 273, L65.
Ghosh, P., Elsner, R. F., Weisskopf, M. C., and Sutherland, P. G. 1981, Ap. J. 251, 230.
Giacconi, R., Gursky, H., Paolini, F. P., and Rossi, B. B. 1962, Phys. Rev. Let. 9 439.
Giacconi, R., Gorenstein, P., Gursky, H., and Waters, J. R. 1967, Ap. J, Lett. 148. L119.
Gould, R. J. 1972, Physica 60, 145.
Gregory, P. C., Kromberg, P. P., Seaquist, E. R., Hughes, V. A., Woodsworth, A., Viner, M. R., Retallact, D., Hjellming, R. M., and Balick, B. 1972, Nature 239, 114.
Harnden, F. R., Branduardi, Jr. G., Elvis, M., Gorenstein, P., Grindlay, J., Pye, J. R., Rosner, R., Topka, K., and Vaianna, G. S. 1979, Ap. J. Lett. 234, L51.
Hatchett, S., and McCray, R. 1977, Ap. J. 211, 552.
Hayakawa, S., Hirano, T., Kunieda, H., and Nagase, F. 1984, Adv. Space Res. 3, No.10-12, 67.
Heitler, W. 1954, in The Quantum Theory of Radiation (London, Oxford Press).
Hermsen, W. 1984, in Contribution to the Proceedings of the 18th ESLAB Symposium 'X-ray Astronomy: 5-9 November 1984, Scheveningen', The Hague, the Netherlands.
Hertz, P., Joss, P. C., and Rappaport, S. 1978, Ap. J..224, 614.
Hillas, M. 1984, Nature, 312, 50.
Hirano, T., Hayakawa, S., Kunieda, H., Makino, F., Masai, K., Nagase, F., and Yamashita, K. 1984, Publ. Astron. Soc. Japan 36, in press.
Hjellming, R. M. 1973, Science, 182, 1089.
Hjellming, R. M., Brown, R. L., and Blankenship, L. C. 1974, Ap. J. Lett. 184, L19.
Holt, S. S., Kaluzienski, L. J., Boldt, E. A., and Serlemitsos, P. J. 1979, Ap. J. 233, 344.
Inoue, H., Koyama, K., Matsuoka, M., Ohashi, T., Tanaka, Y., Waki, I. 1982, Nuclear Instrumensts and methods, 196, 69.
Joss, P. C. 1978, Ap. J. Lett. 225, L123.
Kallman, T. R., and McCray, R. 1982, Ap. J. Supple, 50, 263.
Kestenbaum, H. L., Long, K. S., Novick, R., Weisskopf, M. C., and Wolff, R. S. 1977, Ap. J. Lett. 216, L19.
Kestenbaum, H. L., Ku, W. H.-M., Long, K. S., Silver, E. H., and Novick, R. 1978, Ap. J. 226, 282.
Koyama, K., Ikegami, T., Inoue, H., Kawai, N., Makishima, k., Matsuoka, M., Mitsuda, K., Murakami, T., Ogawara, Y., Ohashi, T., Suzuki, K., Tanaka, Y., Waki, I., and Fenimore, E. E. 1984, Publ. Astron. Soc. Japan, 36, 659.
Lamb, R. C., Godfey, C. P., Wheaton, W. A., and Trumper, T. 1982, Nature, 296, 543.
Lamb, R. C., Fichtel, C. E., Hartmann, R.C., Kniffen, D. A., and Thompson, D. J. 1977, Ap. J. Lett. 212, L63.
Lamb, R. C., Dower, R. G. D., and Fickle, R. K. 1979, Ap. J. Lett. 227, L19.
Lampton, M., Margon, B., and Bowyer, S. 1976, Ap. J. 208, 177.
Lauque, R., Lequeux, J. H., Rieu, N. Q. 1972, Nature 239, 119.
Leach, R. W., Murray, S. S., Schreier, E. J., Tananbaum, H. D., Ulmer, M. D., and Parsignault, D. R., 1975, Ap. J. 199, 184.
Lloyed-Evans, J., Coy, R. N., Lambert, A., Lapikens, J., Patel, M., Reid, R. J. O., and Watson, A. A. 1983, Nature, 305, 27.

Manzo, G., Molteni, D., and Robba, N. R. 1978, Astron and Astrophys. 70, 317.
Mason, K. O., Becklin, E. E., Blankenship, L., Brown, R. L., Elias, J., Hjellming, R. M., Matthews, K., Murdin, P. G., Neugebauer, G., Sanford, P. W., Willner, S. P. 1976, Ap. J. 207, 78.
Mason, K. O., and Sanford, P. W. 1979, MNRAS.189, 9.
Matteson, J. L. 1971, Ph.D. Thesis. University of California, San Diego.
Maxon, M. S., and Corman, E. G. 1967, Phys. Rev. 163, 156.
Meegan, C. A., Fishman, G. T., and Haymes, R. C. 1979. Ap, J. Lett. 234, L123.
Milgrom, M. 1976, Astron. Astrophys. 51, 215.
Milgrom, M., and Pines, D. 1978, Ap. J. 220, 272.
Mitsuda, K., Inoue, H., Koyama, K., Makishima, K., Matsuoka, M., Ogawara, Y., Shibazaki, N., Suzuki, K., Tanaka, Y., and Hirano, T. 1984. Publ. Astron. Soc. Japan 36. in press.
Molteni, D., Rapisarda, M., Robba, N. R., and Scarsi, L. 1980. Astron. Astrophys. 87, 88.
Nagase, F., Hayakawa, S., Kii, T., Sato, N., Ikegami, T., Kawai, N., Makishima, K., Matsuoka, M., Mitani, K., Murakami, T., Oda, M., Ohashi, T., Tanaka, Y., and kitamoto, S. 1984, Publi. Astron. Soc. Japan, 36. in press.
Neshpor, YU. I., Stepanian, A. A., Fomin, V. P., Gerosimov, S. A., Vladimirsky, B. M., and Ziskin, YU. L. 1979, Astrophys. Space. Sci. 61, 349.
Ohashi, T., Inoue, H., Koyama, K., Makishima, K., Matsuoka, M., Murakami, T., Oda, M., Ogawara, Y., Shibazaki, N., Tanaka, Y., Hayakawa, S., Kunieda, H., Makino, F., Masai, K., Nagase, F., Tawara, Y., Miyamoto, S., Tsunemi, H., and Yamashita, K. 1982, Ap. J. 258. 254.
Paczynski, B. 1971, Ann. Rev. Astron. Astrophys. 9, 183.
Parsignault, D. R., Gursky, H., Kelligg, E. M., Matilsky, T., Murray, S., Schreier, E., Tananbaum, H. Giacconi, R., and Brinkman, A. C. 1972, Nature 239, 143.
Parsignault, D. R., Schreier, E., Grindlay, J., and Gursky, H. 1976, Ap. J. Lett. 209, L73.
Parsignault, D. R., Grindlay, J., Gursky, H., and Tucker, W. 1977, Ap. J. 218, 232.
Peterson, F. W. 1973, Ap. J. 271, 304.
Porter, N. A. 1984, Nature 312, 347.
Pravdo, S. H. 1979, in X-ray Astronomy, ed. W. A. Baity and L.E. Pwterson, Cosper Advances in Space Exploration, Volume 3, Pergaman press, Oxford.
Pringle, J. E. 1975, MNRAS. 170, 633.
Pringle, J. E. 1974, Nature, 247, 21.
Protherore, R. J., and Gerhardy, P. R., 1984, Ap. J., Lett. 280, L47.
Rappaport, S., Joss,P. 1981, in X-ray Astronomy with the Einstein Satellite, ed. R. Giacconi, p123. D. Reidel Publishing Company, Dordrecht.
Reppin, C., Pietsch, W., Trumper, J., Voges, W., Kendziorra, E., and Staubert. R. 1979, Ap. J. 234, 329.
Robinson, E. L. 1976, Ap. J. 203, 485.
Sanford, P. W., Hawkins, F. H. 1972, Nature 239,335.
Sanford, P., Mason, K. O., and John, I. 1975, MNRAS 173, 9.

Samorski, M., and Stamm, W. 1983, Ap. J. Lett. 268, L17
Seaquist, E. R., and Gregory, P. C. 1977, Astrophys. Lett. 18, 65.
Serlemitsos, P. J., Boldt, E. A., Holt, S. S., Rothschild, R. E., and Saba, J. L. R. 1975, Ap. J. 201, L9.
Tanaka, Y., Fujii, M., Inoue, H., Kawai, N., Koyama, K., Maejima, Y., Makino, F., Makishima, K., Matsuoka, M., Mitsuda, K., Murakami, T., Nishimura, J., Oda, M., Ogawara, Y., Ohashi, T., Shibazaki, N., Suzuki, K., Waki, I., Yamagami, T., Kondo, I., Murakami, H., Hayakawa, S., Hirano, T., Kunieda, H., Masai, K., Nagase, F., Sato, N., Tawara, Y., Kitamoto, S., Miyamoto, S., Tsunemi, H., Yamashita, K., and Nakagawa, M. 1984. Publ. Astron. Soc. Japan, 36, 641.
Tarter, C. B., Tucker, W. H., and Salpeter, E. E., 1969, Ap. J., 156, 943.
Tucker, W. H. and Gould, R. T., 1966, Ap. J., 144, 244.
Ulmer, M. P., Baity, W. A., Wheaton, W. A., and Peterson, L. E. 1974. Ap. J. 192, 691.
van den Heuvel, E. P. J., and de Loore, C. 1973. Astron. Astrophys. 25, 387.
van der Klis, M., and Bonnet-Bidaud, J. M. 1981, Astron. Astrophys. 95, L5.
van der Klis, M., and Bonnet-Bidaud, J. M. 1982. Astron, Astropys. Suppl. 50, 129.
van der Klis, M., and Jansen, F. 1984, preprint.
van der Klis, M. 1985. Talk presented at Japan U.S. Seminar, Tokyo.
van Paradijs, J. 1978, Nature 274, 650.
Vestrand, W. T. 1983, Ap. J. 271, 304.
Vestrand, W. T., and Eichler, D. 1982. Ap. J. 261, 251.
Weekes, T. C. 1983, Astron. Astrophys. 121, 232.
Westphal, J. A., Kristain, J., Huchra, J. P., Shectman, S. A., and Brucato, R. J. 1972. Nature 239, 134.
White, N. E., and Holt, S. S. 1982. Ap. J. 257, 318.
Wood, K. S., Meekins, J. F., Yentis, D. J., Smathers, H. W., McNutt, D. P., Bleach, R. D., Byram, E. T., Chubb, T. A., Friedman, H., abd meidav, M. 1984, Ap. J. Supple. in press.
Woodsworth, A. W. 1983, Astron. Astrophys. 122, 322.

Table - 1.

Experiments on-board TENMA

Experiment	No. of Modules	Effective Area at Peak Efficiency (cm^2)	Effective Energy Range (keV)	Field of View (FWHM)	Note
SPC A	4	80.x 4	2 – 60	3.1°	Array of GSPC's
SPC B	4	80 x 4		2.5°	
SPC C *	2	40 x 2 ** (Fig. 4)		3.8°	*Equipped with Modulation Collimators (34' and 43' pitches, respectively) **Peak Transmission
XFC	2	7 x 2 (Fig.10)	0.1 – 2.	1.4° x 5°	One-dim. Mirror & Multiwire PC (resolution ~0.2°)
TSM HXT	2	27 x 2 * (Fig.12b)	2 – 25	40° x 40° (FW)	One-dim. Hadamard Mask (resolution ~1°) *Peak Transmission
TSM ZYT	2	88 x 2	1.5–25	2° x 25°	Crossed Collimators (resolution ~1°x2°)
RBM/GBD	2	7 x 2	10 – 100	1 sterad.	NaI(Tl) Scintillation Counter

SPC : Scintillation Proportional Counters
XFC : X-Ray Focusing Collector
TSM : Transient Source Monitor
RBM/GBD : Radiation Belt Monitor/ Gamma-Ray Burst Detector

Table - 2.

Time resolutions of the SPC system

Group	Bit rate	PH mode		MPC Mode			
		256 ch (ms)	1 ch * (ms)	128 ch (s)	C128 ch (s)	32 ch (s)	C32 ch (s)
SPC-A	H	15.625	62.5	2	0.5	0.5	0.125
	L	62.5	250	8	2	2	0.5
SPC-B	H	15.625	62.5	2	0.5	0.5	0.125
	L	62.5	250	8	2	2	0.5
SPC-C	H	15.625	62.5	2	-	0.5	-
	L	62.5	250	8	-	2	-

* Time resolution of an 8-bit scaler for each counter for dead time correction (no energy resolution).

Table - 3.

Name	Flux (error)# 0.5-25 keV (Counts/sec/cm^2	Flux (error)* 2-6 keV (Counts/sec/cm^2)	Coments
1H2105+460 (4U2048+44)	0.0105(0.0007)	0.0043(0.0006)	
1H2018+366 (4U2019+39?).....	0.0080(0.0007)	0.0041(0.0005)	
1H2041+352	0.0011(0.0005)		
1H2050+310 (4U2046+31)	0.1873(0.0021)	0.0020(0.0005)	Cygnus Loop

Wood et al. (1984)
* Forman et al. (1978)

Table - 4.

Parameters of best fit curve $A_0 \exp(-(t-t_0)/\tau_1) + A_1 \exp(-(t-t_0)/\tau_2) \sin(2\pi((t-t_0)/P-\Delta))$ for observation of Cygnus X-3. 1983. Sept. 13-18.

Period (sec)	A_0 (1-9 keV) counts/sec	A_1 (1-9 keV) counts/sec	τ_1 sec	τ_2 sec	Δ cycle
17253.086	541 ± 8	278 ± 14	937000 ± 52000	513000 ± 56000	0.317 ± 0.008
17253.216	541 ± 8	278 ± 14	938000 ± 53000	513000 ± 56000	0.317 ± 0.008

t_0 = 0h 0m. 13. Sept. 1983 (UT)
Quated errors are 68% confidence level($\chi^2_{min}+5.9$). according to Lampton et al. (1976).

Table - 5.
Summary of Observations used to determine a ephemeris.

Tmin (JD 2440000+)	Reference	Energy Bandwidth of Detector (keV)	Phase Min.# (cycle)	Corections$ (cycle)	Error in Phase (cycle)
949.9201	Leach et al.(1975)	2-10	0.0	+0.0200	0.081
987.6624	Leach et al.(1975)	2-10	189.0	+0.0741	0.019
988.4555	Leach et al.(1975)	2-10	193.0	+0.0521	0.032
991.6625	Leach et al.(1975)	2-10	209.0	+0.0541	0.046
1022.9995	Leach et al.(1975)	2-10	366.0	+0.0225	0.070
1024.7890	Leach et al.(1975)	2-10	375.0	+0.0516	0.029
1025.7805	Leach et al.(1975)	2-10	380.0	+0.0506	0.074
1031.1685	Leach et al.(1975)	2-10	407.0	-0.0366	0.079
1107.6697	Leach et al.(1975)	2-10	790.0	+0.0841	0.056
1304.3573	Leach et al.(1975)	2-10	1775.0	+0.0511	0.047
1450.1143	Leach et al.(1975)	2-10	2505.0	+0.0571	0.025
1568.319	Mason and Sanford(1979)	3-8	3097.0	+0.0000	0.010
1579.897	Mason and Sanford(1979)	3-8	3155.0	+0.0000	0.010
1589.679	Mason and Sanford(1979)	3-8	3204.0	+0.0000	0.010
1608.851	Mason and Sanford(1979)	3-8	3300.0	+0.0000	0.010
1697.1296	Leach et al.(1979)	2-10	3742.0	+0.0486	0.030
1818.123	Mason and Sanford(1979)	3-8	4348.0	+0.0000	0.010
1906.781	Mason and Sanford(1979)	3-8	4792.0	+0.0000	0.015
1907.384	Mason and Sanford(1979)	3-8	4795.0	+0.0000	0.010
1929.145	Mason and Sanford(1979)	3-8	4904.0	+0.0000	0.010
1929.545	Mason and Sanford(1979)	3-8	4906.0	+0.0000	0.010
1930.150	Mason and Sanford(1979)	3-8	4909.0	+0.0000	0.015
2187.344	Mason and Sanford(1979)	3-8	6197.0	+0.0000	0.010
2307.747	Mason and Sanford(1979)	3-8	6800.0	+0.0000	0.010
2309.546	Mason and Sanford(1979)	3-8	6809.0	+0.0000	0.010
2311.740	Mason and Sanford(1979)	3-8	6820.0	+0.0000	0.010
2313.738	Mason and Sanford(1979)	3-8	6830.0	+0.0000	0.010
2314.135	Mason and Sanford(1979)	3-8	6832.0	+0.0000	0.015
2314.740	Mason and Sanford(1979)	3-8	6835.0	+0.0000	0.010
2315.132	Mason and Sanford(1979)	3-8	6837.0	+0.0000	0.010
2315.731	Mason and Sanford(1979)	3-8	6840.0	+0.0000	0.010
2316.133	Mason and Sanford(1979)	3-8	6842.0	+0.0000	0.015
2316.938	Mason and Sanford(1979)	3-8	6846.0	+0.0000	0.010
2317.731	Mason and Sanford(1979)	3-8	6850.0	+0.0000	0.010
2318.129	Mason and Sanford(1979)	3-8	6852.0	+0.0000	0.010
2318.733	Mason and Sanfodr(1979)	3-8	6855.0	+0.0000	0.015
2371.4484	Parsignault et al.(1976)	1.4-7.2	7119.0	+0.0150	0.013
2552.3637	Parsignault et al.(1976)	1.4-7.2	8025.0	+0.0150	0.025
2660.594	Mason and Sanford(1979)	3-8	8567.0	+0.0000	0.010
2661.588	Mason and Sanford(1979)	3-8	8572.0	+0.0000	0.010
2665.584	Mason and Sanford(1979)	3-8	8592.0	+0.0000	0.010
2666.584	Mason and Sanford(1979)	3-8	8597.0	+0.0000	0.010
2737.8773	Parsignault et al.(1976)	1.4-7.2	8954.0	+0.0150	0.050
2959.718	Mason and Sanford(1979)	3-8	10065.0	+0.0000	0.010
2960.719	Mason and Sanford(1979)	3-8	10070.0	+0.0000	0.010
2961.715	Mason and Sanford(1979)	3-8	10075.0	+0.0000	0.010
2966.198	Mason and Sanford(1979)	3-8	10097.0	+0.0000	0.010
3303.1806	Manzo et al.(1978)	2-12	11785.0	+0.0000	0.0060
3374.667	Mason and Sanford(19799	3-8	12143.0	+0.0000	0.010
3375.660	Mason and Sanford(1979)	3-8	12148.0	+0.0000	0.015
3376.667	Mason and Sanford(1979)	3-8	12153.0	+0.0000	0.020
3377.064	Mason and Sanford(1979)	3-8	12155.0	+0.0000	0.015
3377.663	Mason and Sanford(1979)	3-8	12158.0	+0.0000	0.020
3378.657	Mason and Sanford(1979)	3-8	12163.0	+0.0000	0.020
3517.6420	Lamb et al.(1979)	1.5-6	12859.0	+0.0045	0.017
3538.8090	Lamb et al.(1979)	1.5-6	12965.0	+0.0000	0.045
3823.361	Mason and Sanford(1979)	3-8	14390.0	+0.0000	0.010
3823.957	Mason and Sanford(1979)	3-8	14393.0	+0.0000	0.020
3858.7063	Elsner et al.(1980)	1.1-22	14567.0	+0.0000	0.0054
4377.4907	van der Klis et al.(1981)	2-12	17165.0	+0.0000	0.0035
5590.3923	This work	1-9	23239.0	+0.0000	0.008

The cycle number from the first data (Leach et al. 1975) at JD 2440949.9201
$ To be added to the previous column to produce the corrected phase.
These corrections were obtained from Elsner et al. (1980).

Table -26.
Trial model and χ^2 values

Trial model	13-15, Sept. 1983				16-18, Sept. 1983				11-14, Sept. 1984			
	1#	2	3	4	1	2	3	4	1	2	3	4
B.B.	368.¥ (30)	282. (30)	889. (30)	483. (30)	1407. (30)	934. (30)	905. (30)	1049. (30)	794. (30)	1116. (30)	1187. (30)	950. (30)
T.B.	1283. (30)	2235. (30)	1827. (30)	1330. (30)	3065. (30)	2183. (30)	1774. (30)	2140. (30)	160. (30)	215. (30)	212. (30)	129. (30)
P.L.	3518. (30)	7272. (30)	6304. (30)	4452. (30)	7567. (30)	6056. (30)	6099. (30)	6841. (30)	224. (30)	323. (30)	413. (30)	192. (30)
B.B.+P.L.	183. (28)	320. (28)	213. (28)	386. (28)	139. (28)	290. (28)	421. (28)	309. (28)	33. (28)	55. (28)	57. (28)	67. (28)
B.B.+T.B.	325. (28)	1236. (28)	851. (28)	451. (28)	1170. (28)	750. (28)	836. (28)	992. (28)	162. (28)	259. (28)	54. (28)	132. (28)
P.L.+T.B.	1189. (28)	300. (28)	1781. (28)	993. (28)	414. (28)	2424. (28)	1395. (28)	1715. (28)	168. (28)	218. (28)	217. (28)	104. (28)
B.B.+P.L.+T.B. ...	69. (26)	66. (26)	61. (26)	79. (26)	134. (26)	98. (26)	54. (26)	73. (26)	28. (26)	26. (26)	31. (26)	24. (26)

Phase interval of (1) 0.875-0.125, (2) 0.125-0.375, (3) 0.375-0.625, and (4) 0.625-0.875.
¥ χ^2 values and degree of freedum (parentheses).

Table - 7.

Best fit parameters of three components model.

Time	Phase	Black body Radius(km)#	Black body kT(keV)	Power law log(A#)	Power law index	Thermal bremsstrahlung log(n^2V#)	Thermal bremsstrahlung kT(keV)	column density Log(N_H)	reduced χ^2 D.O.F=26
13-15. Sept.1983	0.875-0.125	$22.5(^{22.9}_{21.6})$	$1.152(^{1.167}_{1.137})$	$45.9(^{46.5}_{45.7})$	$2.3(^{2.9}_{1.7})$	$62.5(^{62.9}_{62.4})$	$0.54(^{0.60}_{0.48})$	$22.99(^{23.03}_{22.95})$	2.67
	0.125-0.375	$35.8(^{36.9}_{33.9})$	$1.100(^{1.115}_{1.085})$	$46.2(^{46.5}_{45.9})$	$2.6(^{2.7}_{2.5})$	$63.1(^{63.1}_{62.7})$	$0.45(^{0.49}_{0.41})$	$23.00(^{23.03}_{22.97})$	2.53
	0.375-0.625	$38.7(^{38.9}_{37.5})$	$1.105(^{1.016}_{1.094})$	$46.7(^{47.1}_{45.1})$	$2.7(^{3.0}_{2.4})$	$62.9(^{63.1}_{62.7})$	$0.49(^{0.53}_{0.45})$	$23.00(^{23.03}_{22.96})$	2.36
	0.625-0.875	$33.3(^{33.4}_{32.4})$	$1.121(^{1.131}_{1.111})$	$46.5(^{47.1}_{46.4})$	$2.6(^{3.0}_{2.2})$	$62.4(^{62.7}_{62.4})$	$0.55(^{0.62}_{0.48})$	$22.94(^{22.99}_{22.89})$	3.03
16-18. Sept.1983	0.875-0.125	$23.7(^{23.8}_{22.9})$	$1.1537^{1.149}_{1.125})$	$46.0(^{46.3}_{45.8})$	$2.3(^{2.6}_{2.0})$	$63.5(^{63.8}_{63.5})$	$0.38(^{0.40}_{0.36})$	$23.06(^{23.09}_{23.04})$	5.15
	0.125-0.375	$32.1(^{32.8}_{30.6})$	$1.102(^{1.117}_{1.087})$	$46.5(^{47.1}_{46.1})$	$2.7(^{3.1}_{2.3})$	$63.6(^{64.0}_{63.4})$	$0.38(^{0.40}_{0.36})$	$23.07(^{23.11}_{23.04})$	3.78
	0.375-0.625	$34.8(^{36.3}_{32.4})$	$1.101(^{1.113}_{1.089})$	$47.7(^{47.9}_{47.4})$	$3.6(^{3.8}_{3.4})$	$64.4(^{65.0}_{63.0})$	$0.32(^{0.42}_{0.22})$	$23.11(^{23.17}_{23.05})$	2.09
	0.625-0.875	$31.5(^{32.1}_{30.1})$	$1.115(^{1.124}_{1.106})$	$46.7(^{46.8}_{46.1})$	$2.9(^{3.4}_{2.4})$	$63.3(^{63.4}_{63.0})$	$0.45(^{0.49}_{0.41})$	$23.03(^{23.07}_{22.99})$	2.82
11-14. Sept.1984	0.875-0.125	$17.1(^{20.1}_{12.8})$	$1.093(^{1.165}_{1.021})$	$46.7(^{47.0}_{46.3})$	$2.2(^{2.6}_{1.8})$	$63.7(^{64.7}_{63.2})$	$0.38(^{0.46}_{0.30})$	$23.11(^{23.19}_{23.03})$	1.08
	0.125-0.375	$22.2(^{24.4}_{19.0})$	$1.136(^{1.097}_{1.175})$	$46.6(^{47.2}_{46.5})$	$2.3(^{2.6}_{2.0})$	$63.0(^{64.3}_{62.9})$	$0.47(^{0.53}_{0.41})$	$23.02(^{23.09}_{22.94})$	0.99
	0.375-0.625	$20.8(^{22.7}_{18.2})$	$1.199(^{1.238}_{1.160})$	$46.8(^{47.5}_{46.3})$	$2.2(^{2.4}_{2.0})$	$62.9(^{64.0}_{62.6})$	$0.48(^{0.63}_{0.33})$	$23.02(^{23.10}_{22.94})$	1.18
	0.625-0.875	$18.1(^{19.5}_{16.1})$	$1.239(^{1.275}_{1.203})$	$46.0(^{46.4}_{45.9})$	$1.7(^{2.1}_{1.3})$	$61.9(^{62.9}_{61.5})$	$0.63(^{0.86}_{0.40})$	$22.97(^{23.05}_{22.88})$	0.91

Distance to Cygnus X-3 is assumed to be 12 kpc.
Quoted errors are 90% confidence level.

Table - 8.

Best fit parameters of the black body spectrum and χ^2 values.

Time	Phase	Radius(km)#	kT(keV)	N_H	reduced χ^2 (D.O.F=21)
13-15, Sept,1983	0.875-0.125	17.6 ± 0.2	1.256 ± 0.008	22.627 ± 0.011	7.66
	0.125-0.375	28.5 ± 0.3	1.197 ± 0.005	22.727 ± 0.007	11.84
	0.375-0.625	31.7 ± 0.4	1.190 ± 0.005	22.733 ± 0.007	7.60
	0.625-0.875	28.3 ± 0.4	1.195 ± 0.006	22.695 ± 0.008	5.54
16-18, Sept,1983	0.875-0.125	17.1 ± 0.2	1.270 ± 0.006	22.753 ± 0.007	32.75
	0.125-0.375	24.8 ± 0.3	1.207 ± 0.006	22.821 ± 0.007	21.82
	0.375-0.625	29.8 ± 0.4	1.184 ± 0.006	22.802 ± 0.007	11.06
	0.625-0.875	25.4 ± 0.3	1.200 ± 0.005	22.772 ± 0.007	13.86
11-14, Sept,1983	0.875-0.125	11.8 ± 0.4	1.500 ± 0.024	22.497 ± 0.034	1.92
	0.125-0.375	16.8 ± 0.4	1.427 ± 0.018	22.536 ± 0.024	1.28
	0.375-0.625	17.3 ± 0.4	1.437 ± 0.016	22.538 ± 0.021	1.63
	0.625-0.875	16.9 ± 0.4	1.450 ± 0.016	22.562 ± 0.020	1.45

Distance to Cygnus X-3 is assumed to be 12 kpc.
Quoted errors are 90% confidence level.

Table - 9.

The properties of iron features.

Time	Phase	Flux counts/sec/cm^2	Energy keV	Width(FWHM) keV	Equivalent Width eV
13-15. Sept. 1983	0.875-0.125	0.0144 ± 0.0009	6.68 ± 0.02	0.42 ± 0.09	310. ± 19.
	0.125-0.375	0.0170 ± 0.0016	6.69 ± 0.04	0.67 ± 0.11	187. ± 18.
	0.375-0.625	0.0159 ± 0.0017	6.73 ± 0.03	0.45 ± 0.14	183. ± 16.
	0.625-0.875	0.0189 ± 0.0016	6.71 ± 0.03	0.45 ± 0.11	212. ± 17.
16-18. Sept. 1983	0.875-0.125	0.0139 ± 0.0008	6.66 ± 0.02	0.61 ± 0.07	304. ± 18.
	0.125-0.375	0.0138 ± 0.0015	6.66 ± 0.04	0.78 ± 0.13	194. ± 21.
	0.375-0.625	0.0128 ± 0.0017	6.74 ± 0.04	0.55 ± 0.16	138. ± 18.
	0.625-0.875	0.0128 ± 0.0011	6.74 ± 0.03	0.42 ± 0.12	175. ± 15.
11-14. Sept. 1984	0.875-0.125	0.0250 ± 0.0023	6.68 ± 0.03	0.68 ± 0.12	502. ± 46.
	0.125-0.375	0.0261 ± 0.0033	6.59 ± 0.05	0.81 ± 0.16	333. ± 42.
	0.375-0.625	0.0300 ± 0.0028	6.68 ± 0.04	0.68 ± 0.12	341. ± 32.
	0.625-0.875	0.0236 ± 0.0022	6.72 ± 0.03	0.40 ± 0.13	373. ± 35.

Quoted errors are 90% confidence level.

Figure Captions

Figure 1. A composite spectrum of Cygnus X-3 from radio to γ-rays.

Figure 2. The schematic structure of Tenma.

Figure 3. The fields of view of three high energy astrophysical experiments on board Tenma.

Figure 4. The schematic illustration of the SPC on board Tenma.

Figure 5. The effective area and the energy resolution (FWHM) of the SPC as a function of energy.

Figure 6. The theoretical pulse height distributions for several monochromatic incident radiation. The each curve was normalized to the total area of one.

Figure 7. The collimator response functions for SPC A. B and C.

Figure 8. The locus of the spin axis in the sky during the observation in 1983. The light solid line and the dashed line are the loci during the attitude maneuver and the natural drift. respectively. The heavy solid line is the locus during the observation.

Figure 9. Same as figure 8 for the observation in 1984.

Figure 10. Same as figure 8 for the observation of the background in 1983.

Figure 11. Same as figure 8 for the observation of the background in 1984.

Figure 12. The observed times of the selected data. The phase is derived from the ephemeris determined in V-1. The phase 0 means the X-ray minimum phase.

Figure 13. The light curve after background subtraction and correction for the satellite attitude in the range 1-3 keV.

3-6 keV. 6-9 keV and 9-21 keV for (a) 1983 observation and (b) 1984 observation. The intervals (a). (b). (c). (d) and (e) indicate the data intervals for the analysis of iron line properties.

Figure 14. The light curve in the range 1-9 keV and the best fit sinusoidal curve including the decrease in the mean level and in the amplitude of the modulation. for the period of 17253.216 sec. The error bars are σ_{rms} (51.437 counts/sec). The horizontal axis is the time (sec) from 0h 0m. Sept. 13. 1983.

Figure 15. The residuals from the linear fit of the data summarized in table 5 except for the Copernicus data.

Figure 16. The residuals from the quadratic fit of the data summarized in table 5 except for the Copernicus data.

Figure 17. The folded light curves in the range 3-6 keV and 6-9 keV and the hardness ratio (intensity in 6-9 keV/ intensity in 3-6 keV) for (a) 1983 observation and (b) 1984 observation.

Figure 18. The spectra of Cygnus X-3 after background subtraction and aspect correction. All the data were divided into three parts. the first half (before 0h 0m Sept. 16 UT). the latter half (after 0h 0m Sept. 16 UT) in 1983 and in 1984, and then integrated for phase intervals. 0.875-0.125. 0.125-0.375. 0.375-0.625 and 0.625-0.875 over each of three parts. (a)-(d) are the spectra of four phase intervals of the first half in 1983. (e)-(h) and (i)-(l) are that of the latter half in 1983 and in 1984. respectively.

Figure 19. The PHA ratios of the spectra in the phase intervals

0.875-0.125, 0.125-0.375 and 0.625-0.875 to it in the phase interval 0.375-0.625, in the first half in 1983.

Figure 20. Same as figure 19 in the latter half in 1983.

Figure 21. Same as figure 19 in 1984.

Figure 22. The PHA ratios between the data in the first half and the latter half of 1983, for each phase interval.

Figure 23. The PHA ratios between the spectra in 1984 and the averaged spectra of the first and latter half of 1983 for each phase interval.

Figure 24. The simulated PHA ratios derived from the variations of the absorption column density both of neutral gas and of partially ionized gas of He-like Mg, Si, S, A, Ca, Cr and Fe with cosmic abundance. The indicated numbers are the Hydrogen column densities assuming the cosmic abundance. Comptonization by the 10 keV plasma is also shown. The indicated numbers are Compton scattering depths of the 10 keV plasma.

Figure 25. The best fit parameters of a black body model for each of four phase intervals of three parts. The data in the range 1-9 keV except for 6-7 keV were used. The black body radius derived assuming the distance to Cygnus X-3 is 12 kpc.

Figure 26. The best fit simulations with the three-components model and the residuals. (a)-(b) show the data for four phase intervals in the first half in 1983. (e)-(h) and (i)-(l) show those in the latter half in 1983 and in 1984, respectively. The histograms, A, B, and C, are the blackbody component, the thermal bremsstrahlung component, and the

power law component, respectively.

Figure 27. The best fit simulations of the observed spectra of the three-component model with the Gaussian line for the iron feature. (a)-(d), (e)-(h) and (i)-(l) show that of each phase interval integrated over each of three parts, the fast half,the later half in 1983 and 1984, respectively.

Figure 28. The properties of iron feature of the data of four phase intervals integrated over each of three parts.

Figure 29. The properties of iron feature of the data in 1983 divided into five parts (a) - (e) as shown in figure 13.

Figure 30. The properties of iron feature of the data of individual orbits of the satellite, for (a) 1983 observation and (b) 1984 observation.

Figure 31. The folded properties of the iron feature of the data of individual orbits of the satellite, for (a) 1983 observation and (b) 1984 observation.

Figure 32. The correlation of the iron feature intensity with the flux of the range 9-10 keV for the data of four phase intervals integrated over each of three parts.

Figure 33. The correlation of the iron feature intensity with the mean intensity in the range 9-10 keV for the five parts intervals, (a) - (e), in 1983, and 1984 data.

Figure 34. Two dimensional projections of the 90% and 99% confidence contours for the fitting, assuming the absorption edge of He-like iron ions of the four phase intervals over each of three parts, the first half in 1983 ((a),(b),(c) and (d)), the latter half in 1983 ((e), (f), (g) and (h)) and in 1984 ((i), (j), (k) and (l)). The parameters are the

edge energy and the column density assumed the cosmic abundance.

Figure 35. The simulation of the relation between the true column density and the observed column density and the observed edge energy when the Lymann continuum in the case of $\Omega = 4\pi$ and $Y_{Fe}=1$ is taken into account. The absorption edge is assumed to be due to the absorption of the He-like iron ions at 8.8 keV. In (a) and (b), the spectrum is assumed the power law spectrum. of the index of -4.90 corresponding to the spectrum of the 1983 observation. In (c) and (d), the spectrum is assumed the power law spectrum of the index of -2.28 corresponding to that of the 1984 observation.

Figure 36. The lines of constant q in the orbital plane. $q = (r_*/r)^2$, where r_* is the distance from the center of the companion star and r is the distance from the X-ray star.

Figure 37. The energy exchange rate of the plasma irradiated by X-rays and γ-rays in the cases of (a) $n=3\times10^{13}$, kT=9keV, and the power law index(α)=2.5 of the γ-ray spectrum and the X-ray luminosity of 2×10^{38}erg/sec. and (b) $n=3\times10^{13}$, kT=100keV, the power law index(α)=2.1 and the X-ray luminosity of 0.5×10^{38}erg/sec.

Figure 38. The schematic illustration of the hot gas model. Cygnus X-3 is a close binary system containing a neutron star and a normal companion star which has the separation of about 10^{11}cm. The system is enshrouded with matter, which is not shown in the figure. The X-rays and γ-rays are emitted around the neutron star. The matter in inner region on the orbital scale is fully ionized and has high temperature

(several tens keV) by the energy supply of mainly γ-rays, which is shown by a dashed circle.

Figure 39. The monte carlo simulation of the light curve of the energy of several keV for the density distribution of $3\times10^{13}r_{11}^{-2}$.

Figure 40. The monte carlo simulation of the PHA ratios of the model illustrated in figure 38 having the density distribution of $3\times10^{13}r_{11}^{-2}$ and the temperature of the hot region of 10 keV. The open circles are the simulated data and the cross symbols are the observed data. (a) is the PHA ratio of the intermediate intensity phase to the maximum intensity phase. (b) is that of the minimum intensity phase to the maximum intensity phase.

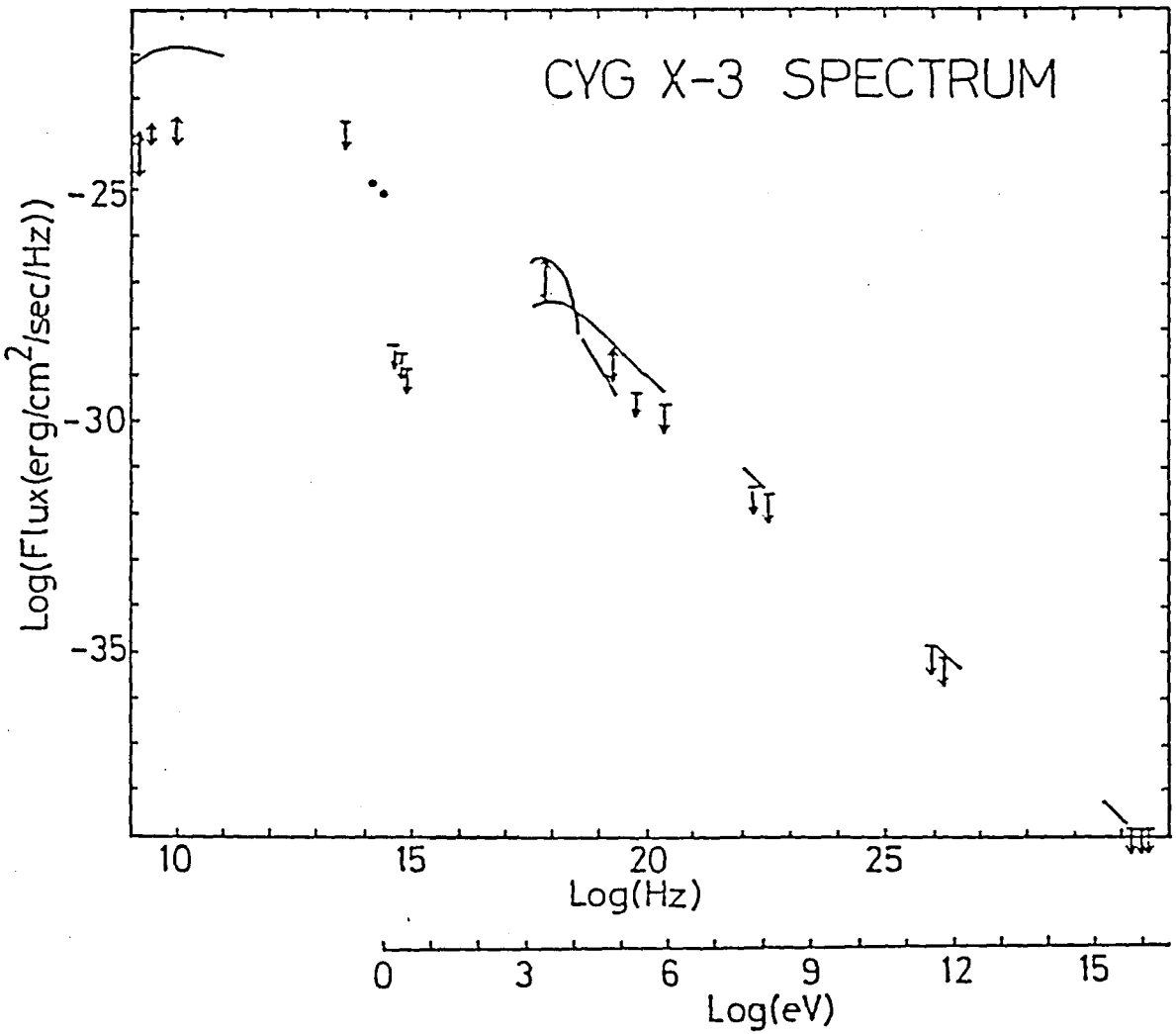
CYG X-3 SPECTRUM
Log(Flux(erg/cm²/sec/Hz))
-25
-30
-35
10
15
20
25
Log(Hz)
0
3
6
9
12
15
Log(eV)

Figure - 1.

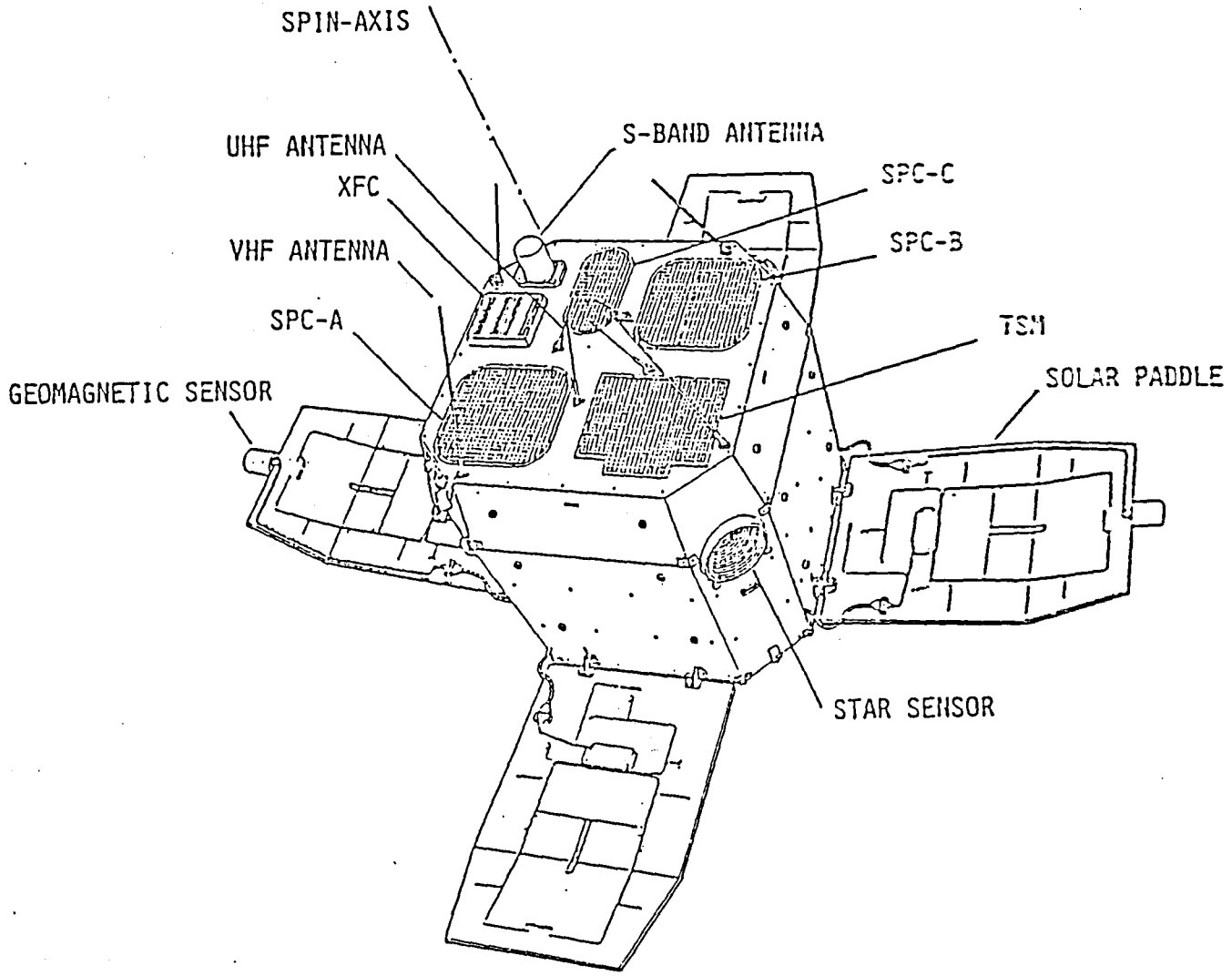
SPIN-AXIS
UHF ANTENNA
XFC
VHF ANTENNA
SPC-A
GEOMAGNETIC SENSOR
S-BAND ANTENNA
SPC-C
SPC-B
TSM
SOLAR PADDLE
STAR SENSOR

Figure - 2.

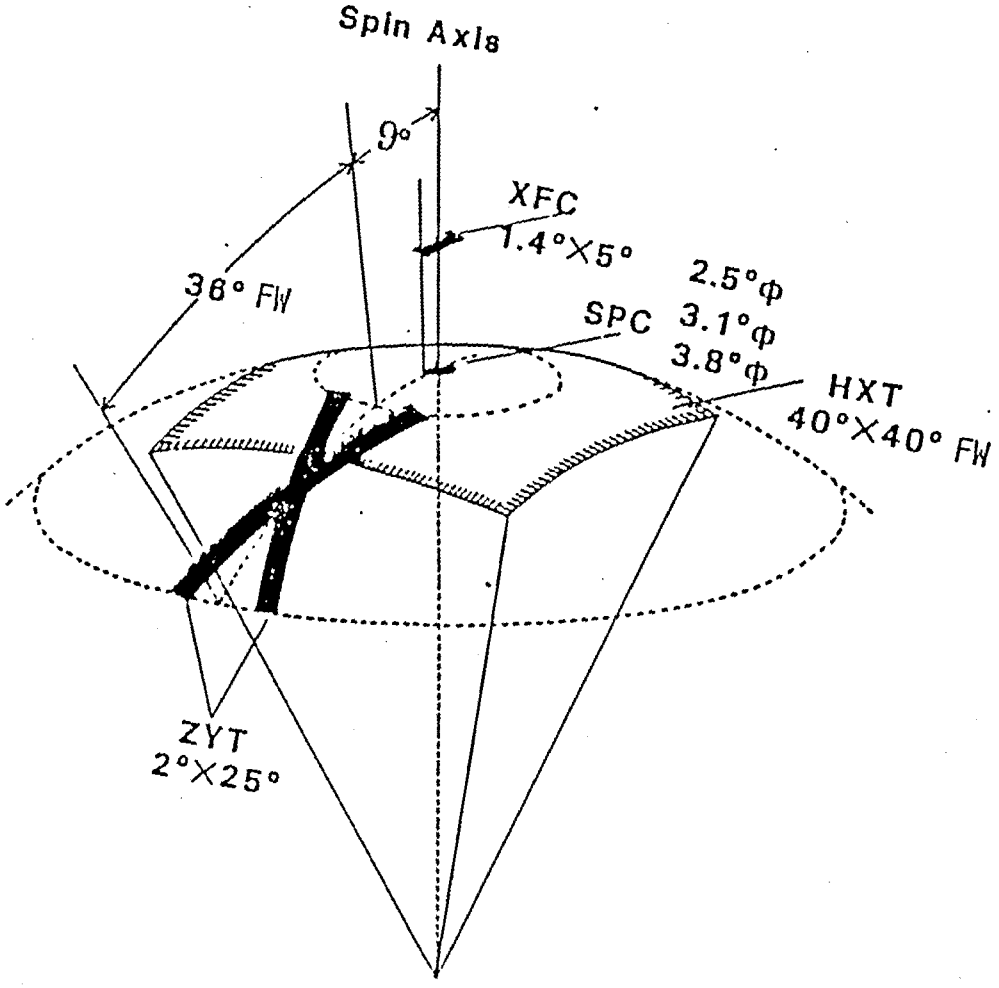

Figure - 3.

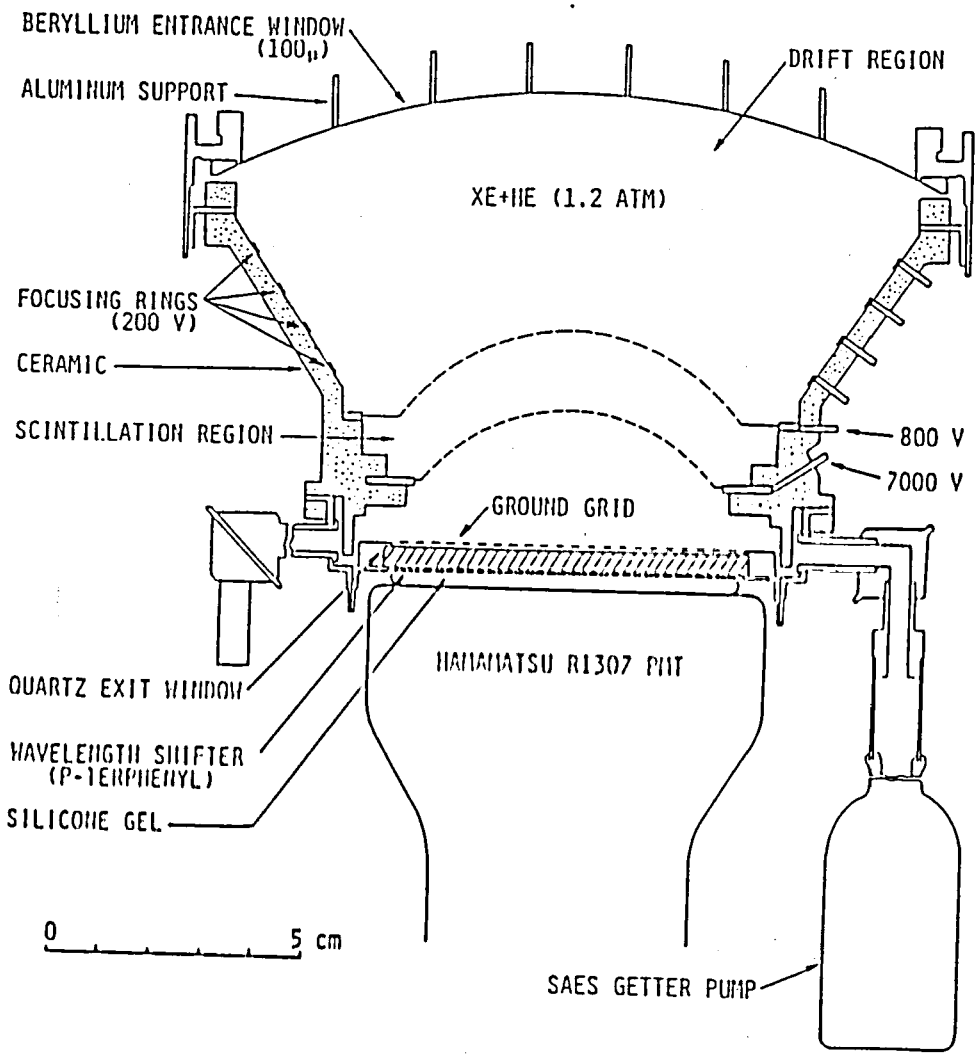
BERYLLIUM ENTRANCE WINDOW (100μ)
ALUMINUM SUPPORT
DRIFT REGION
XE+HE (1.2 ATM)
FOCUSING RINGS (200 V)
CERAMIC
SCINTILLATION REGION
800 V
7000 V
GROUND GRID
HAMAMATSU R1307 PMT
QUARTZ EXIT WINDOW
WAVELENGTH SHIFTER (P-TERPHENYL)
SILICONE GEL
0
5 cm
SAES GETTER PUMP

Figure - 4.

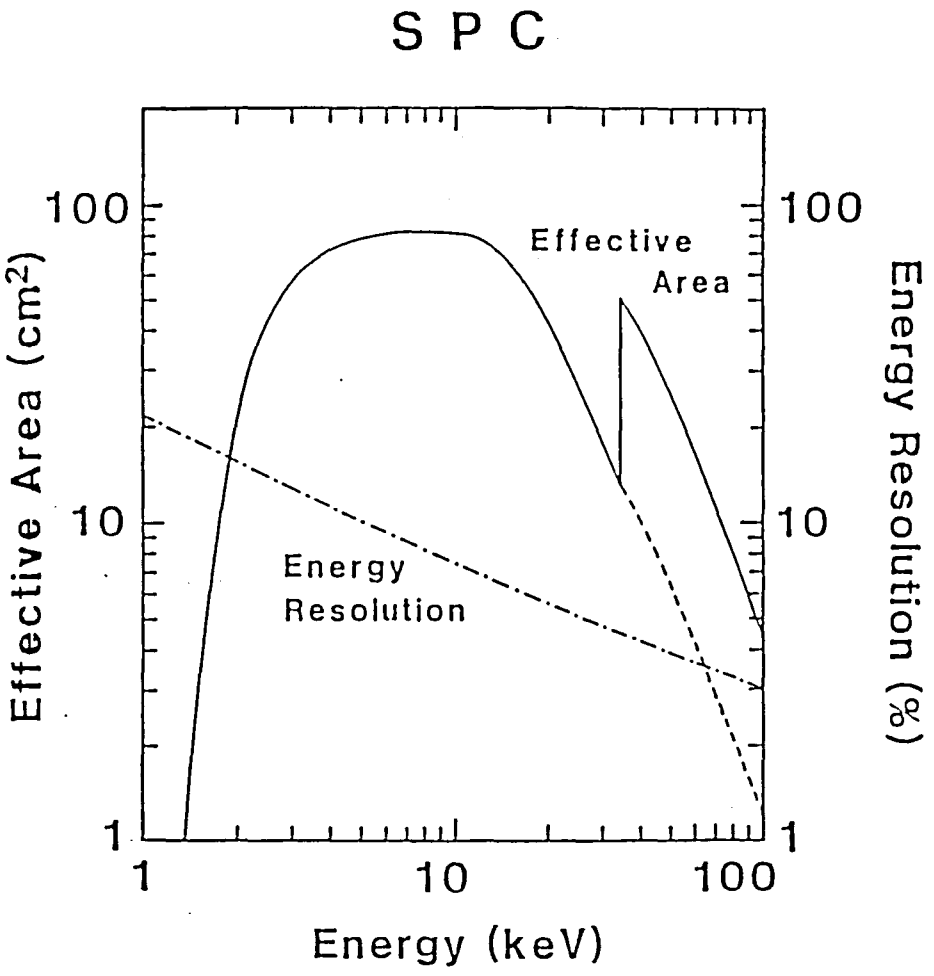
S P C
100
10
1
1
10
100
Effective Area (cm²)
Energy Resolution (%)
Energy (keV)
Effective Area
Energy Resolution

Figure - 5.

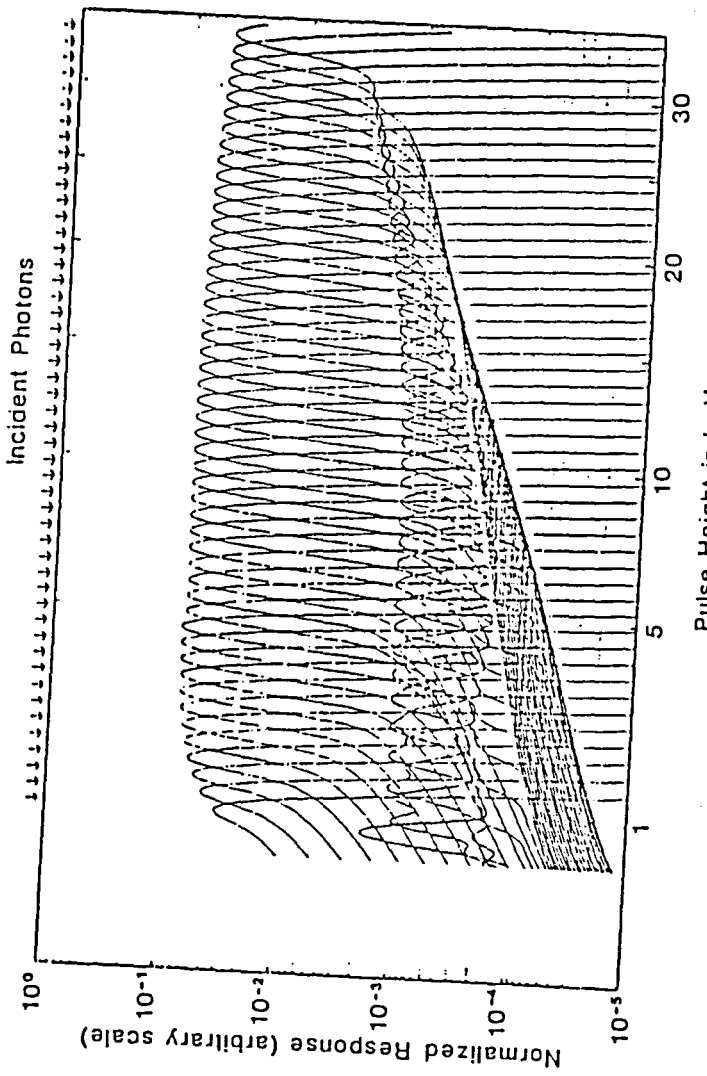
Incident Photons
Normalized Response (arbitrary scale)
10⁰
10⁻¹
10⁻²
10⁻³
10⁻⁴
10⁻⁵
1
5
10
20
30
Pulse Height in keV

Figure - 6.

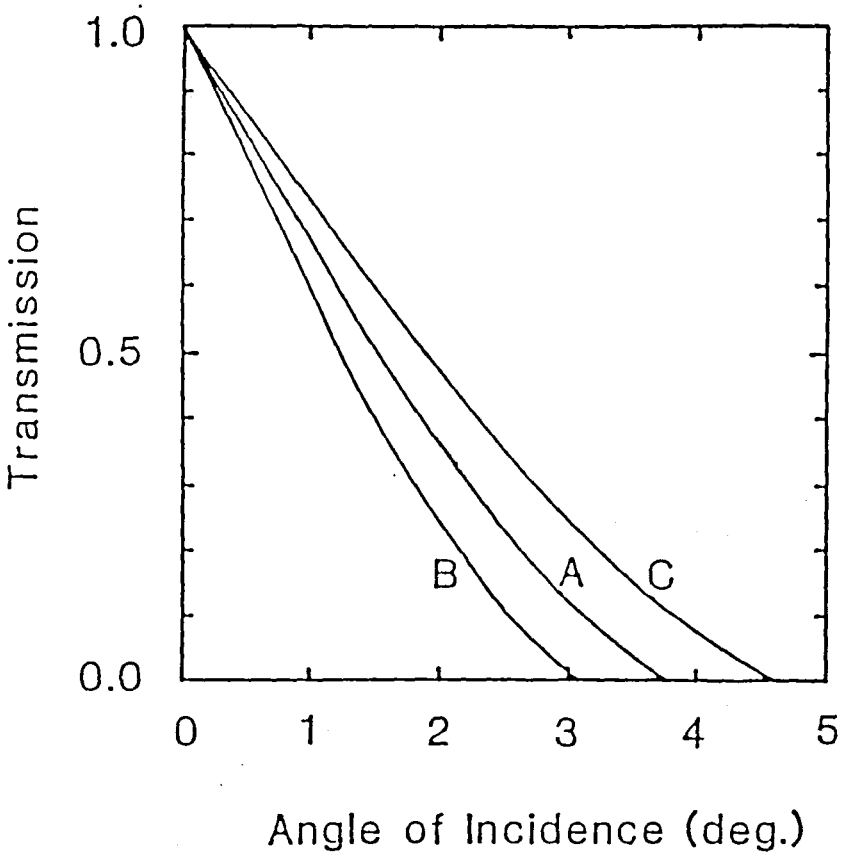

Figure - 7.

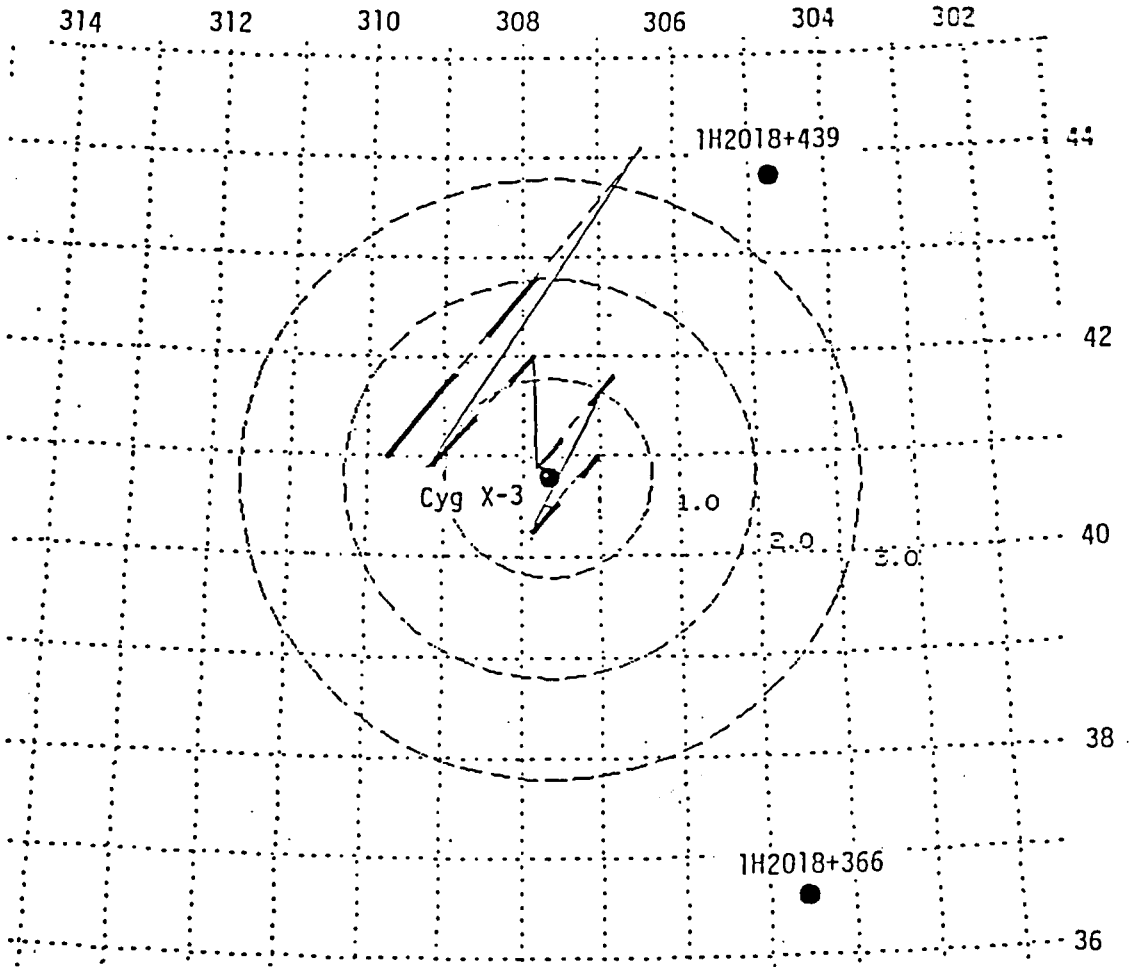
314
312
310
308
306
304
302
44
42
40
38
36
1H2018+439
1H2018+366
Cyg X-3
1.0
2.0
3.0

Figure - 8.

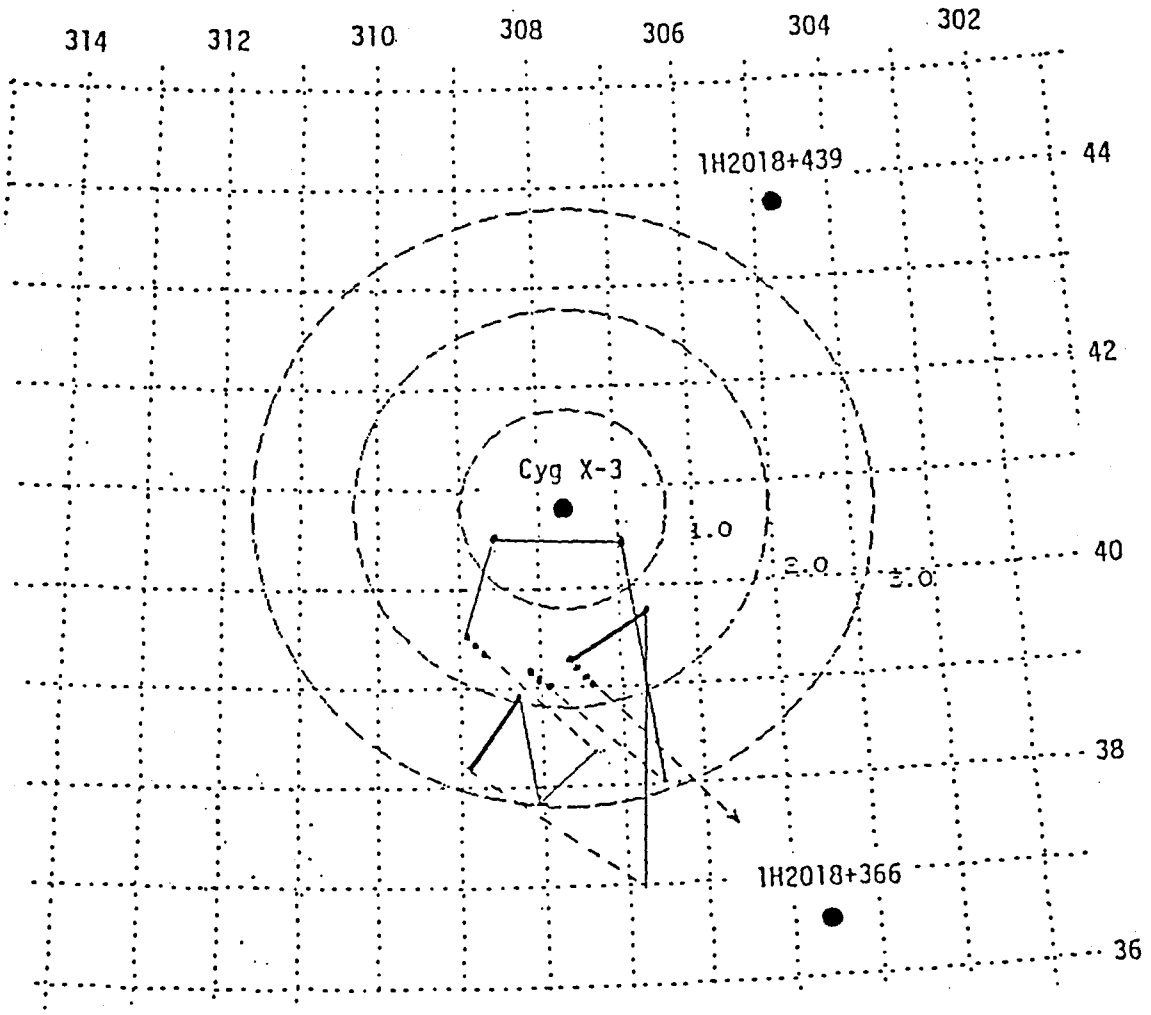
314
312
310
308
306
304
302
44
42
40
38
36
1H2018+439
Cyg X-3
1.0
2.0
3.0
1H2018+366

Figure - 9.

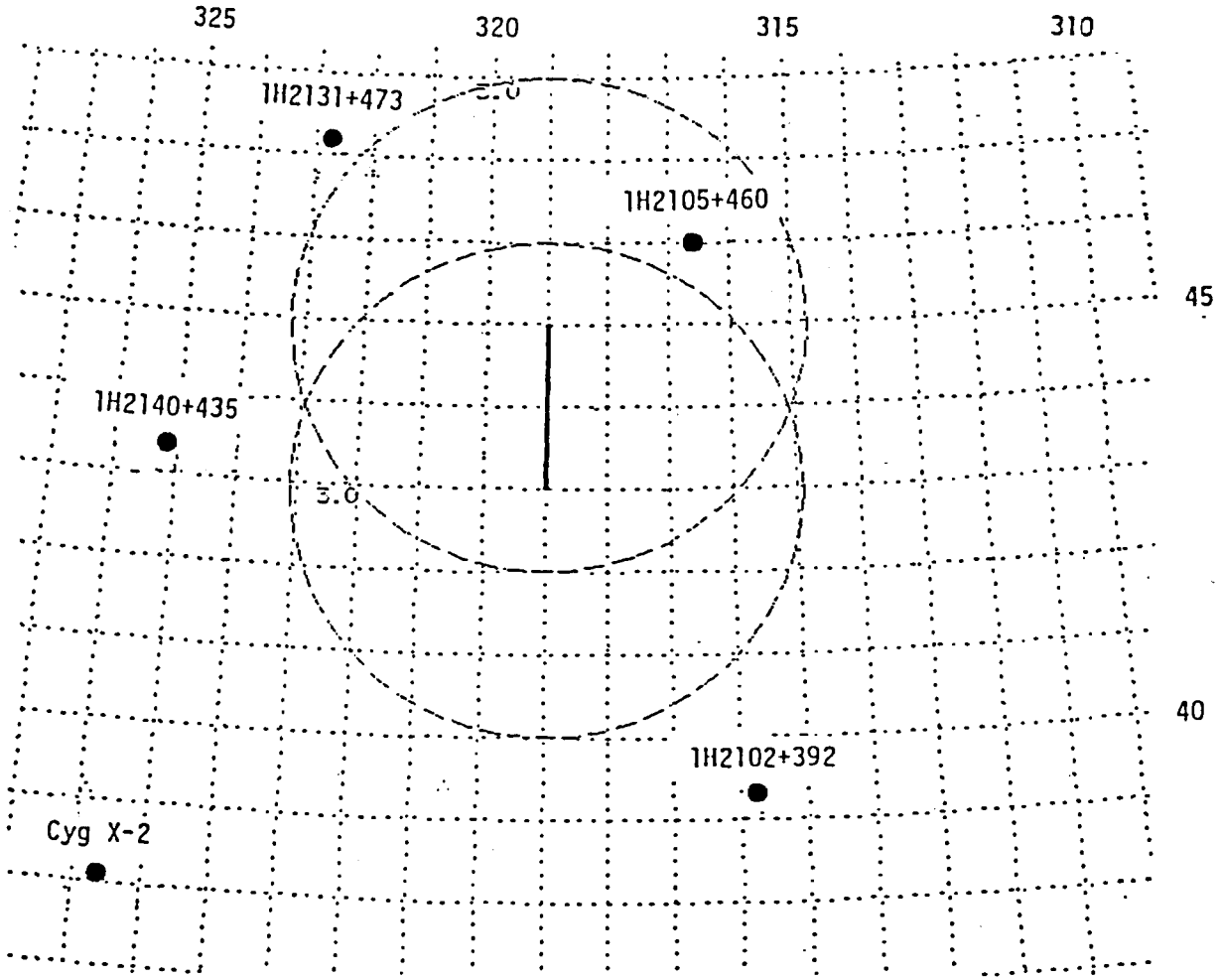
325
320
315
310
45
40
1H2131+473
1H2105+460
1H2140+435
1H2102+392
Cyg X-2
3.0

Figure - 10.

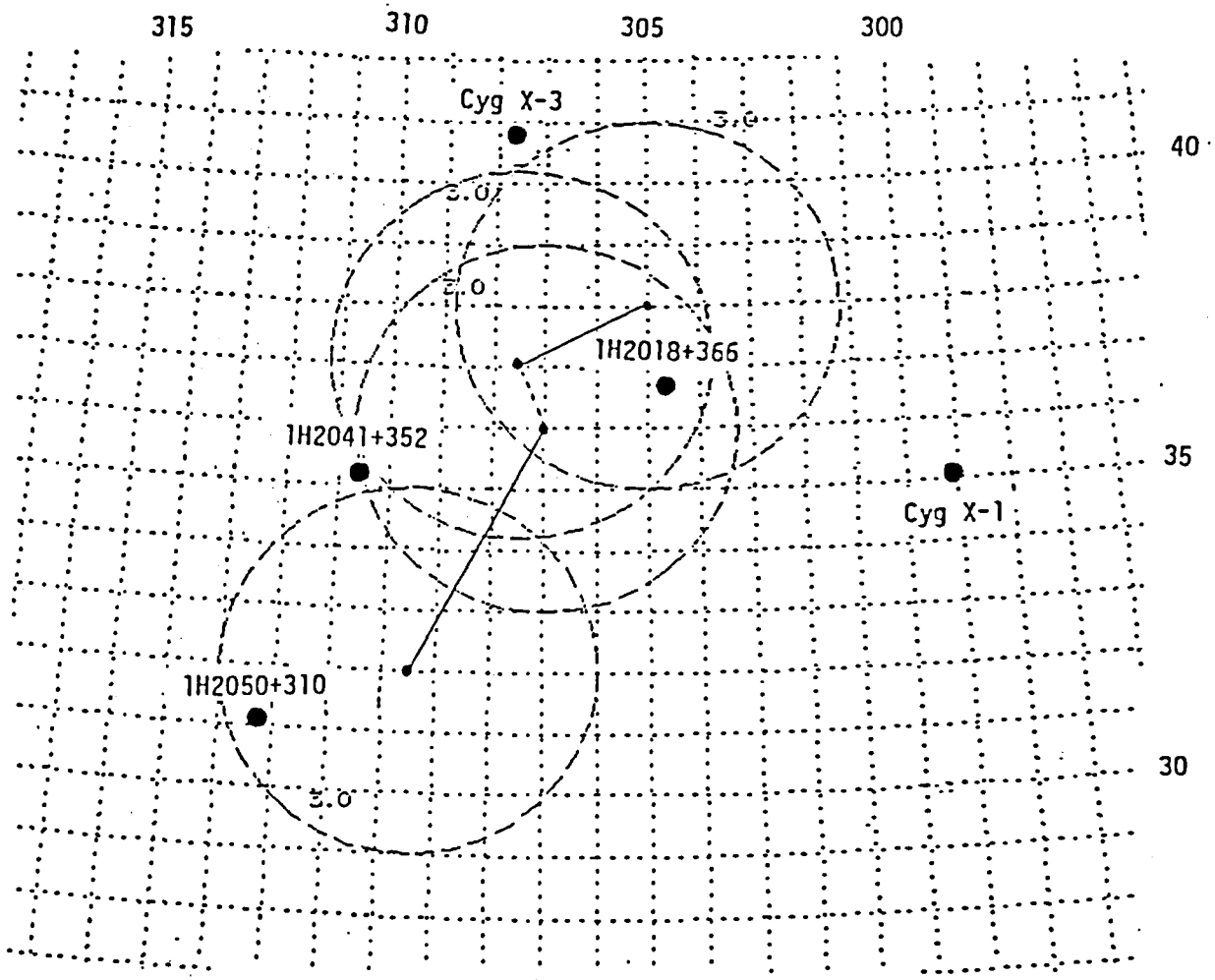
315
310
305
300
40
35
30
Cyg X-3
3.0
2.0
1H2018+366
1H2041+352
Cyg X-1
1H2050+310
3.0

Figure - 11.

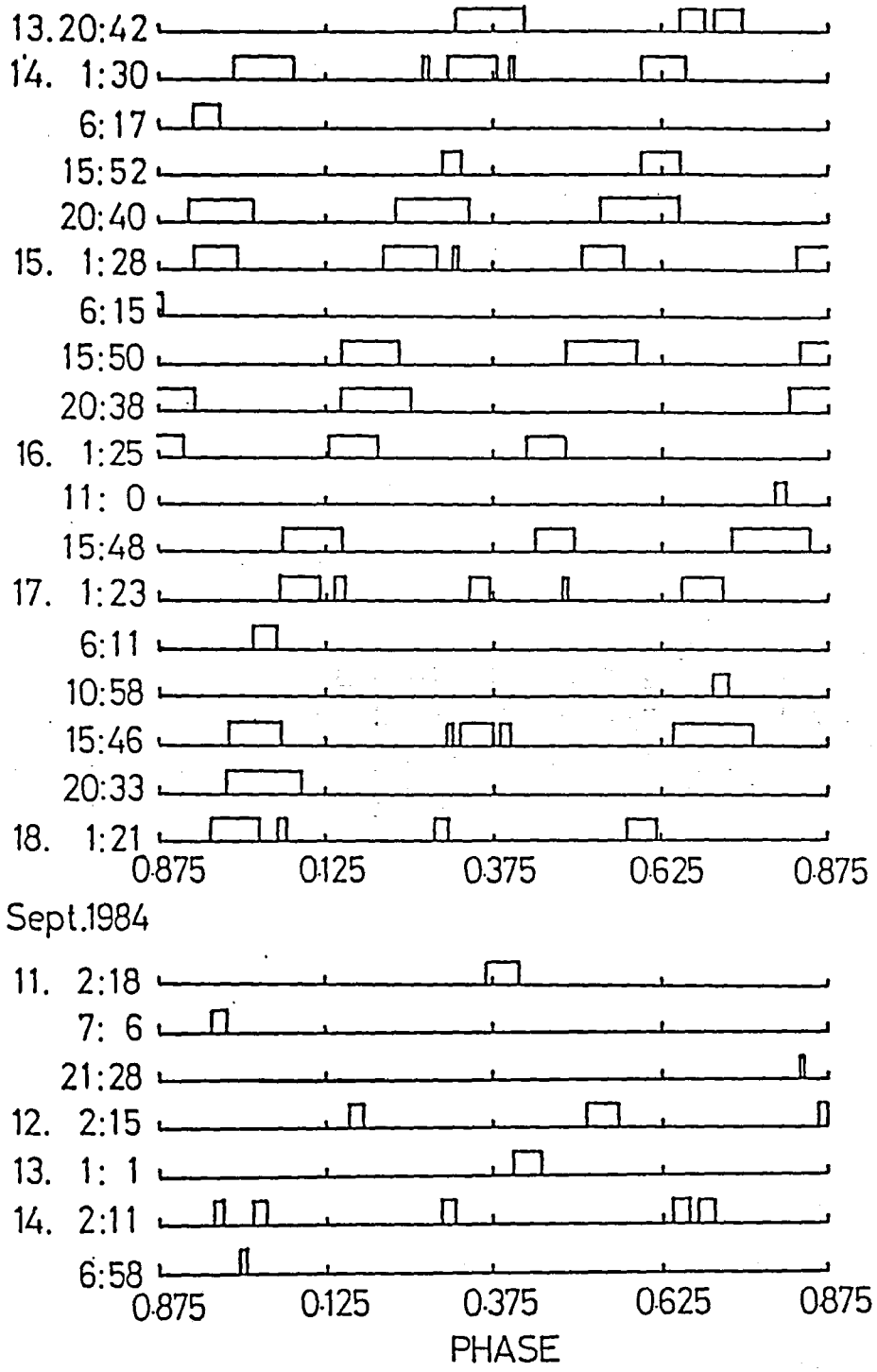
Sept.1983
13.20:42
14. 1:30
6:17
15:52
20:40
15. 1:28
6:15
15:50
20:38
16. 1:25
11: 0
15:48
17. 1:23
6:11
10:58
15:46
20:33
18. 1:21
0.875
0.125
0.375
0.625
0.875
Sept.1984
11. 2:18
7: 6
21:28
12. 2:15
13. 1: 1
14. 2:11
6:58
0.875
0.125
0.375
0.625
0.875
PHASE

Figure - 12

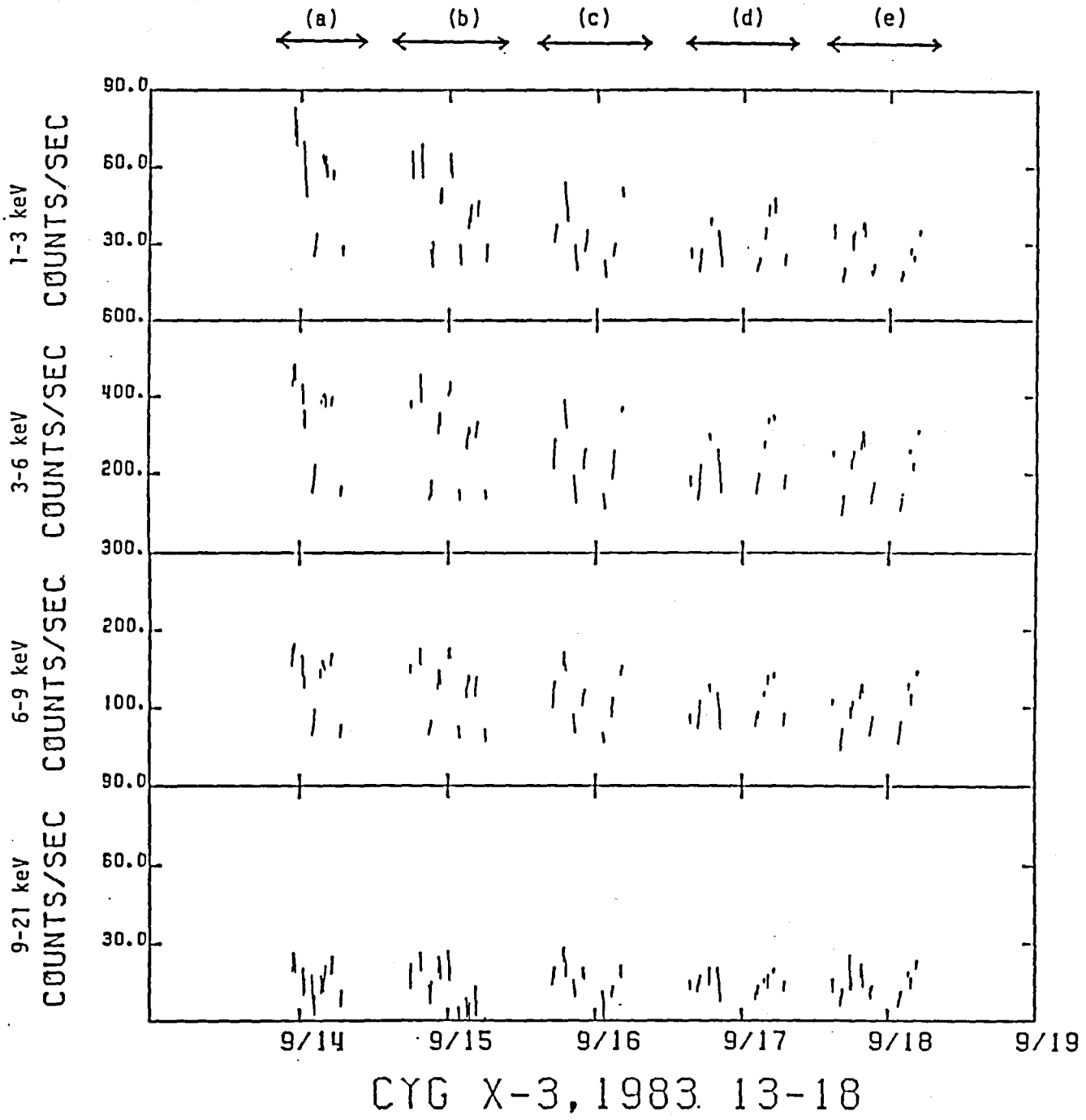
(a)
(b)
(c)
(d)
(e)
90.0
60.0
30.0
600.
400.
200.
300.
200.
100.
90.0
60.0
30.0
1-3 keV
3-6 keV
6-9 keV
9-21 keV
COUNTS/SEC
COUNTS/SEC
COUNTS/SEC
COUNTS/SEC
9/14
9/15
9/16
9/17
9/18
9/19
CYG X-3, 1983 13-18

(a)

Figure - 13.

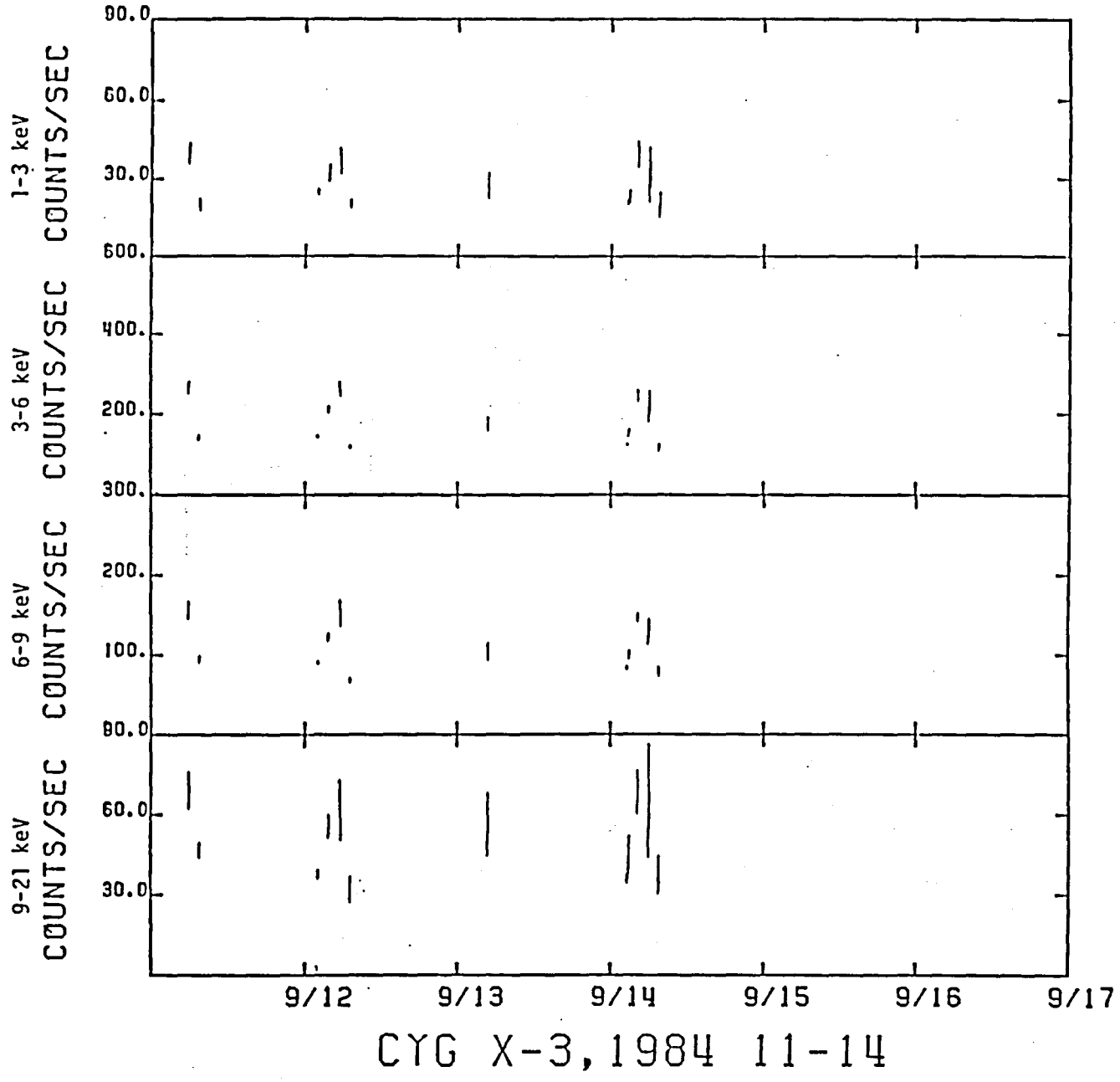
1-3 keV
COUNTS/SEC
90.0
60.0
30.0
3-6 keV
COUNTS/SEC
600.
400.
200.
6-9 keV
COUNTS/SEC
300.
200.
100.
9-21 keV
COUNTS/SEC
80.0
60.0
30.0
9/12
9/13
9/14
9/15
9/16
9/17
CYG X-3, 1984 11-14

(b)

Figure - 13.

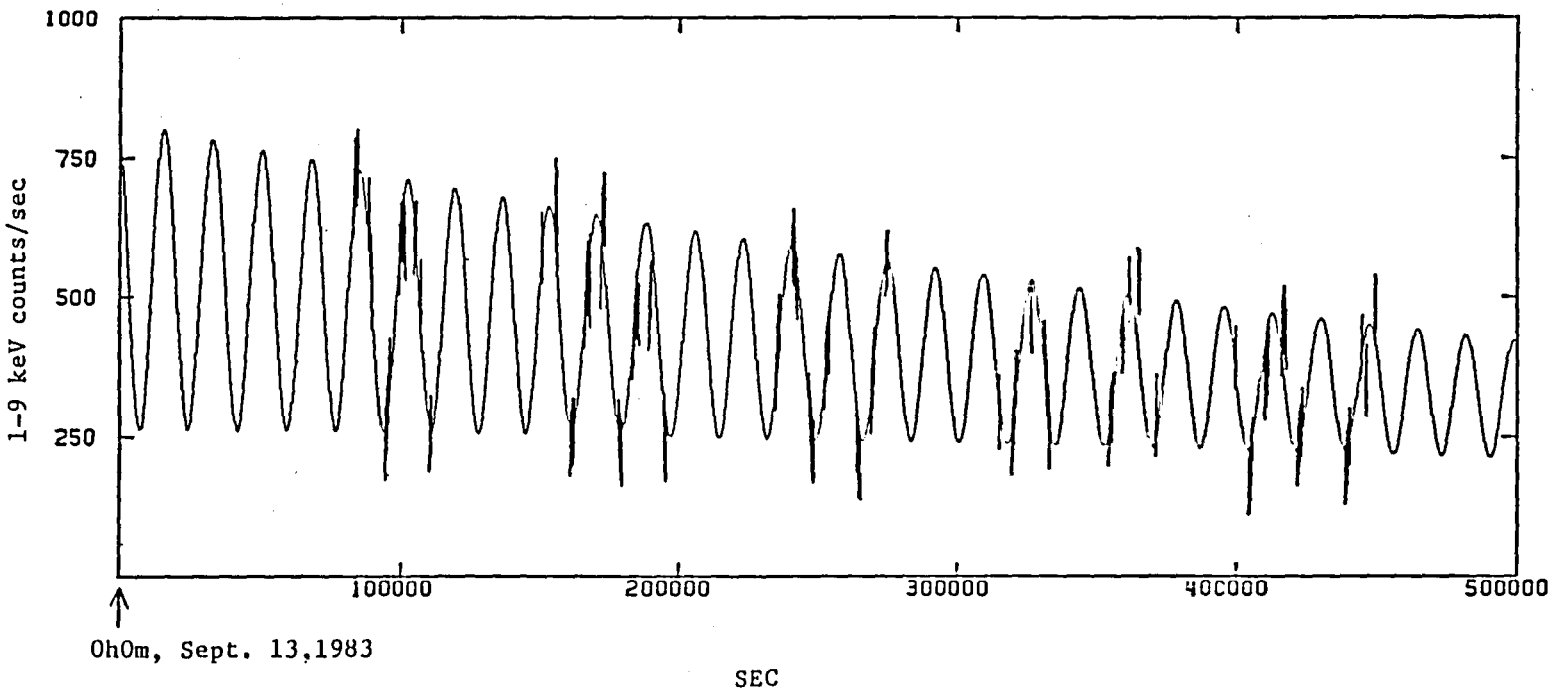
1000
750
500
250
1-9 keV counts/sec
100000
200000
300000
400000
500000
0h0m, Sept. 13,1983
SEC

Figure - 14.

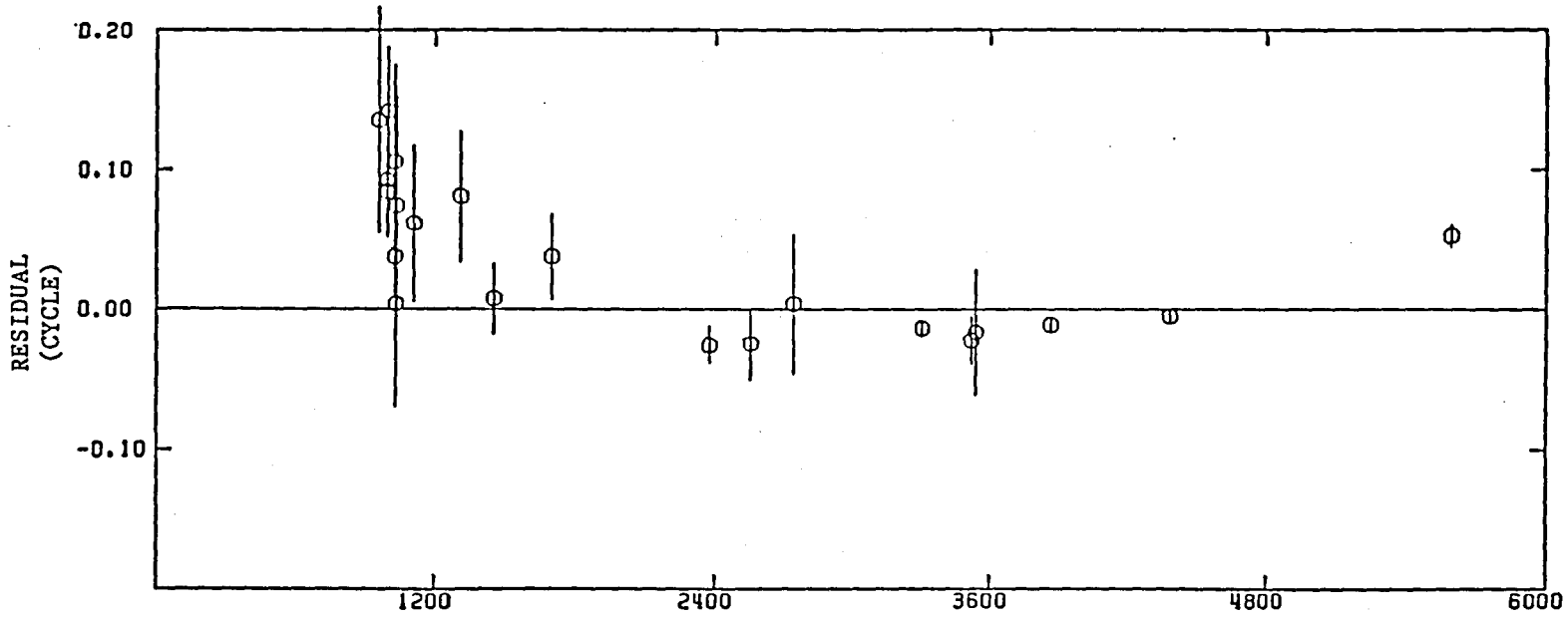
0.20
0.10
0.00
-0.10
RESIDUAL
(CYCLE)
1200
2400
3600
4800
6000
JD - 2440000

Figure - 15.

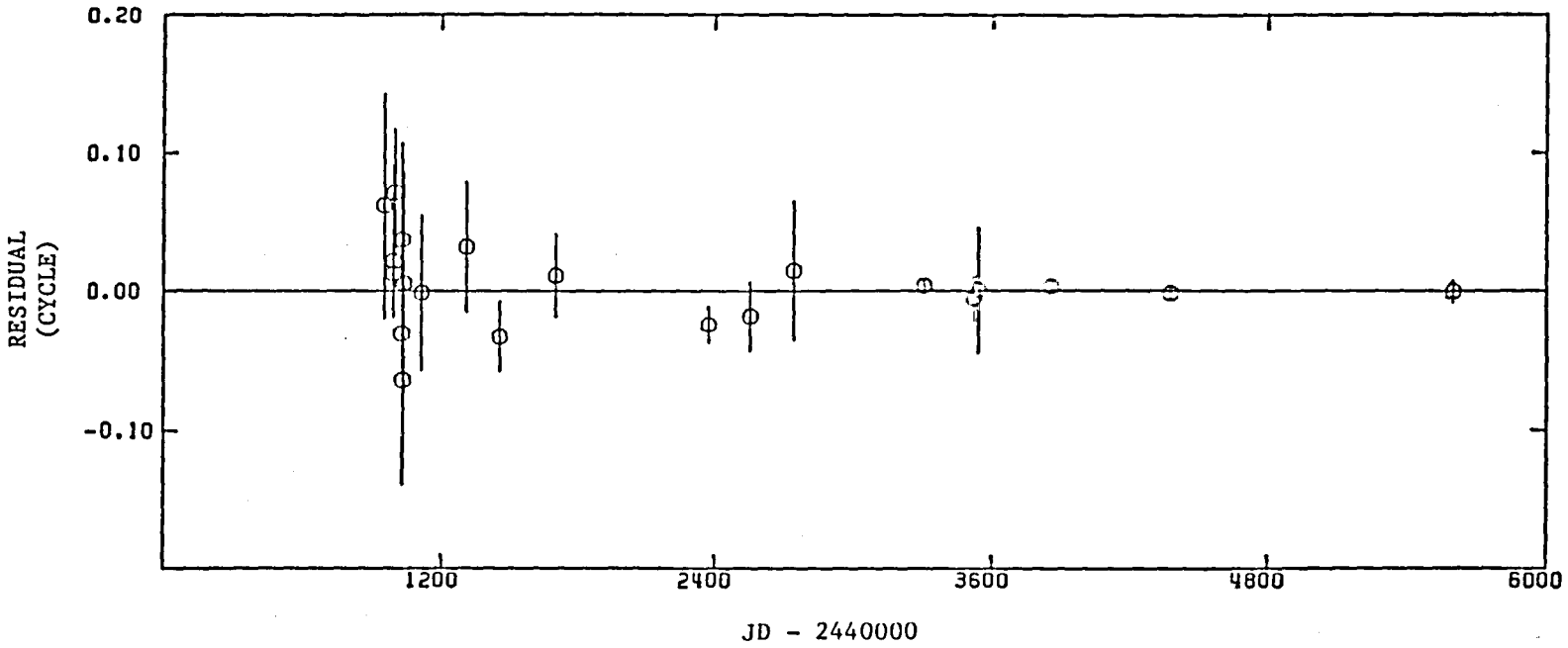
0.20
0.10
0.00
-0.10
RESIDUAL
(CYCLE)
1200
2400
3600
4800
6000
JD - 2440000

Figure - 16.

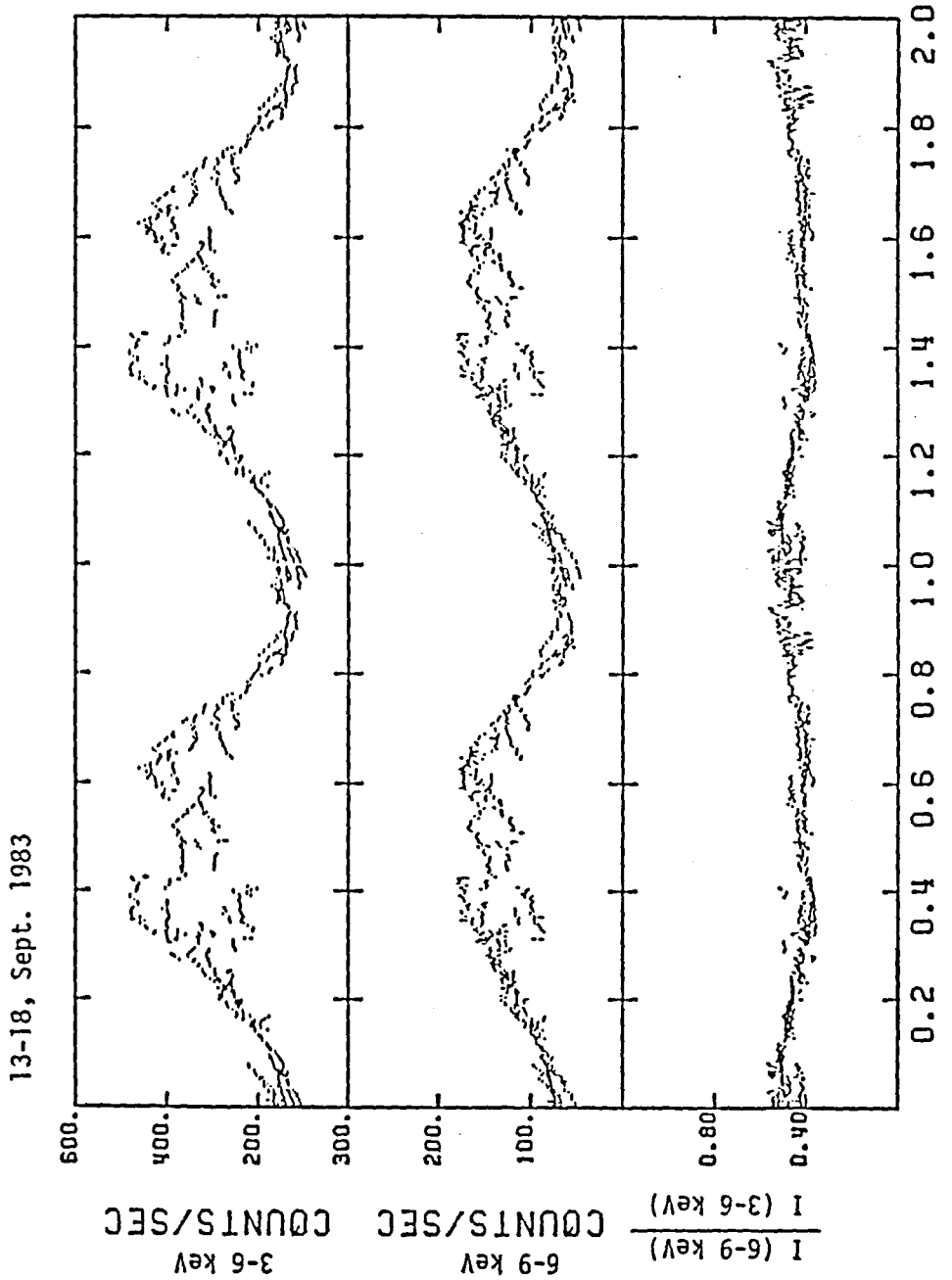
13-18, Sept. 1983
600.
400.
200.
3-6 keV
COUNTS/SEC
300.
200.
100.
6-9 keV
COUNTS/SEC
0.80
0.40
I (6-9 keV) / I (3-6 keV)
0.2
0.4
0.6
0.8
1.0
1.2
1.4
1.6
1.8
2.0
PHASE

(a)

Figure - 17.

11-14, Sept. 1984

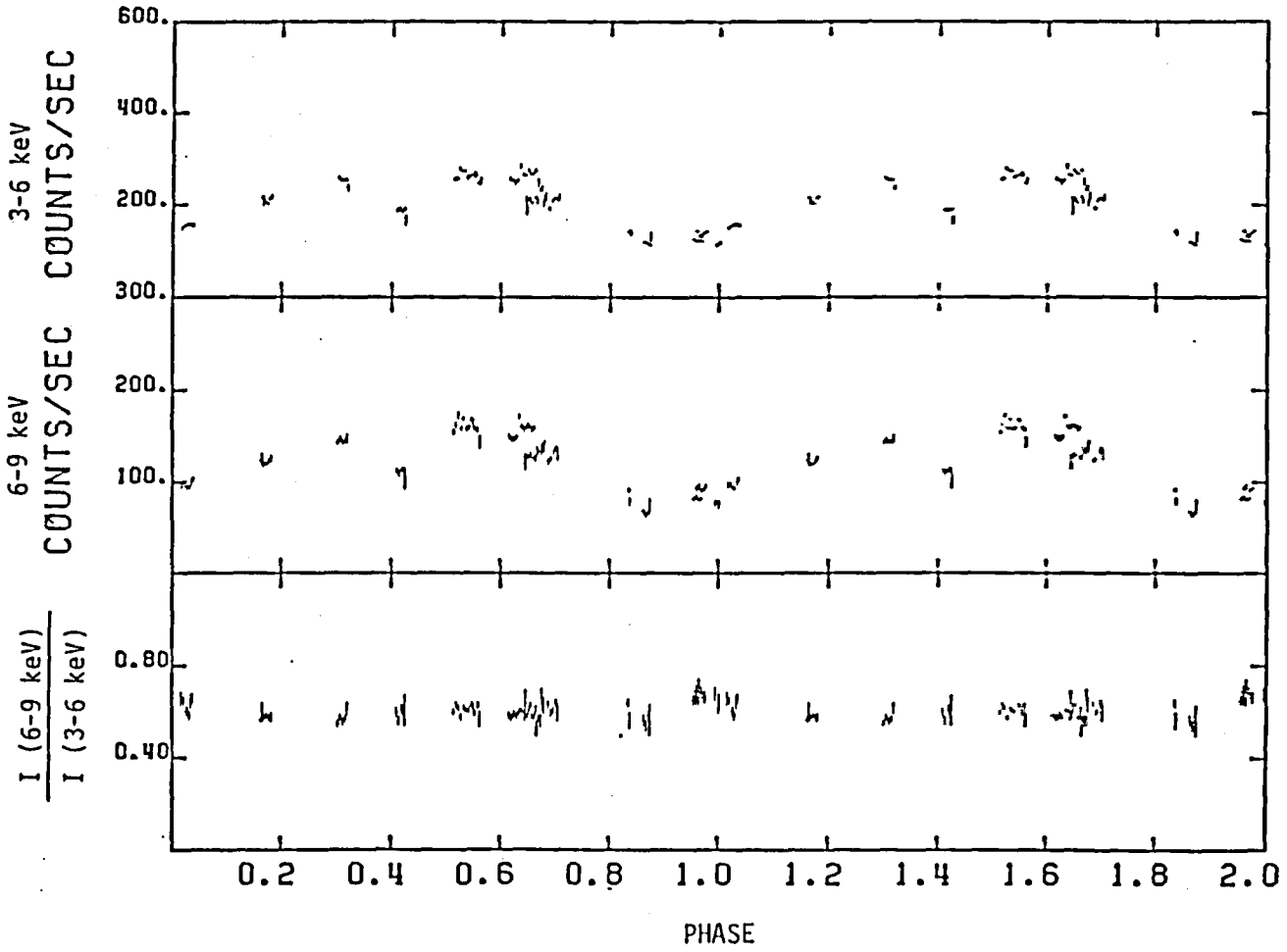

(b)

Figure - 17.

13-15, Sept. 1983

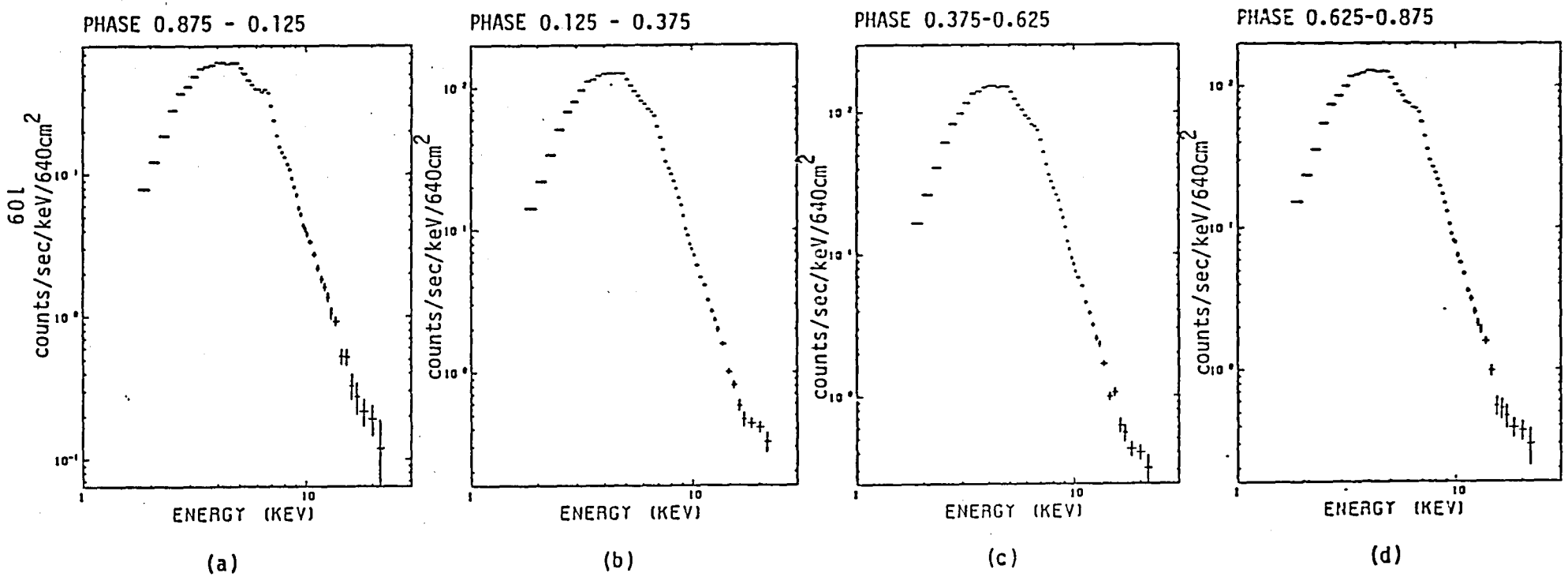

Figure - 18.

16-18, Sept. 1983

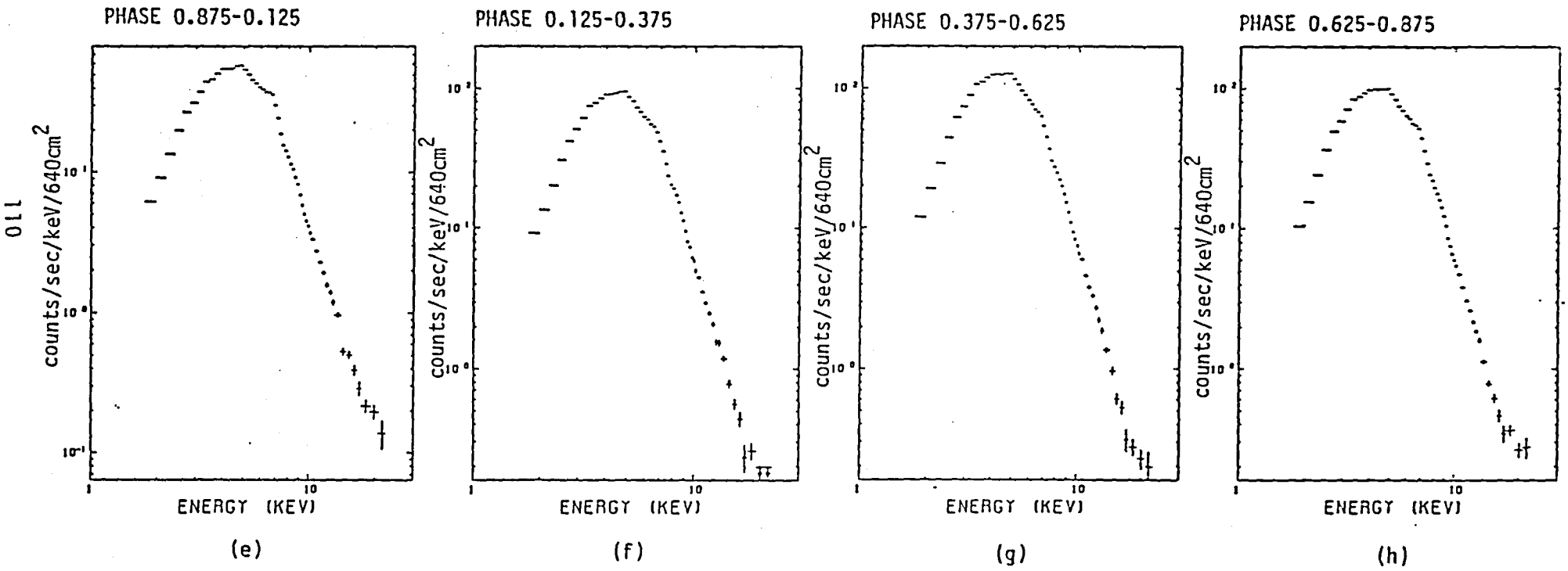

Figure - 18.

11-14, Sept. 1984

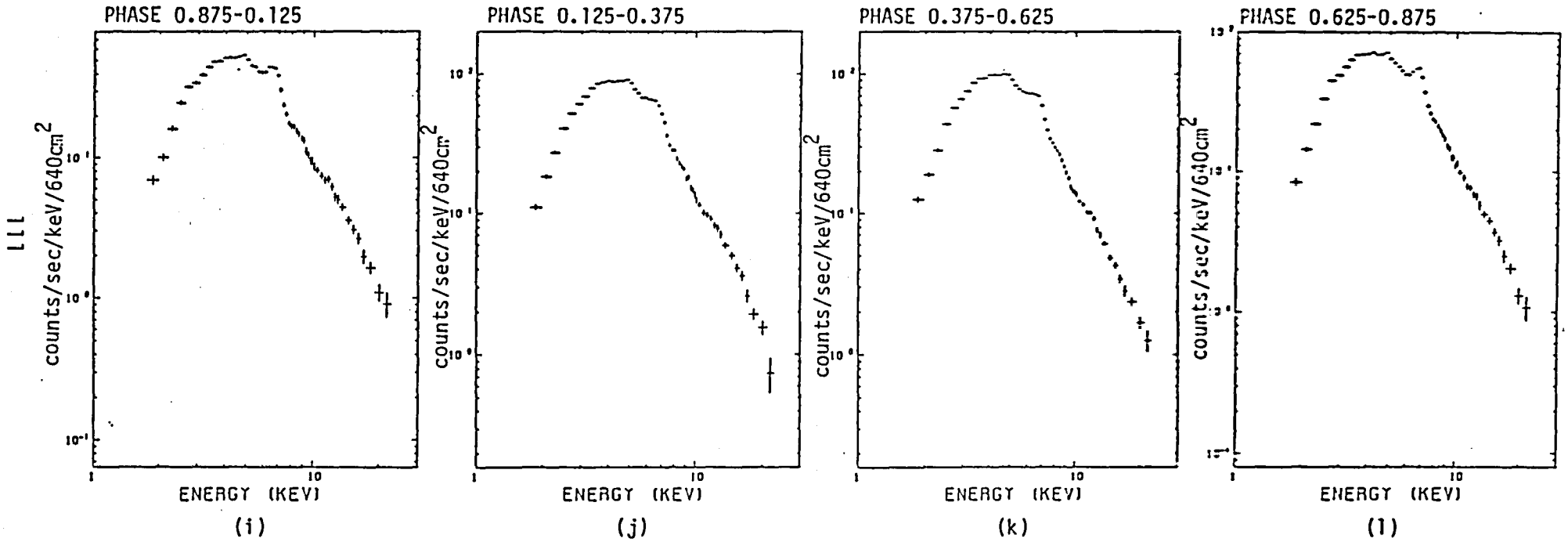

Figure - 18.

13-15, Sept. 1983

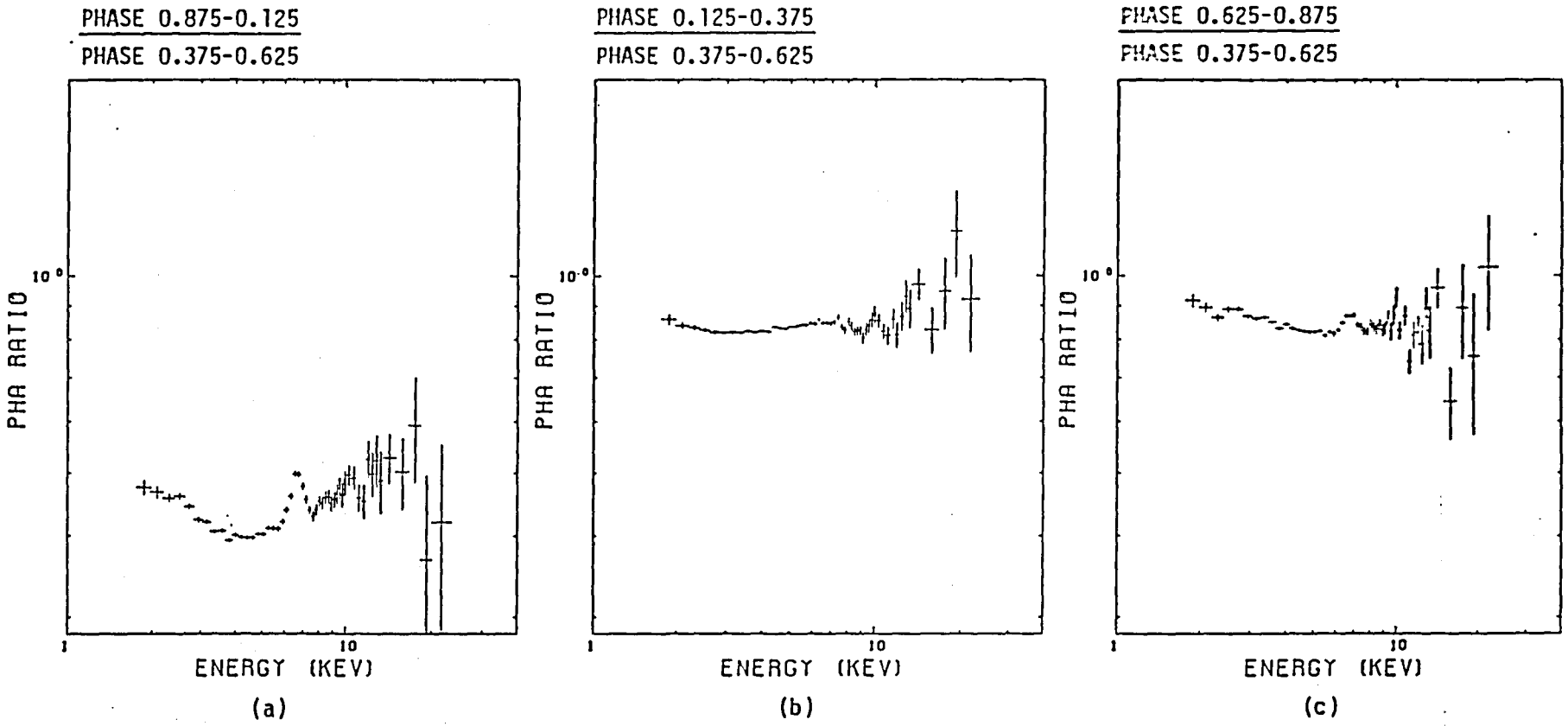

Figure - 19.

16-18, Sept. 1983

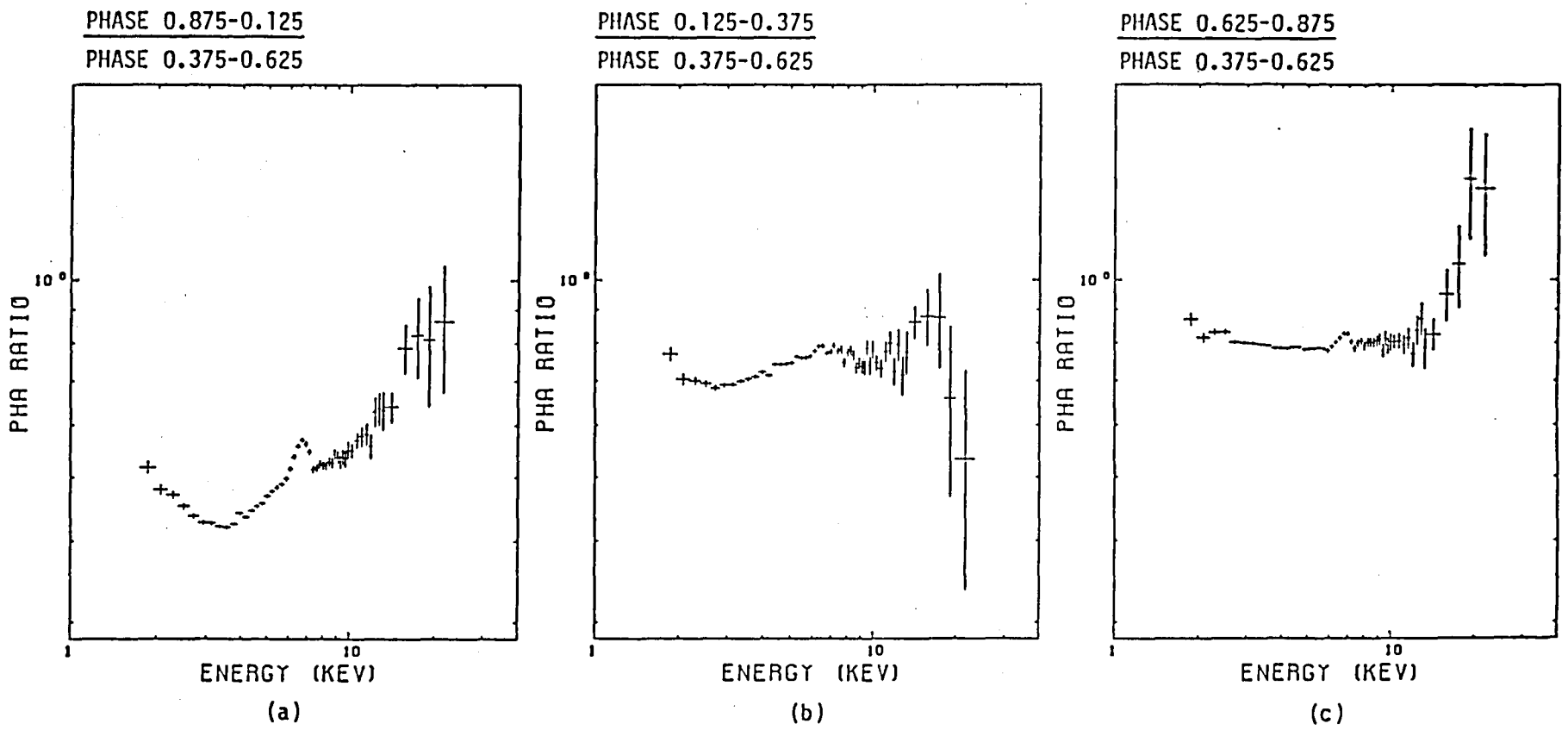

Figure - 20.

11-14, Sept. 1984

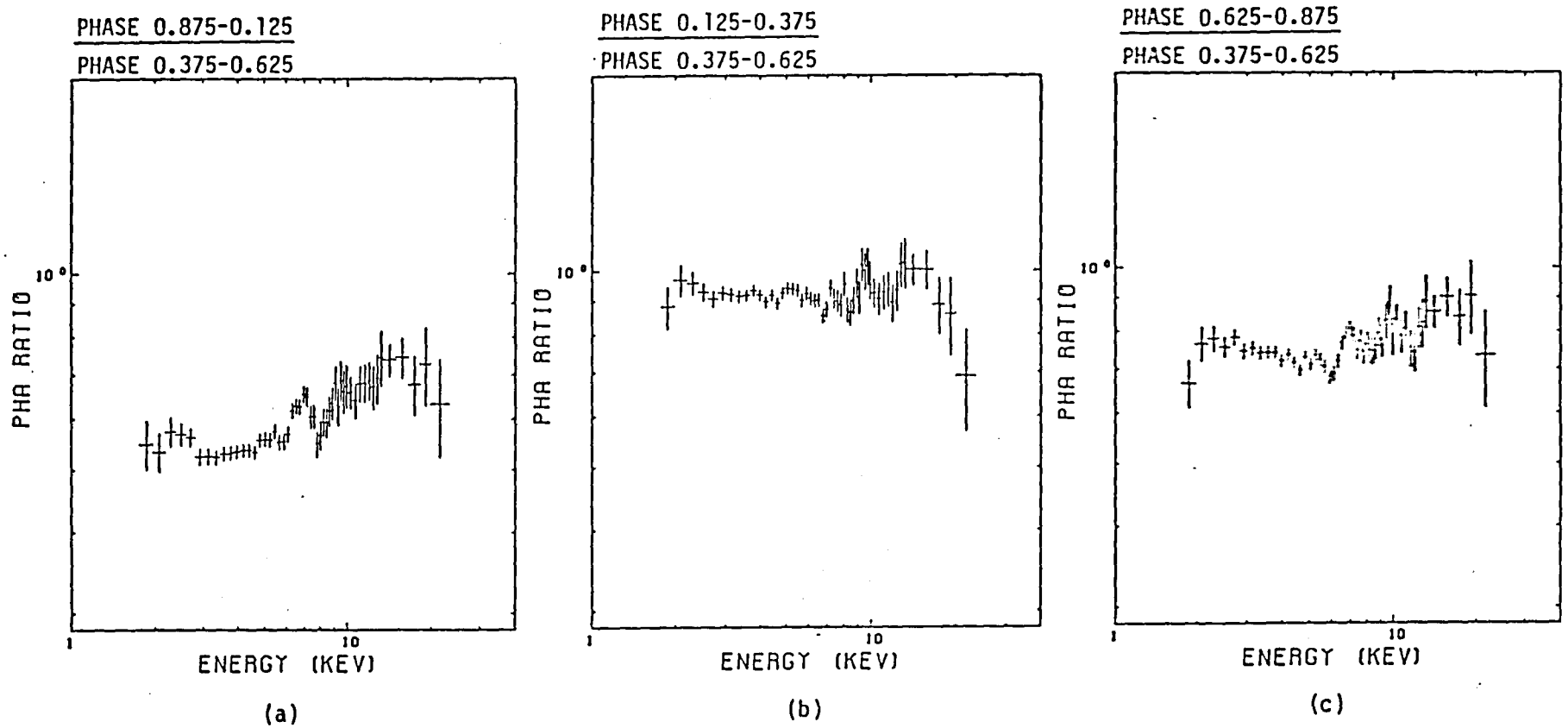

Figure - 21.

16-18, Sept. 1983

13-15, Sept. 1983

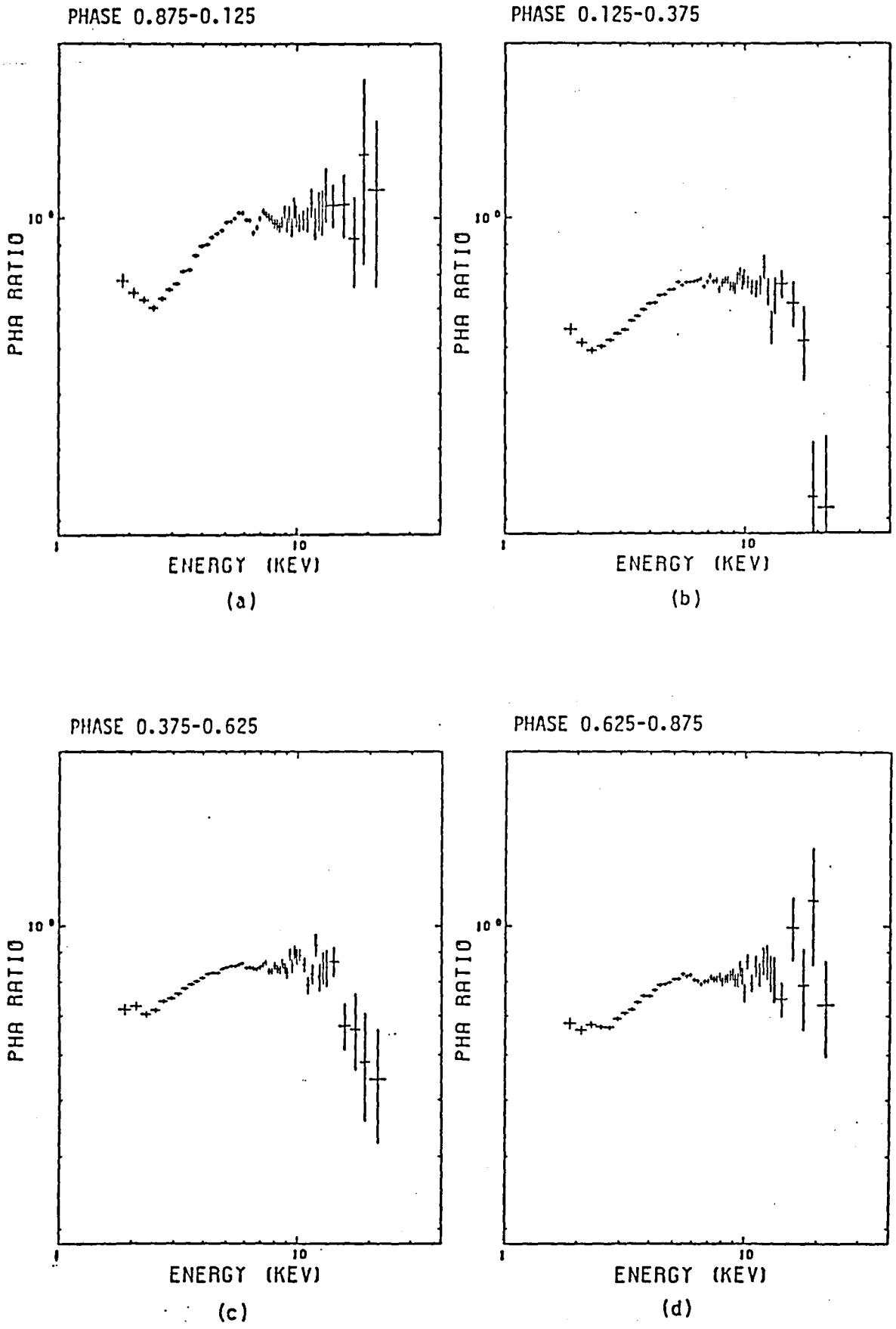

Figure - 22.

11-14, Sept. 1984

13-18, Sept. 1983

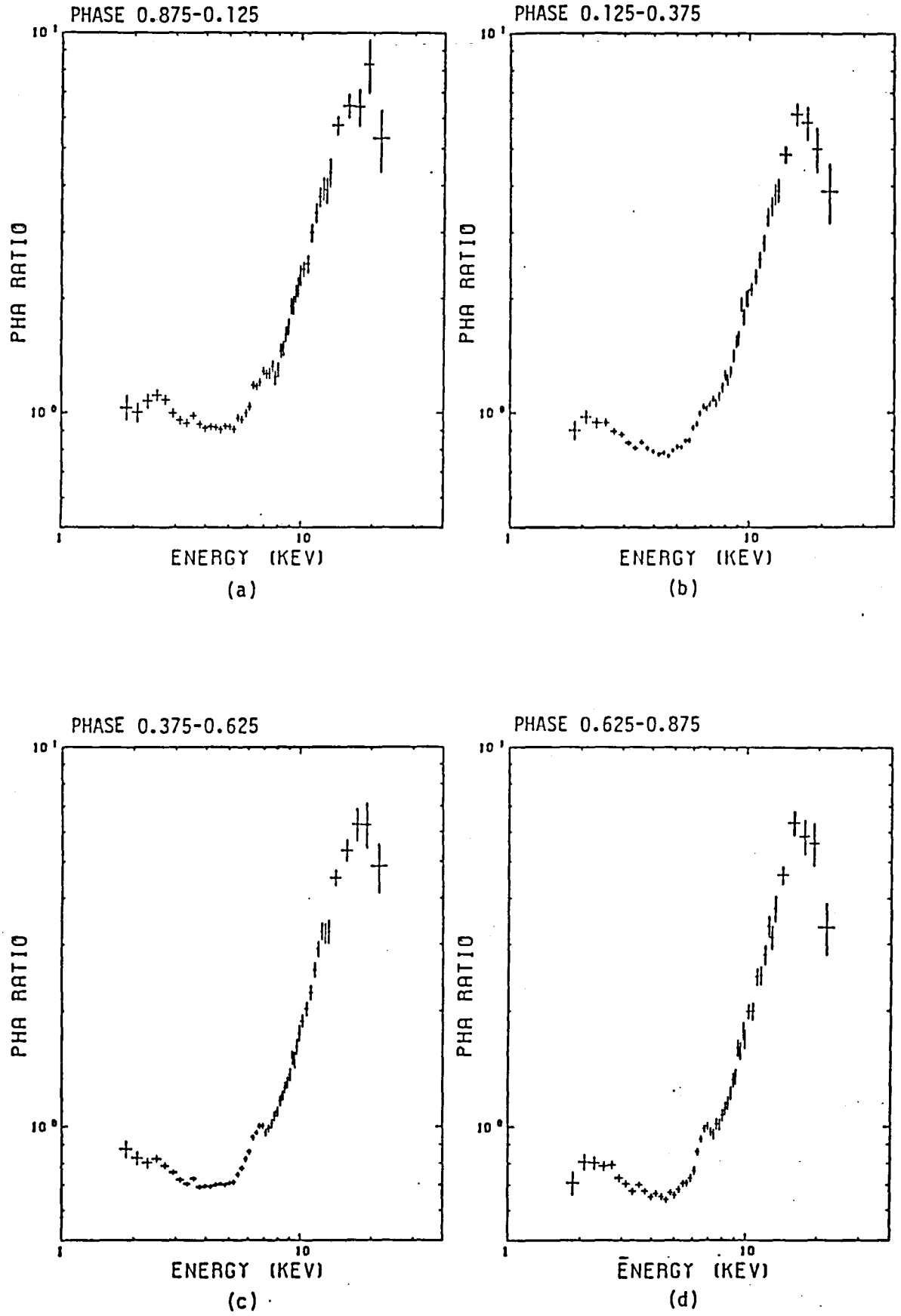

Figure - 23.

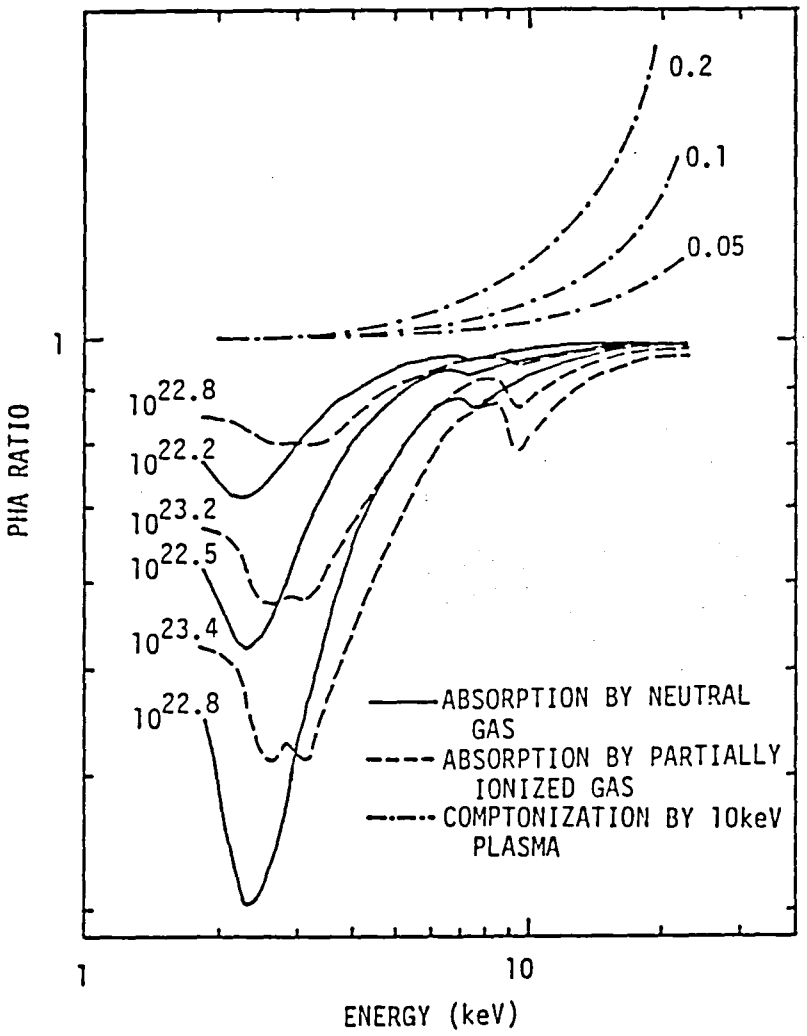
0.2
0.1
0.05
1
$10^{22.8}$
$10^{22.2}$
$10^{23.2}$
$10^{22.5}$
$10^{23.4}$
$10^{22.8}$
ABSORPTION BY NEUTRAL GAS
ABSORPTION BY PARTIALLY IONIZED GAS
COMPTONIZATION BY 10keV PLASMA
PHA RATIO
1
10
ENERGY (keV)

Figure-24.

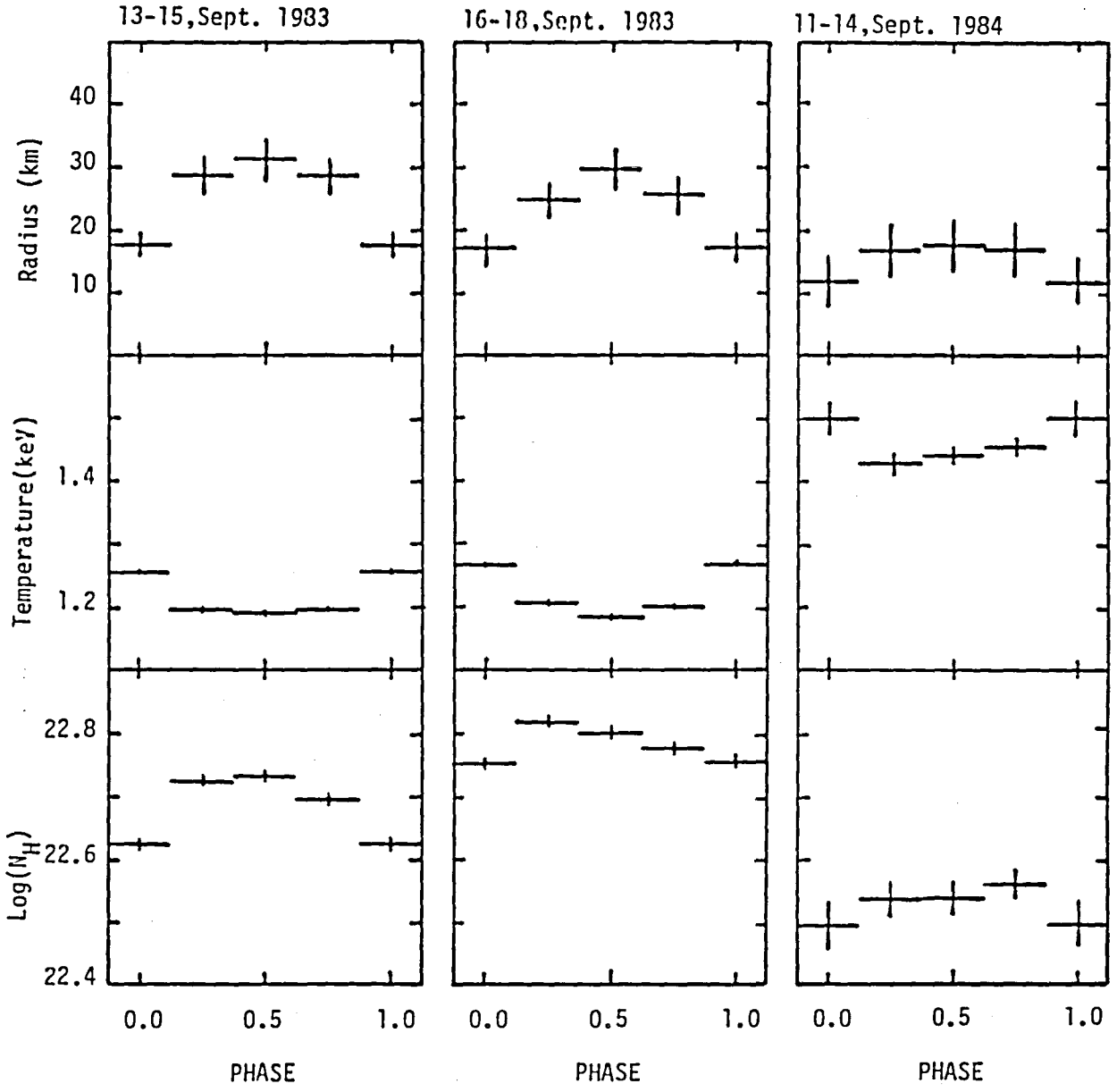
13-15,Sept. 1983
16-18,Sept. 1983
11-14,Sept. 1984
Radius (km)
40
30
20
10
Temperature(keV)
1.4
1.2
Log(N_H)
22.8
22.6
22.4
0.0
0.5
1.0
PHASE

Figure - 25.

13-15, Sept. 1983

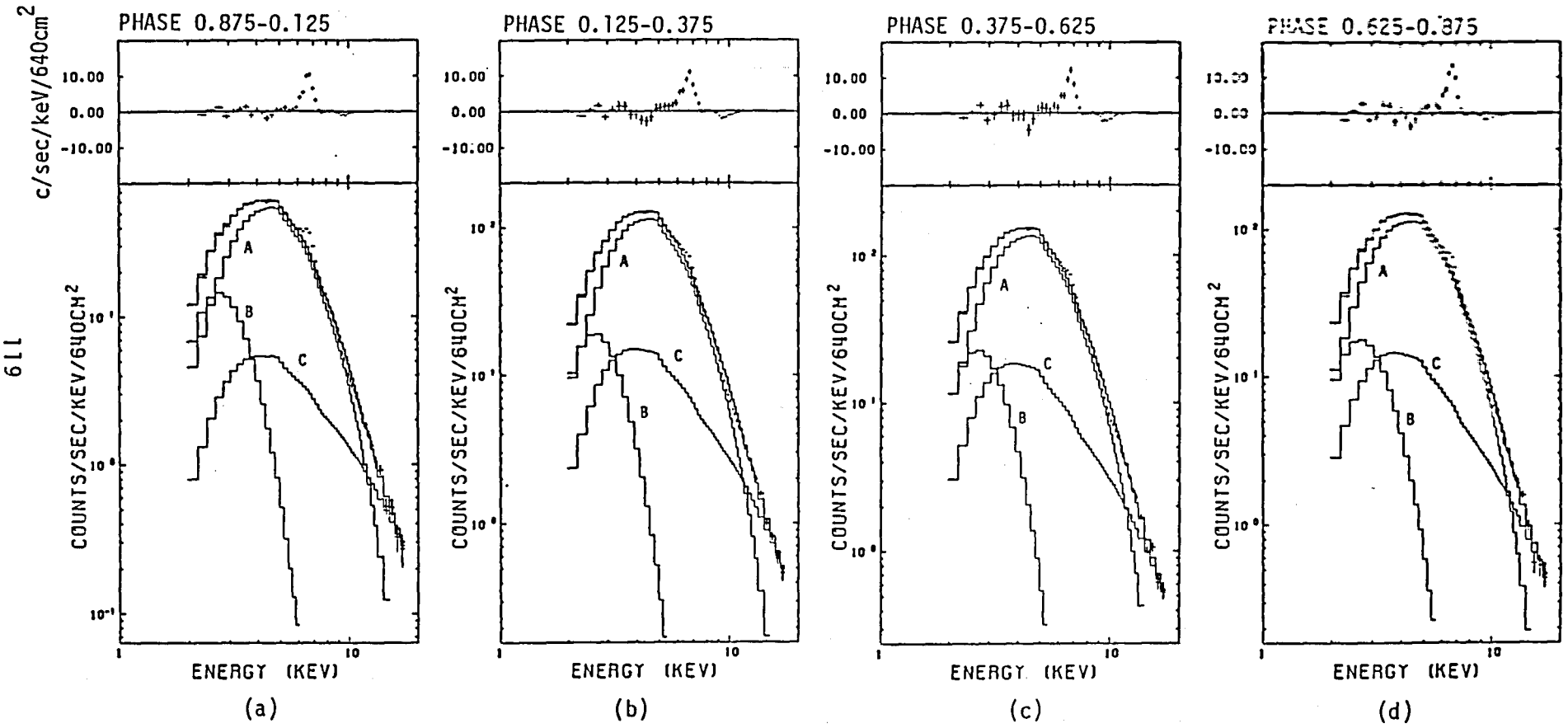

Figure - 26.

16-18, Sept. 1983

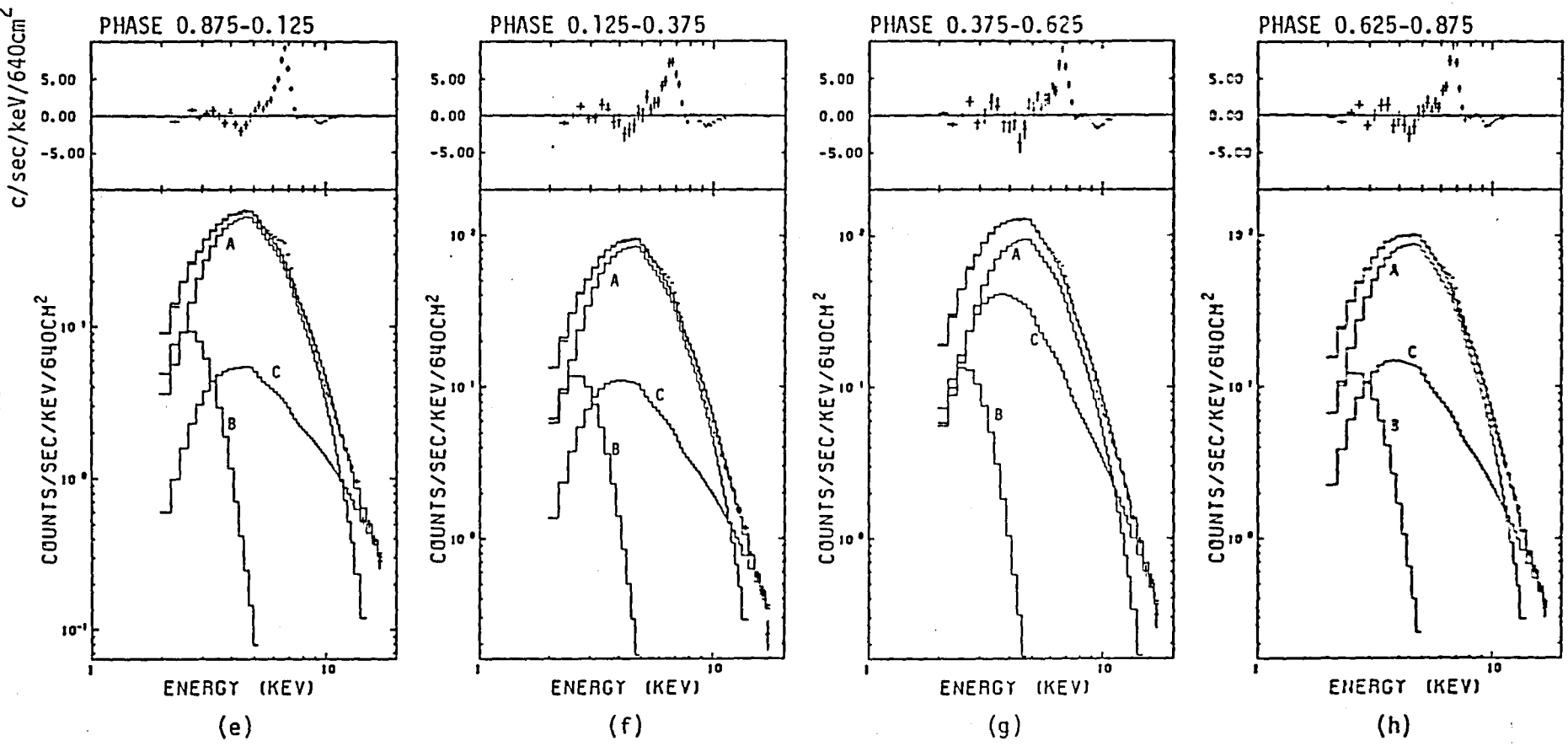

Figure - 26.

11-14, Sept. 1984

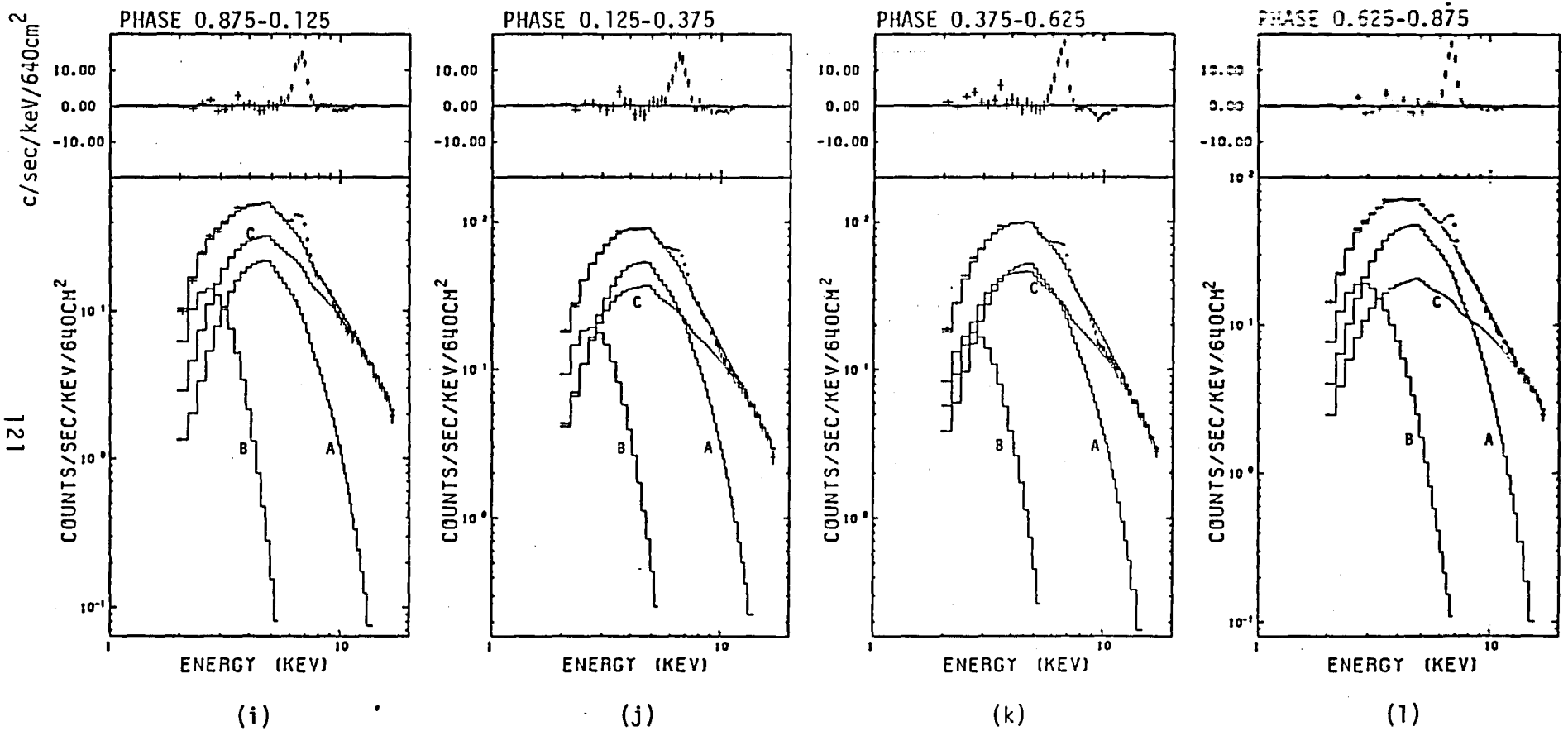

Figure - 26.

13-15, Sept. 1983

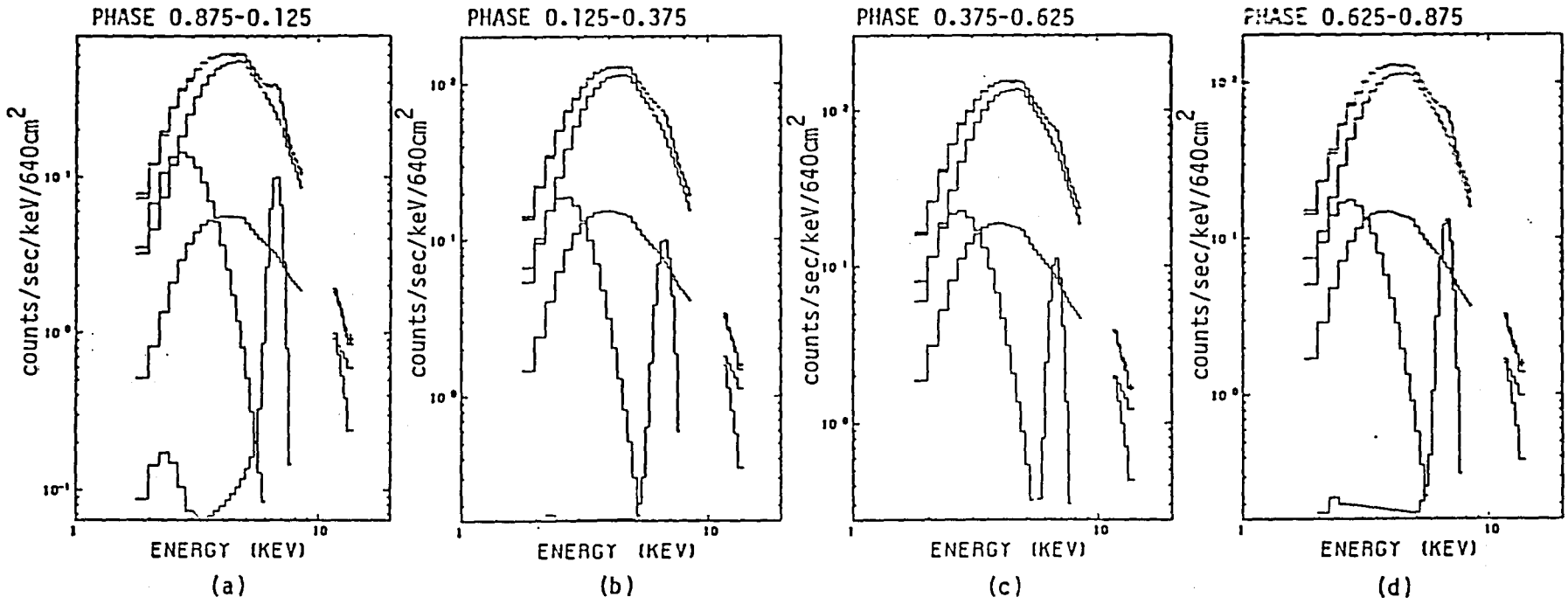

Figure - 27.

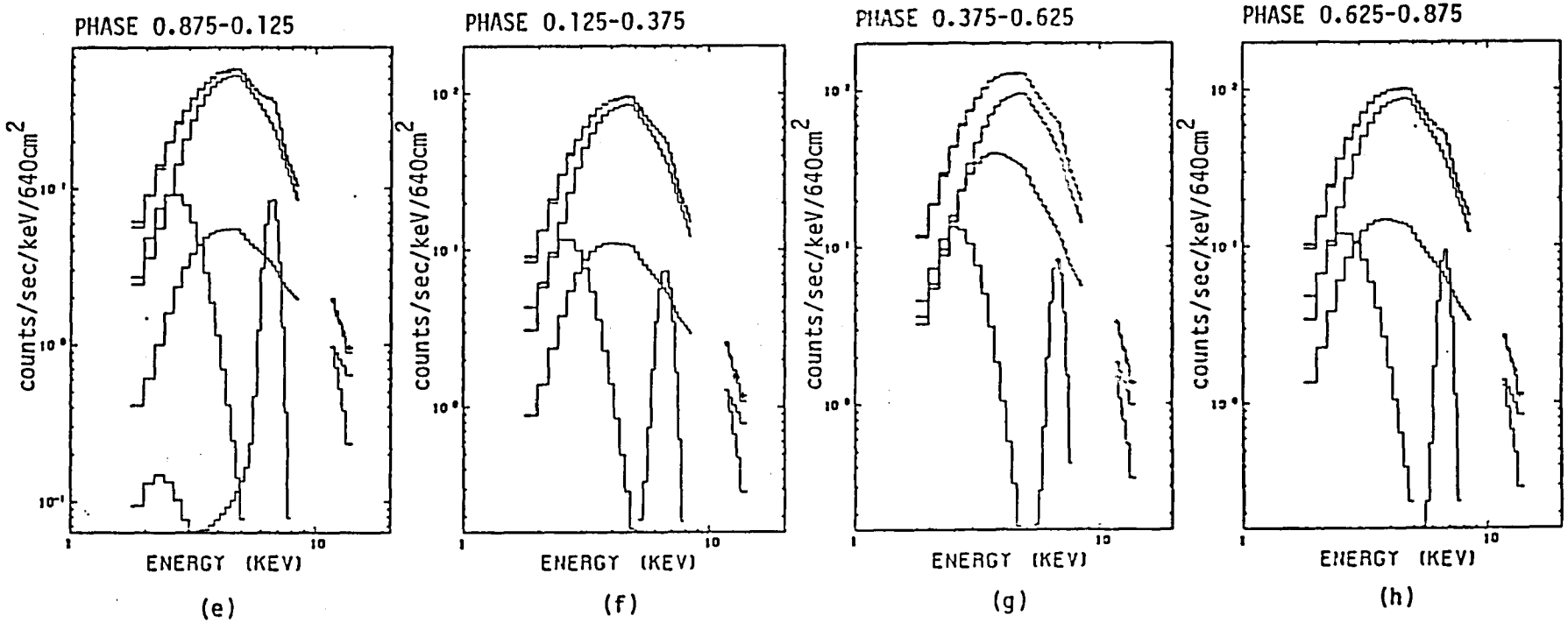
16-18, Sept, 1983
PHASE 0.875-0.125
PHASE 0.125-0.375
PHASE 0.375-0.625
PHASE 0.625-0.875
counts/sec/keV/640cm^2
ENERGY (KEV)
(e)
(f)
(g)
(h)

Figure - 27.

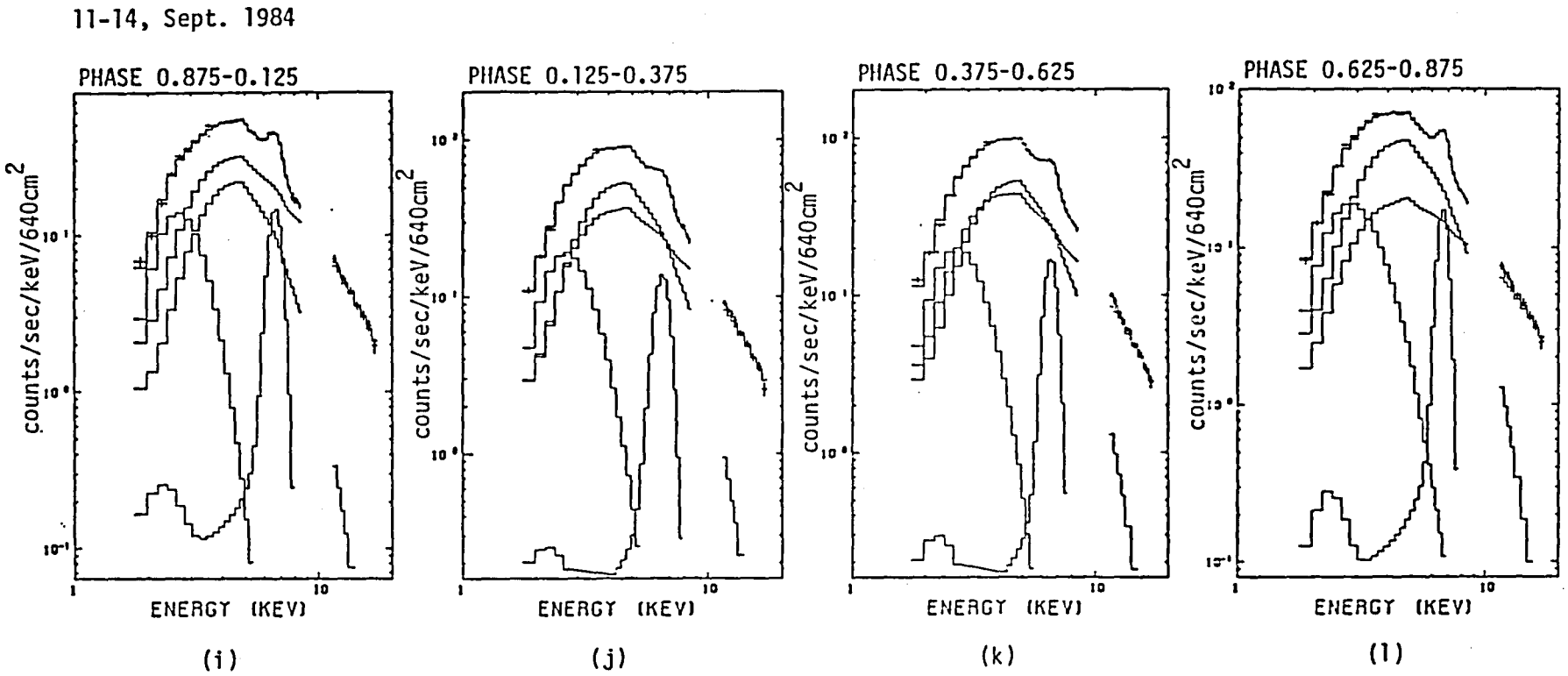
11-14, Sept. 1984
PHASE 0.875-0.125
PHASE 0.125-0.375
PHASE 0.375-0.625
PHASE 0.625-0.875
counts/sec/keV/640cm^2
ENERGY (KEV)
(i)
(j)
(k)
(l)

Figure - 27.

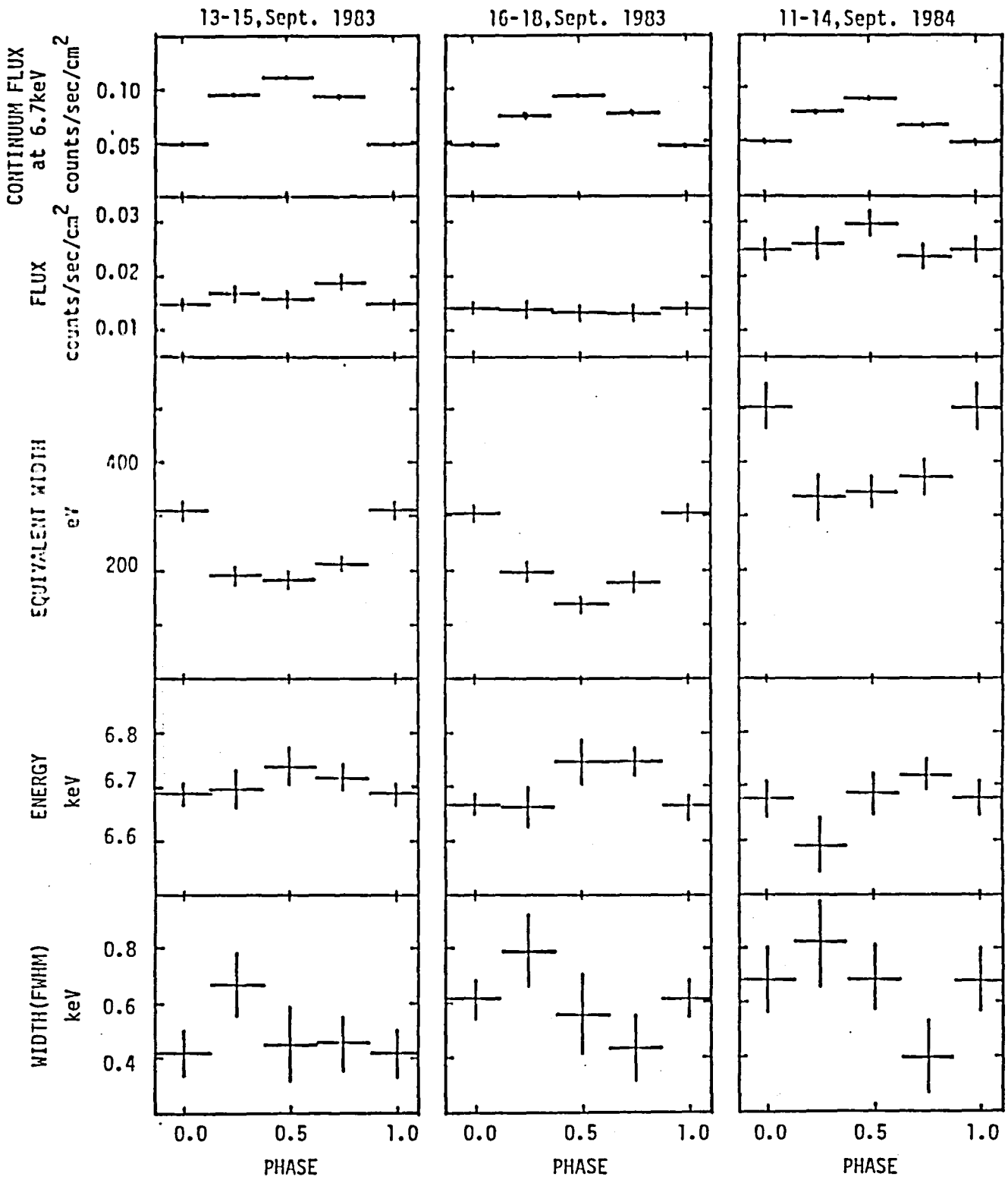
13-15,Sept. 1983
16-18,Sept. 1983
11-14,Sept. 1984
CONTINUUM FLUX at 6.7keV
FLUX counts/sec/cm2 counts/sec/cm2
0.10
0.05
0.03
0.02
0.01
EQUIVALENT WIDTH eV
400
200
ENERGY keV
6.8
6.7
6.6
WIDTH(FWHM) keV
0.8
0.6
0.4
0.0
0.5
1.0
PHASE

Figure - 28.

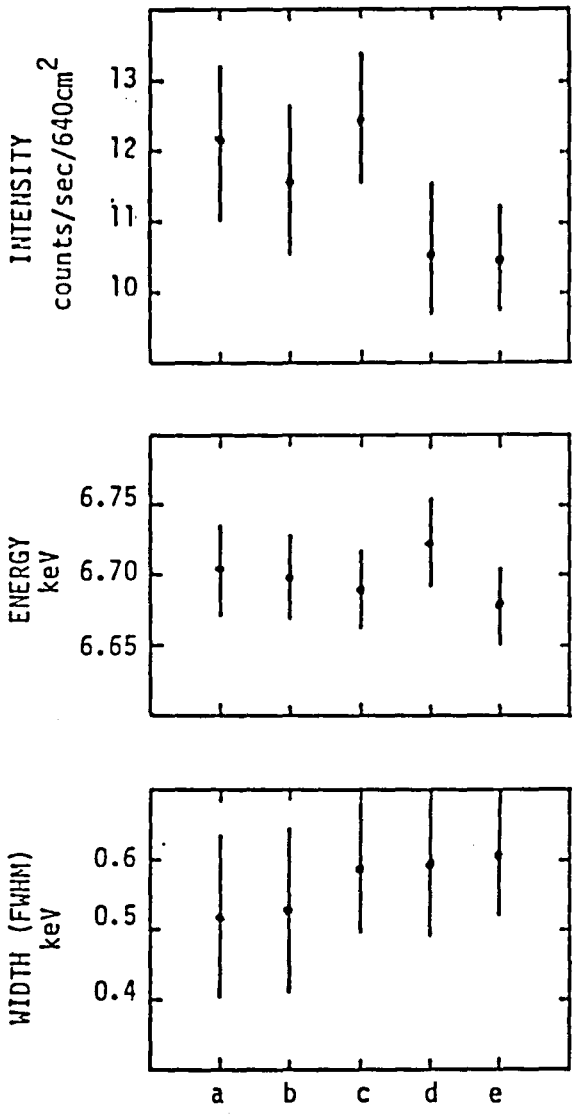
INTENSITY
counts/sec/640cm^2
13
12
11
10
ENERGY
keV
6.75
6.70
6.65
WIDTH (FWHM)
keV
0.6
0.5
0.4
a
b
c
d
e

Figure - 29.

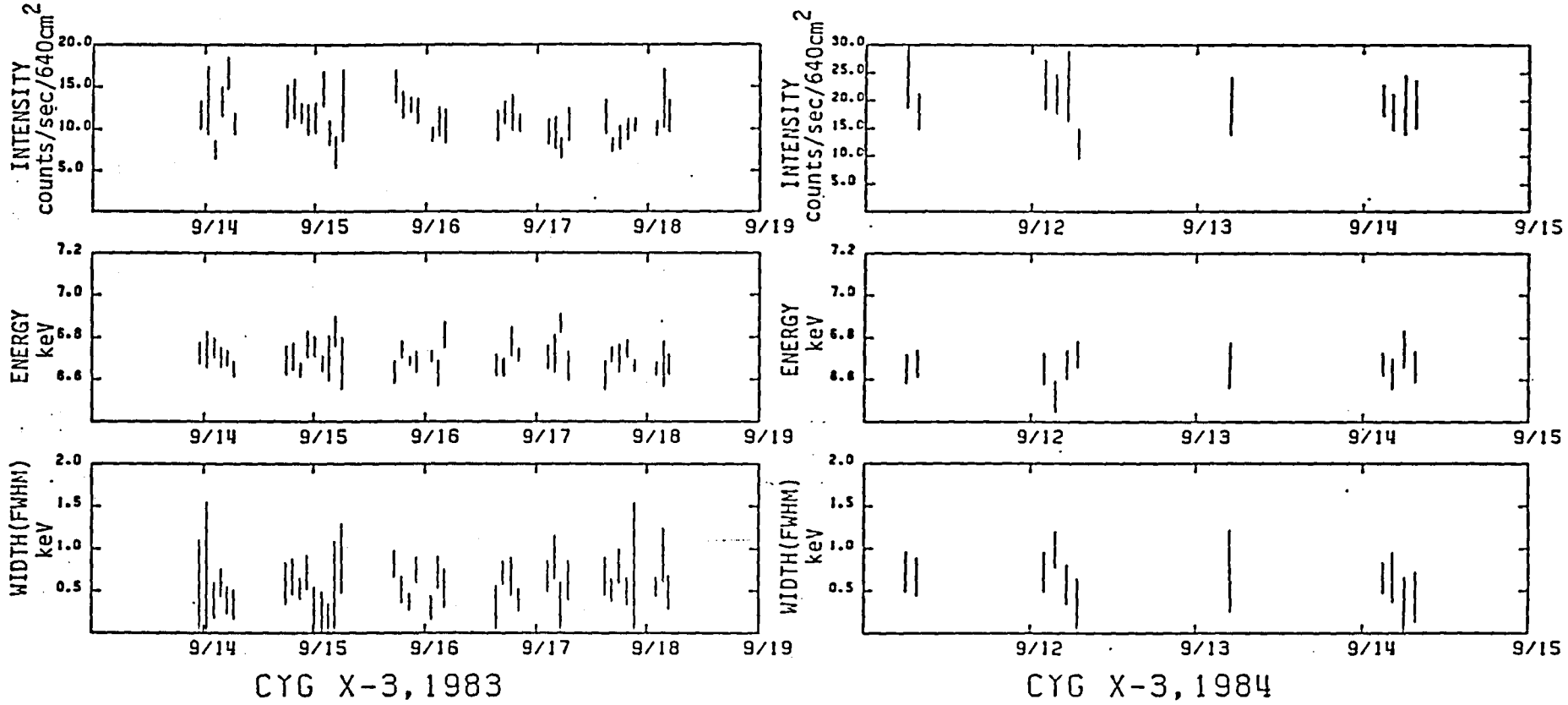
INTENSITY counts/sec/640cm2
ENERGY keV
WIDTH(FWHM) keV
9/14
9/15
9/16
9/17
9/18
9/19
CYG X-3, 1983
9/12
9/13
9/14
9/15
CYG X-3, 1984

(a) (b)

Figure-30.

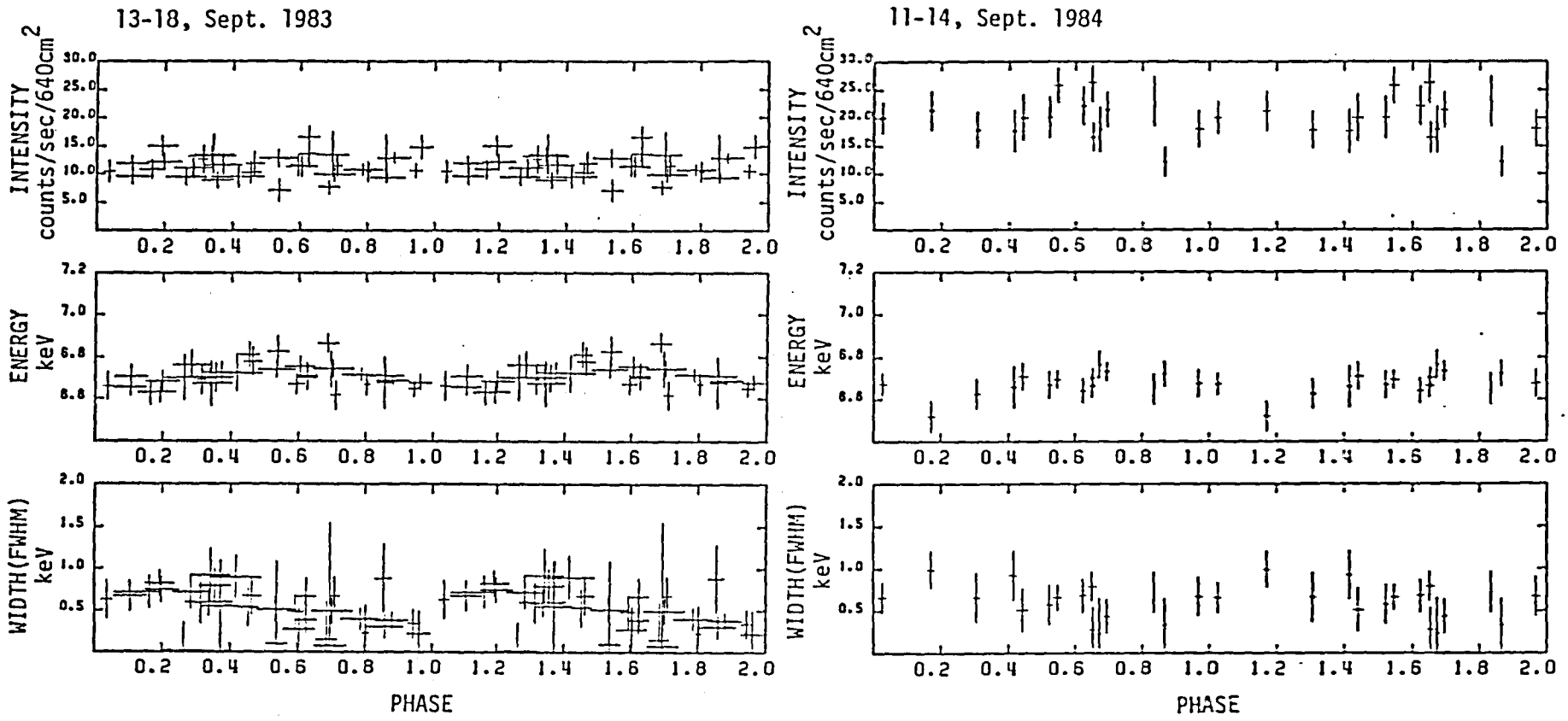
13-18, Sept. 1983
11-14, Sept. 1984
INTENSITY counts/sec/640cm^2
ENERGY keV
WIDTH(FWHM) keV
PHASE
(a)
(b)

Figure - 31.

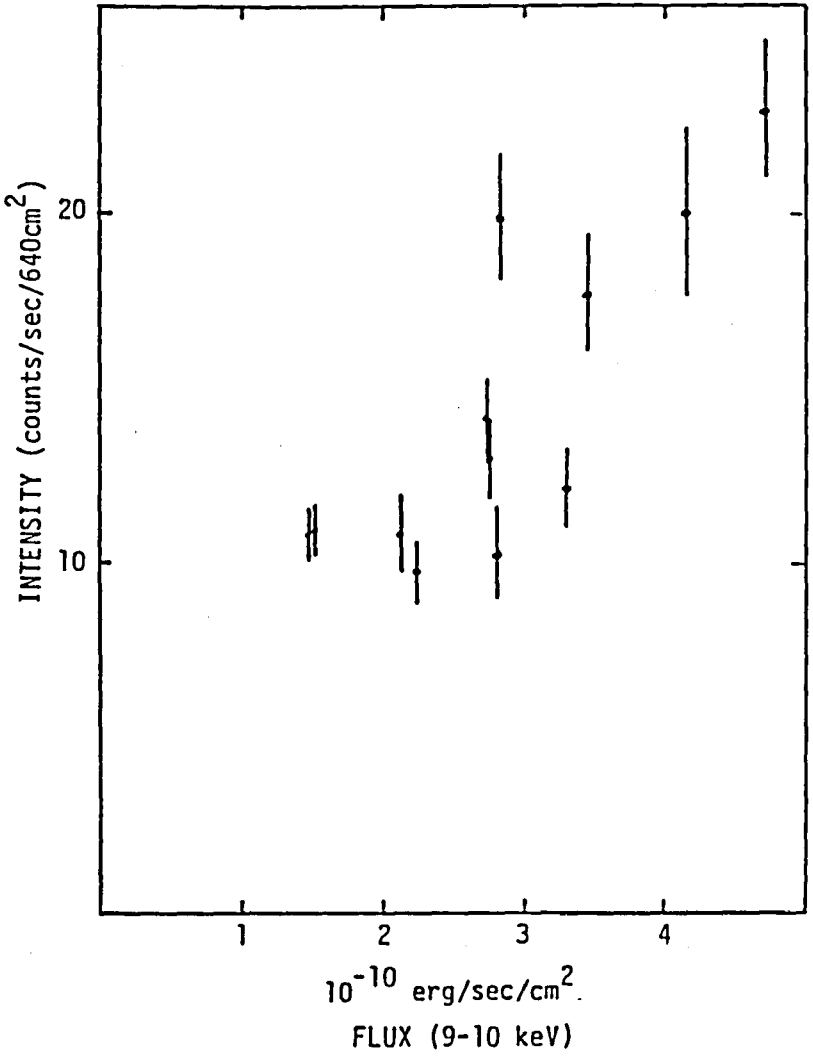

Figure - 32.

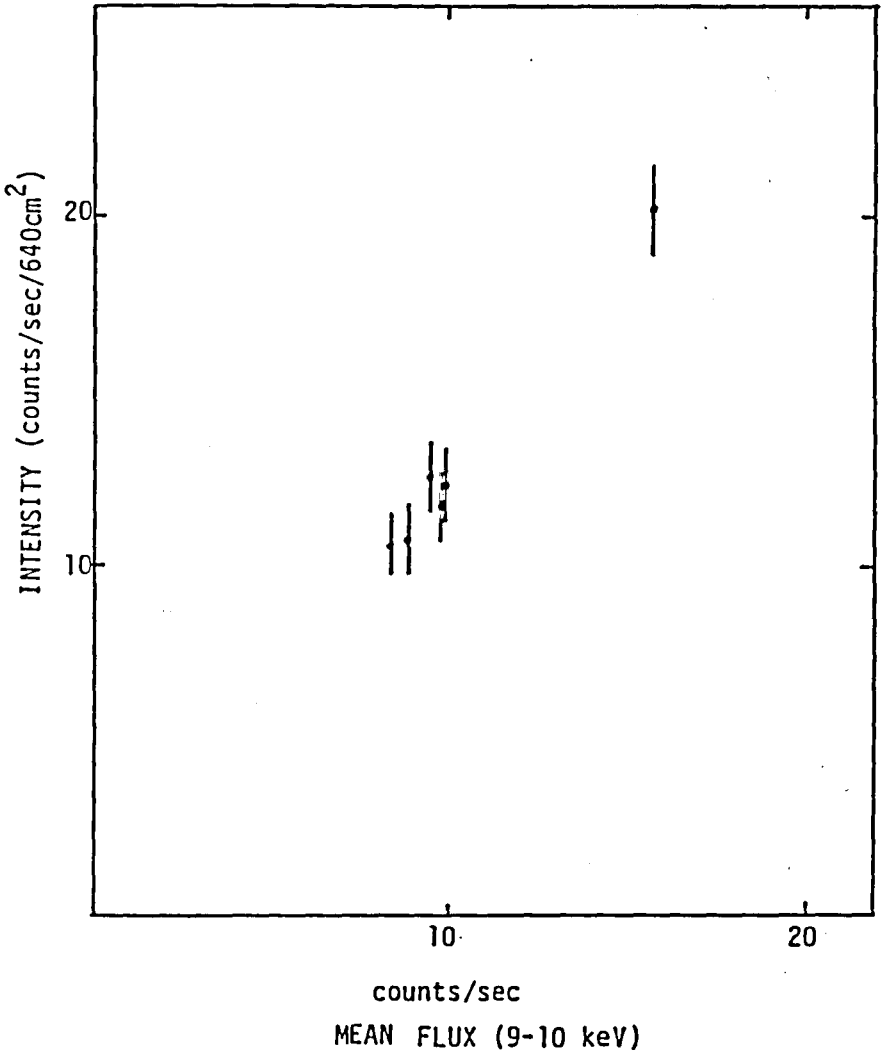

Figure - 33.

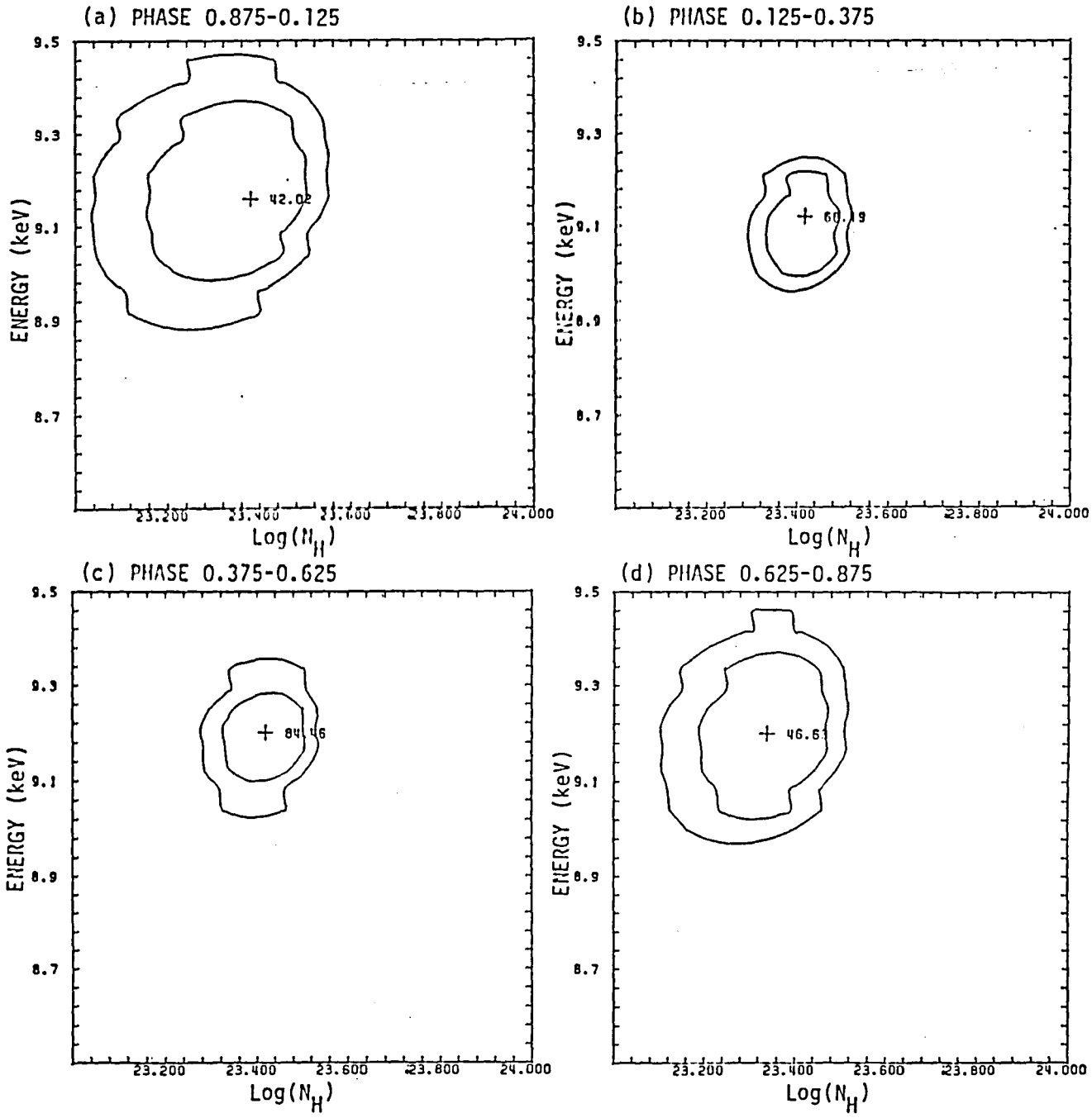
(a) PHASE 0.875-0.125
(b) PHASE 0.125-0.375
(c) PHASE 0.375-0.625
(d) PHASE 0.625-0.875
ENERGY (keV)
Log(N_H)
9.5
9.3
9.1
8.9
8.7
23.200
23.400
23.600
23.800
24.000

Figure - 34.

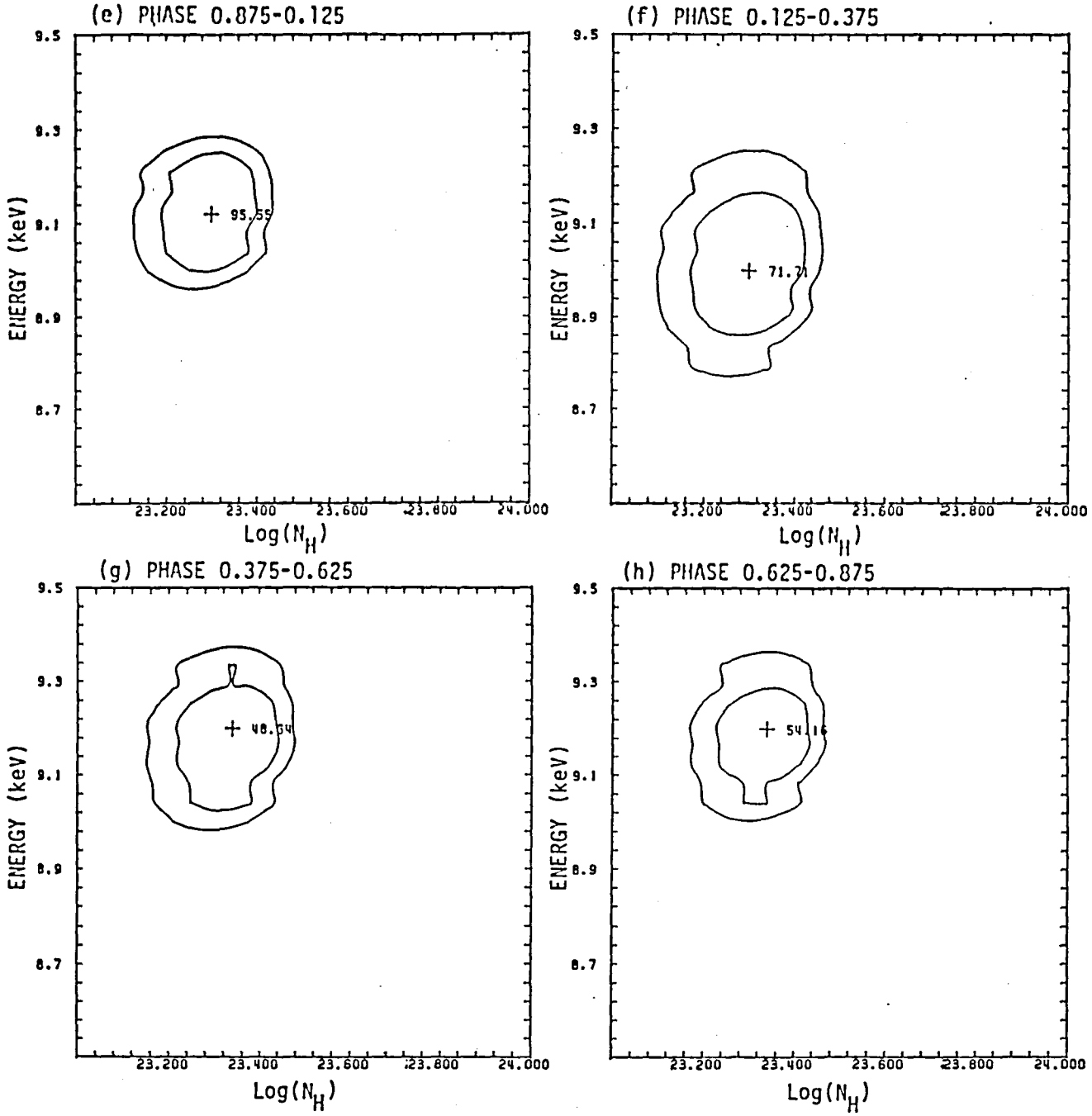
(e) PHASE 0.875-0.125
(f) PHASE 0.125-0.375
(g) PHASE 0.375-0.625
(h) PHASE 0.625-0.875
ENERGY (keV)
Log(N_H)
9.5
9.3
9.1
8.9
8.7
23.200
23.400
23.600
23.800
24.000

Figure - 34.

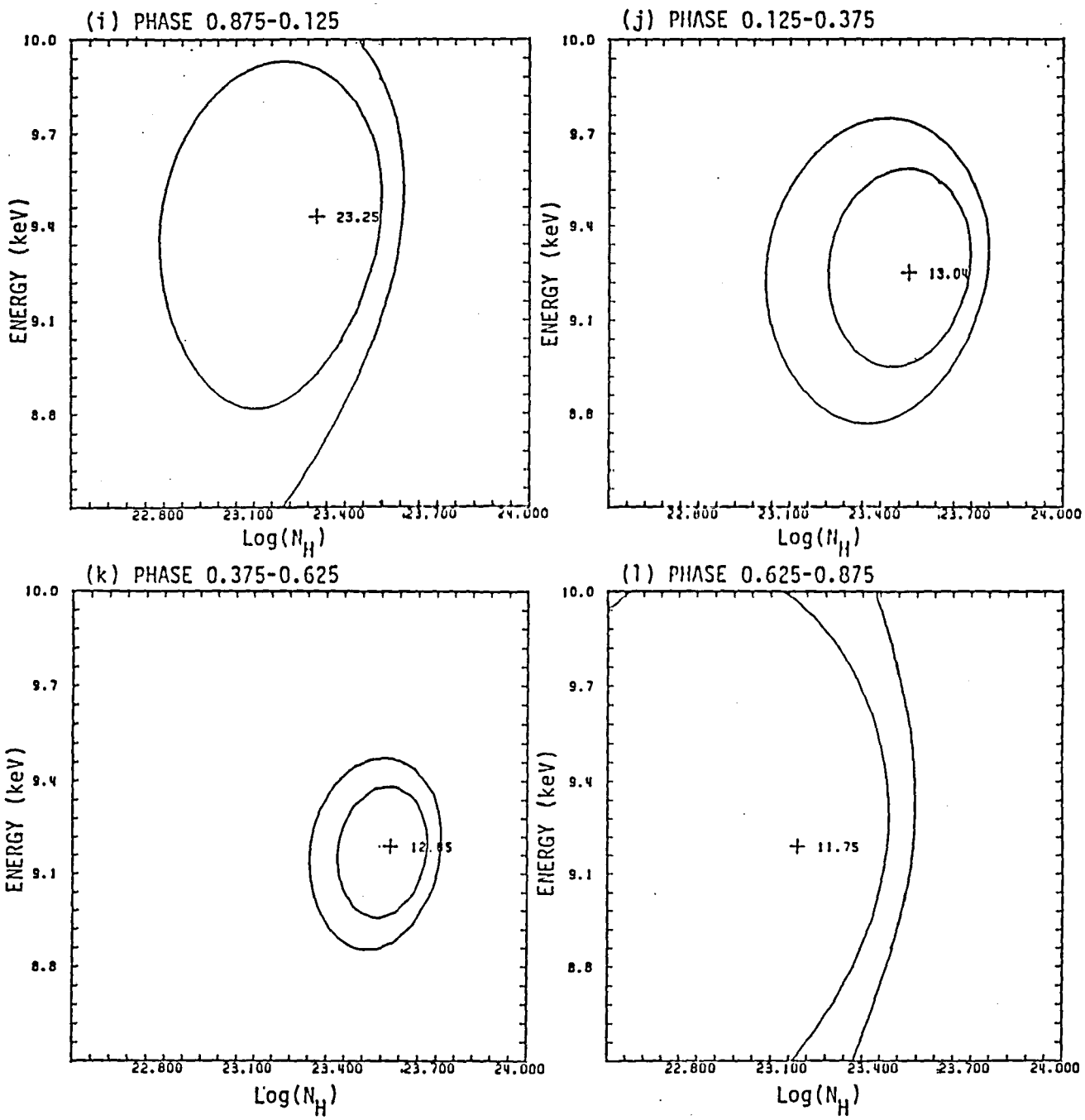
(i) PHASE 0.875-0.125
(j) PHASE 0.125-0.375
(k) PHASE 0.375-0.625
(l) PHASE 0.625-0.875
ENERGY (keV)
Log(N_H)
10.0
9.7
9.4
9.1
8.8
22.800
23.100
23.400
23.700
24.000
23.25
13.04
11.75

Figure - 34.

$I(E) \propto E^{-4.90}$

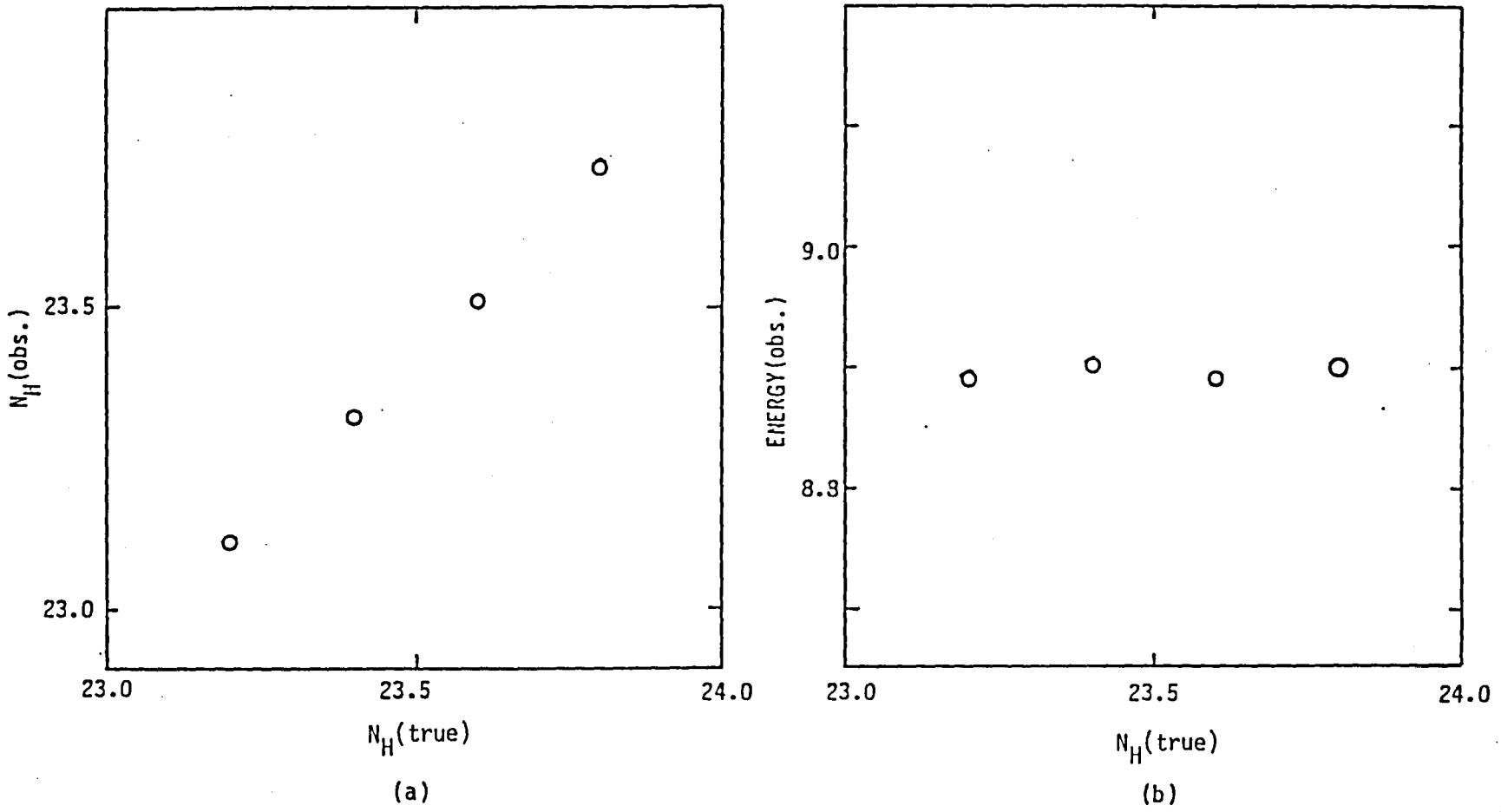

Figure - 35.

$I(E) \propto E^{-2.28}$

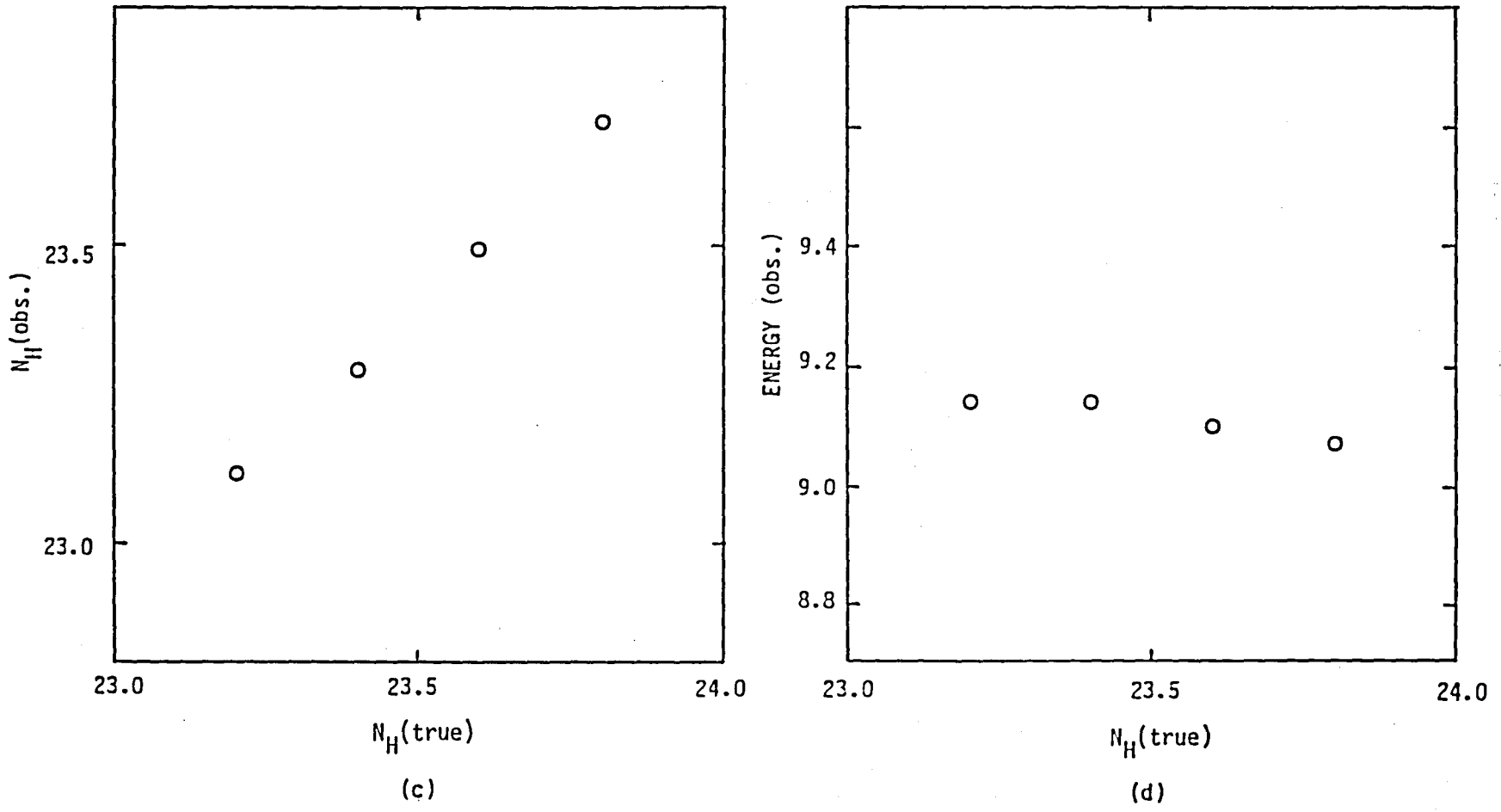

Figure - 35.

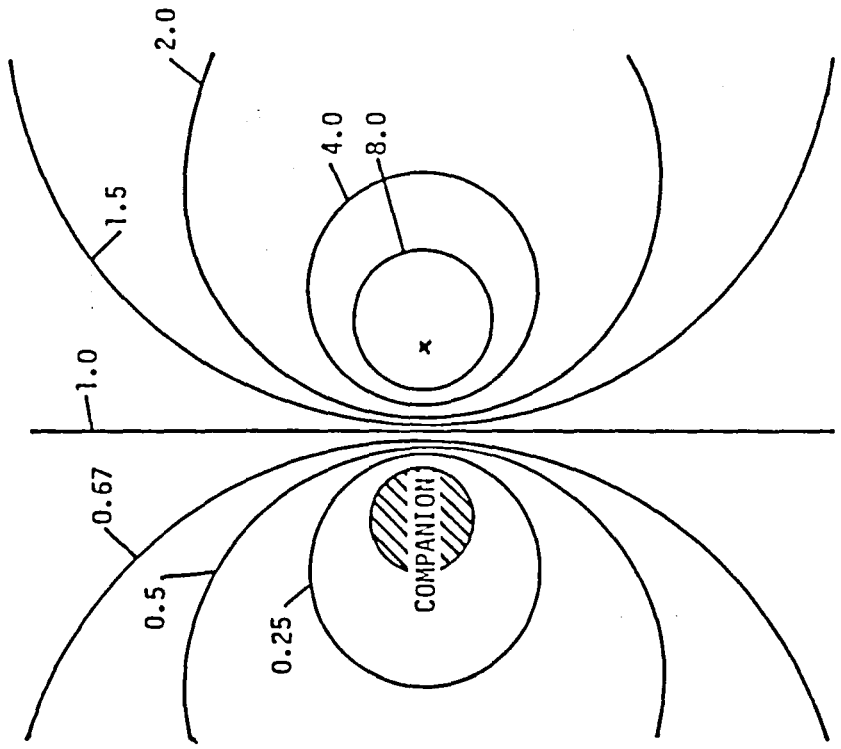

Figure - 36.

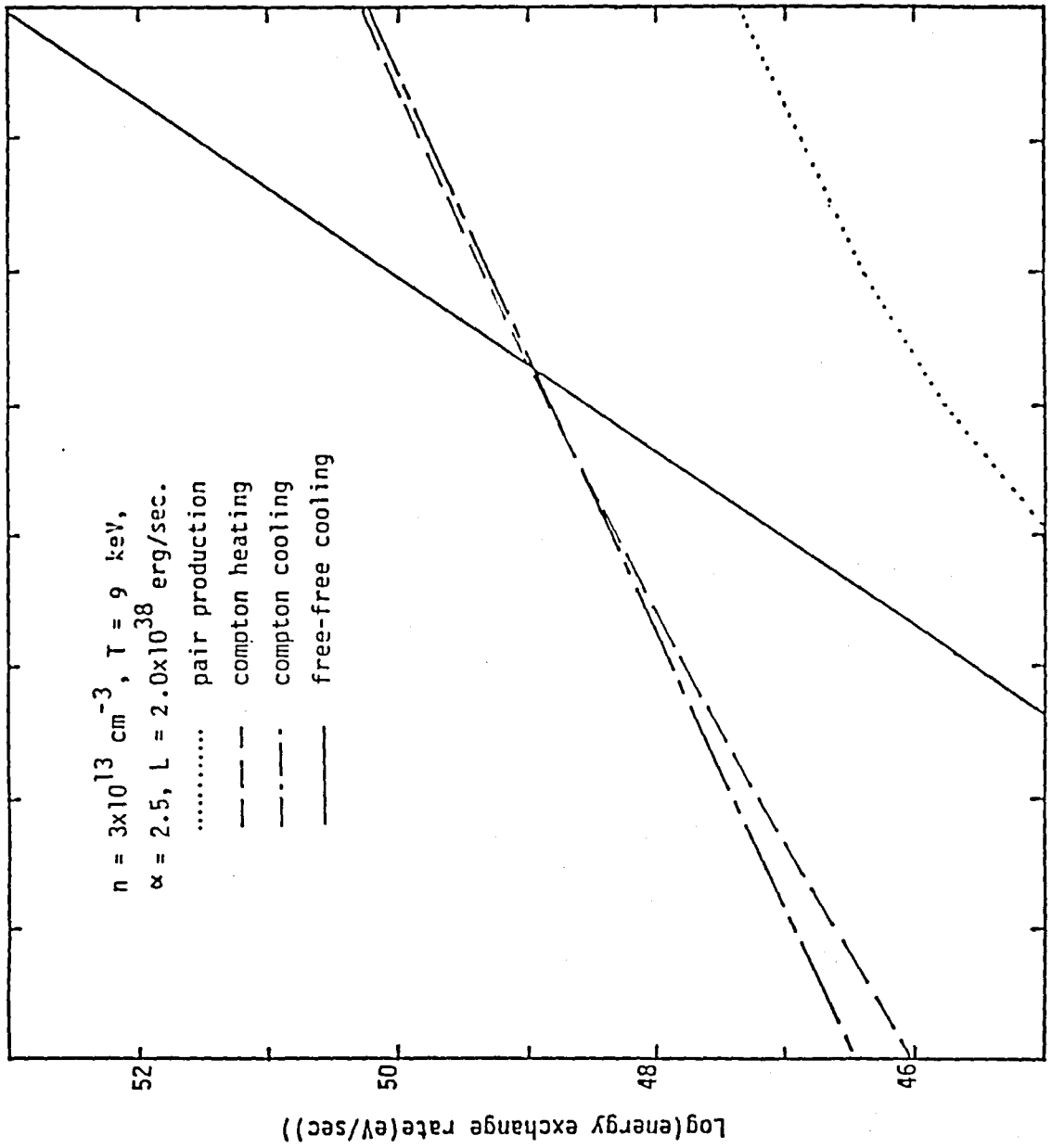
n = 3x10^13 cm^-3, T = 9 keV,
α = 2.5, L = 2.0x10^38 erg/sec.
pair production
compton heating
compton cooling
free-free cooling
Log(energy exchange rate(eV/sec))
Log(r(cm))
(a)

Figure - 37.

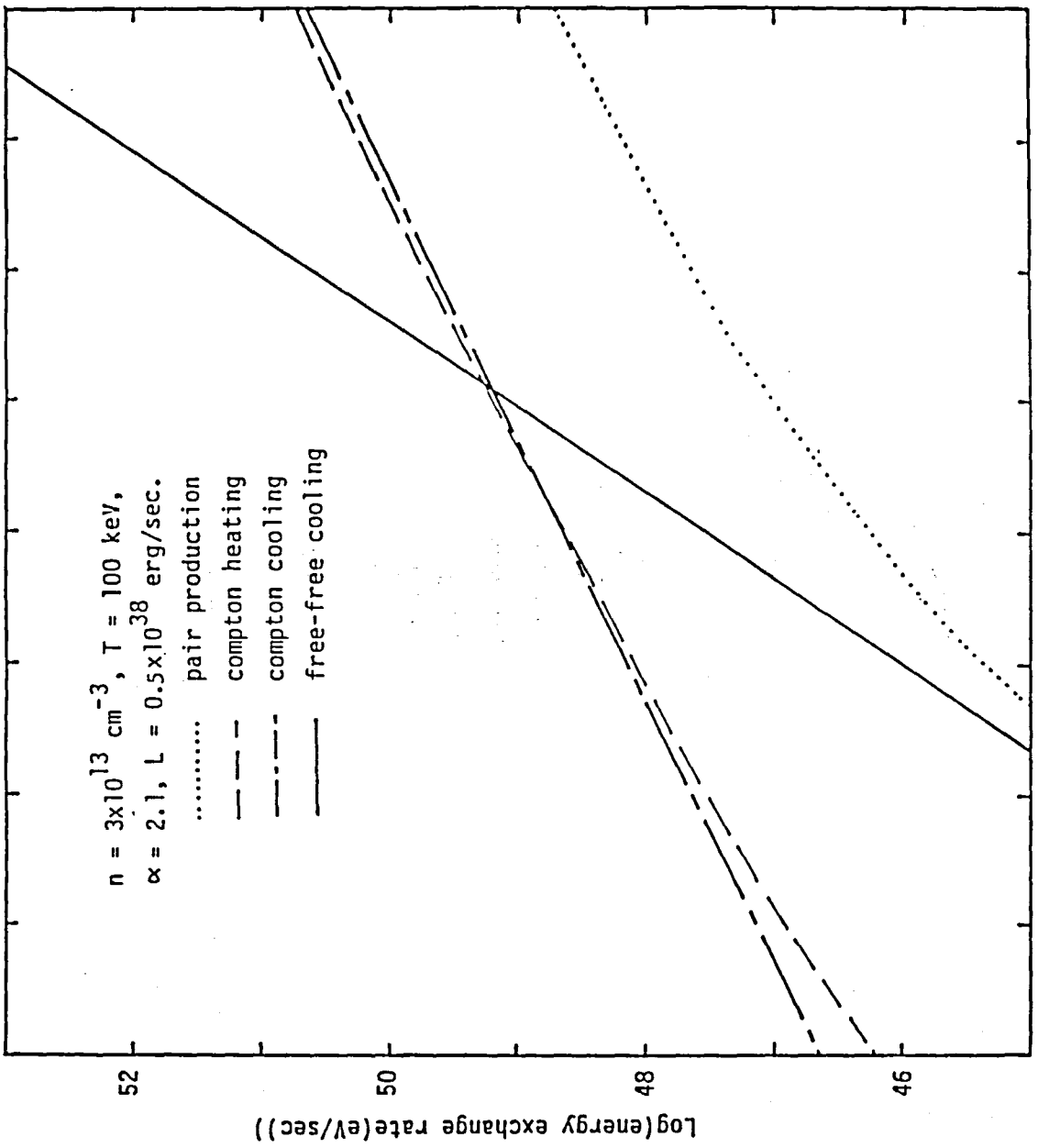
n = 3x10^13 cm^-3, T = 100 keV,
α = 2.1, L = 0.5x10^38 erg/sec.
pair production
compton heating
compton cooling
free-free cooling
Log(energy exchange rate(eV/sec))
52
50
48
46
8
9
10
11
Log(r(cm))

(b)

Figure - 37.

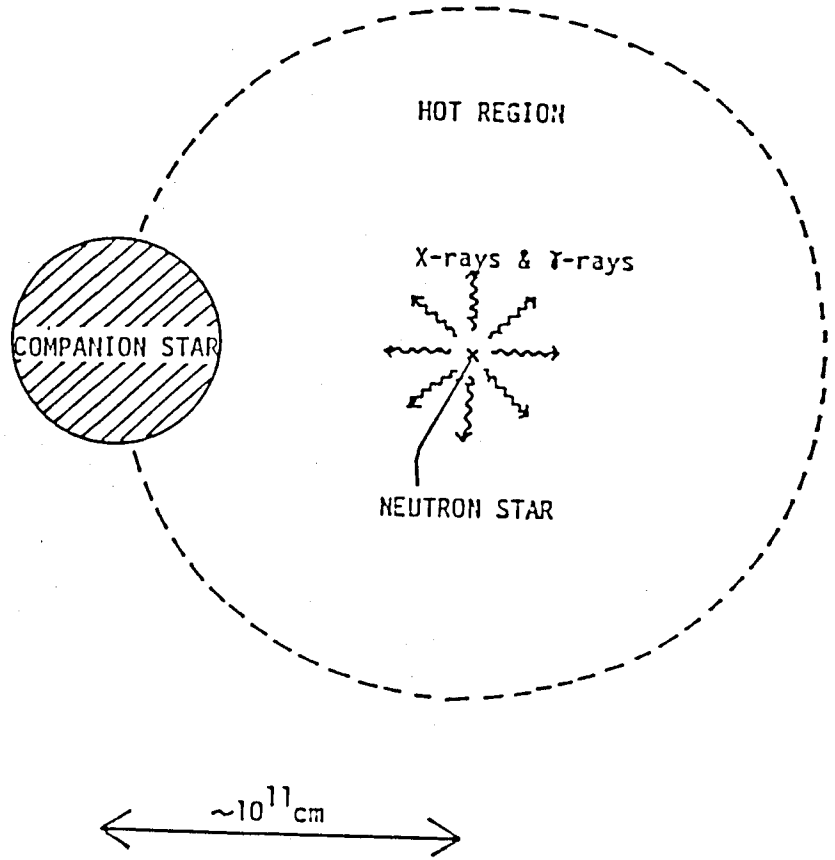

Figure - 38.

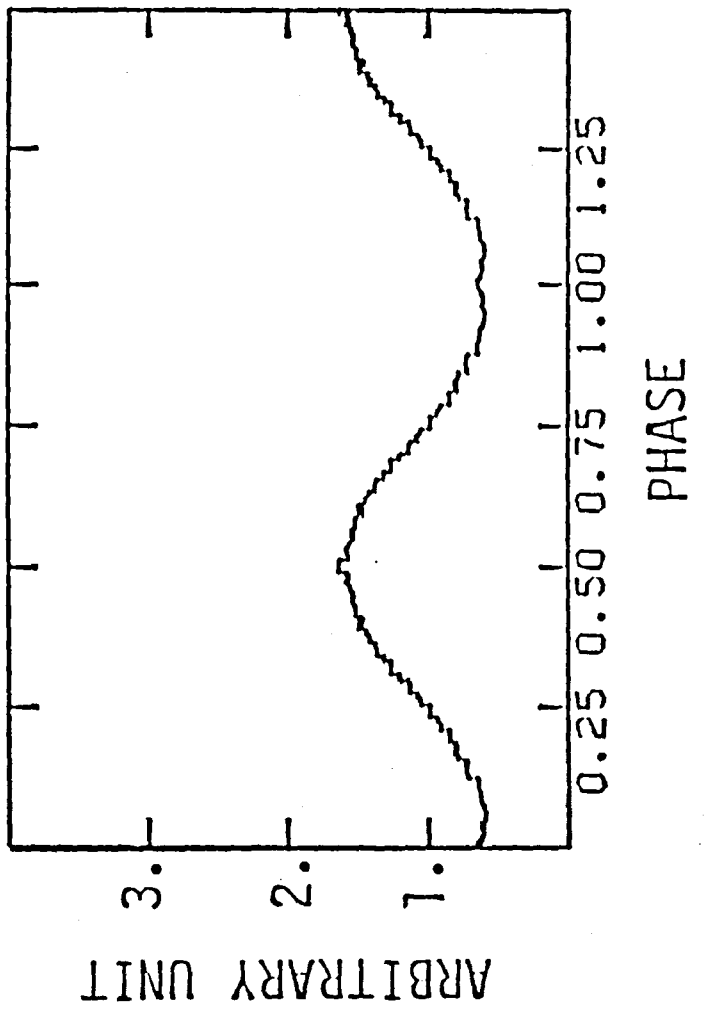

Figure - 39.

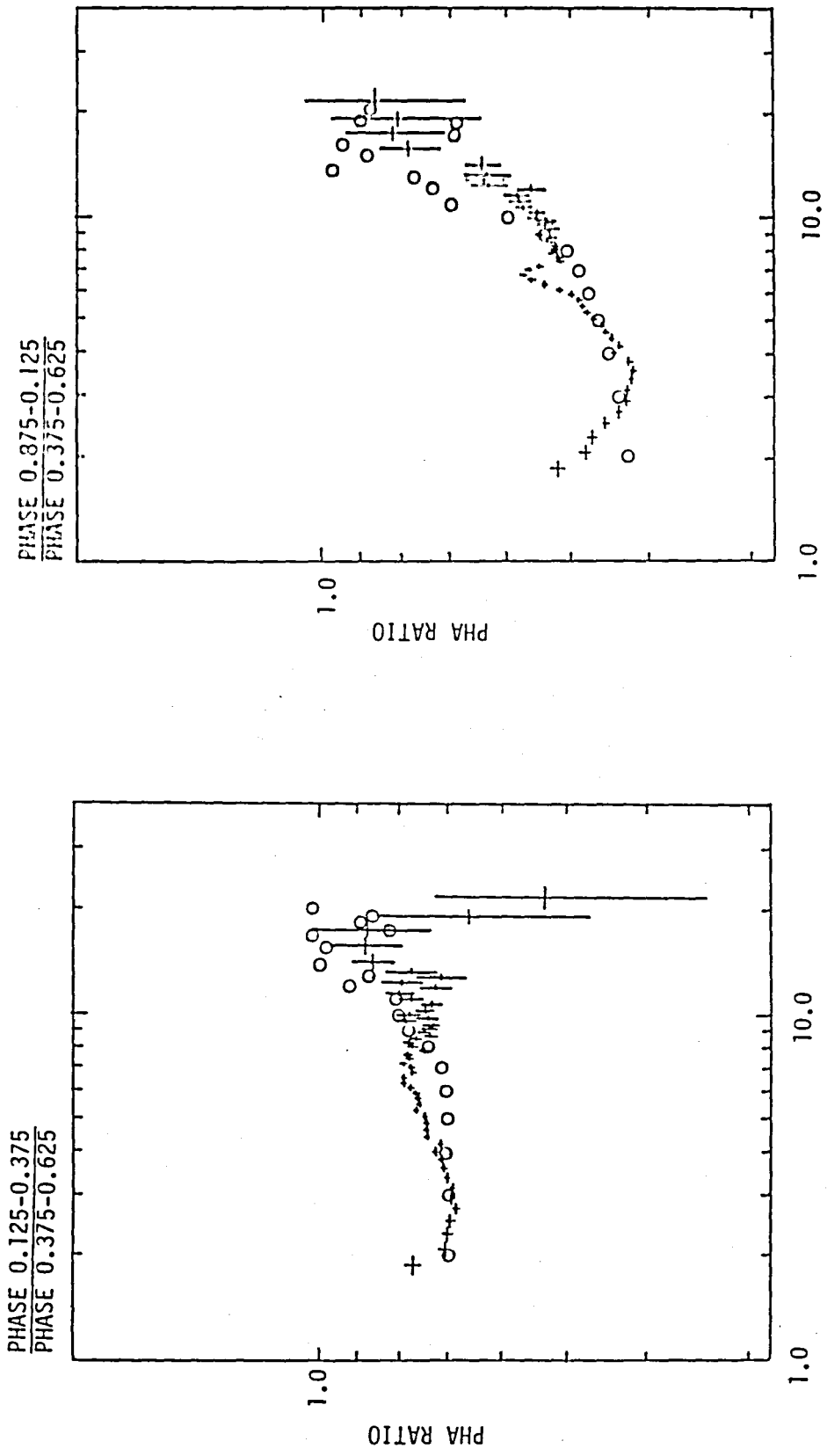
PHASE 0.375-0.125
PHASE 0.375-0.625
PHA RATIO
1.0
1.0
10.0
ENERGY (keV)
(b)
PHASE 0.125-0.375
PHASE 0.375-0.625
PHA RATIO
1.0
1.0
10.0
ENERGY (keV)
(a)

Figure - 40.